IEEE Access
Multidisciplinary | Rapid Review | Open Access Journal

IEEE POWER & ENERGY SOCIETY SECTION

Received 8 July 2022, accepted 30 July 2022, date of publication 8 August 2022, date of current version 16 August 2022.

Digital Object Identifier 10.1109/ACCESS.2022.3197194

RESEARCH ARTICLE

A Deep Learning Based Multiobjective Optimization for the Planning of Resilience Oriented Microgrids in Active Distribution System

YOUTHANALACK VILAISARN[1], YURI R. RODRIGUES[2], MORAD MOHAMED ABDELMAGEED ABDELAZIZ[3], (Senior Member, IEEE), AND JÉRÔME CROS[1]

[1]Department of Electrical and Computer Engineering, Université Laval, Québec, QC G1V 0A6, Canada
[2]Department of Engineering and Computer Science, Seattle Pacific University, Seattle, WA 98119, USA
[3]School of Engineering, University of British Columbia, Kelowna, BC V1V 1V7, Canada

Corresponding author: Morad Mohamed Abdelmageed Abdelaziz (morad.abdelaziz@ubc.ca)

This work was supported in part by the Programme Canadien de Bourses de la Francophonie (PCBF), and in part by the Natural Sciences and Engineering Research Council of Canada (NSERC), Canada.

ABSTRACT When facing severe weather events, a distribution system may suffer from the loss or failure of one or more of its components, the so-called N-K contingencies. Nevertheless, taking advantage of the system's isolate switches and the increasing availability of distributed energy resources (DERs), a distribution system may be clustered into microgrids able to withstand such contingencies with minimal power interruption. In this perspective, this work proposes a novel bilevel optimization framework for planning microgrids in active distribution systems under a resilience-oriented perspective. For this, first, the outer level optimization features a multi-objective problem seeking to optimally allocate DERs and isolate switches in the distribution network while balancing the competing objectives of cost, resilience, and environmental impact. Next, the inner level handles the optimization problem pertaining to the optimal operation of the microgrids that can be created by harnessing local DERs and isolate switches allocated in the outer level. Further, given the proposed approach resilience-oriented focus, the developed framework employes deep learning models based on deep neural network (DNN) architectures trained using Bayesian Regularization Backpropagation (BRB) technique. This strategy allows for avoiding the modeling simplifications typically employed to alleviate the computational burden that can otherwise jeopardize planning solutions' feasibility. Thus, enabling the accurate consideration of microgrids' operational behavior, including hierarchal controls and the stochastic nature of loads, generation, and weather-induced line failures, especially critical aspects under resilience-oriented planning. Simulation case studies are developed to demonstrate the effectiveness of the developed planning framework.

INDEX TERMS Resilience, stochastic linear optimal power flow, microgrids formation, NSGA-II, deep learning.

NOMENCLATURE

A. ABBREVIATION

AC	Alternative Current system
BRB	Bayesian Regularization Backpropagation
CO_2	Carbon dioxide
DDG	Dispatchable Distributed Generation
DER	Distributed Energy Resource
DFS	Depth First Search algorithm
DGs	Distributed Generations
DL-LOPF^{AC}	Deep Learning AC-LOPF
DNN	Deep Neural Network
droop/2nd	Primary droop mode with a supervisory secondary control layer
DSO	Distribution System Operator

The associate editor coordinating the review of this manuscript and approving it for publication was Shafi K. Khadem.

ES	Energy Storage unit
GC	Grid-Connected operation
HILP	High Impact Low Probability
IS	Islanded operation
ISW	Isolate Switch
ISW^{sub}	Isolate Switch at the upstream substation
MG(s)	Microgrid(s)
MILP	Mixed Integer Linear Programming
NaS	Technology Sodium Sulfur
N-K	Level of contingencies
NREL	National Renewable Energy Laboratory
NSGA-II	Non-dominated Sorting Genetic Algorithm II
NYISO	New York Independent System Operator
O&M	Operation and Maintenance
OPF/LOPF	Non-Linear/Linear Optimum Power Flow
PHEVs	Plug-In Hybrid Electric Vehicles
PQ mode	Active and Reactive power control mode
PV	Photovoltaic unit
SPF	System Performance
WT	Wind Turbine unit

B. SET AND NUMBER

n_{br}	Number of the branches in the test system
n_{bus}	Number of buses in the test system
n_{ddg}	Number of DDGs in the planning problem
n_{es}	Number of ESs in the planning problem
n_{feat}	Number of features in a vector of sample
n_{hl}	Number of hidden layers for DNN model
n_{isw}	Number of ISWs in the planning problem
n_{MG}	Number of the microgrids
n_{path}	Number of the paths search
n_{pv}	Number of PVs in the planning problem
n_{pw}	Number of pieces for piecewise linearization
N_s'	Number of normal scenarios
N_s''	Number of severe scenarios
N_s^{pre}	Number of generated scenarios in Ω_s^{pre}
n_{sam}	Number of samples for training DNN model
N_T	Planning horizon time e.g., 24h
n_{wt}	Number of WTs in the planning problem
$\mathbb{R}$	Continuous variable or real number
$\mathbb{Z}$	Integer variable or binary number
Ω_{BUS}	Set of buses in the test system
Ω_{DDG}^{can}	Set of candidate buses for DDGs
Ω_{ES}^{can}	Set of candidate buses for ESs
Ω_{ISW}^{can}	Set of candidate branches for SSWs
Ω_{PV}^{can}	Set of candidate buses for PV units
Ω_{WT}^{can}	Set of candidate buses for WT units
Ω_{LIN}	Set of lines or branches in the test system
Ω_{LIN}^{fail}	Set of failure branches in the test system
Ω_{TG}^{node}	Set of targets node(s)
Ω_s'	Set of generated scenarios for normal situation
Ω_s''	Set of generated scenarios for severe situations considering network SPF progression phase I and II (i.e., $t^e \rightarrow t^r$)
$\Omega_s^{'',orig}$	Original set before reduction of generated scenarios for severe situation considering network SPF progression phase I and II (i.e., $t^e \rightarrow t^r$)
Ω_s^{pre}	Set of generated pre-scenarios for severe situations considering only network SPF progression phase I (i.e., $t^e \rightarrow t^d$)
Ω_{SAM}	Set of DNN training samples
Ω_{se}	Set of seasonal periods i.e. {fall, winter, spring, summer}
Ω_T	Set of time segment in planning horizon e.g. {1, 2,. . . ,24}

C. PARAMETERS AND VECTOR/MATRIX

$\mathbf{A}^{\mathbf{MG}}$	Adjacency matrix for generating $\mathbf{MG}_t^{\mathbf{set}}$
$APL_{t,s,se}$	Annual peak load pattern in percentage at time t for s^{th} scenario of season se
$\mathbf{AV}$	Line or branch availability binary matrix
$\mathbf{AV}_{s,se}^{\mathbf{I-II}}$	Reduction version of $\mathbf{AV}_{s,se}^{\mathbf{I-II,orig}}$
$\mathbf{AV}_{s,se}^{\mathbf{I-II,orig}}$	Matrix constraining the binary element representing the availability of branches for s^{th} scenario of season se, considering full network SPF progression i.e., phase I and II (i.e., $t^e \rightarrow t^r$)
$\mathbf{AV}_{s,se}^{\mathbf{I}}$	Matrix constraining the binary element representing the availability of branches for s^{th} scenario of season se, considering only network SPF progression phase I (i.e., $t^e \rightarrow t^d$)
$B_{ij,t,s,se}$	Element of the time-coupled susceptance matrix denotes the connection of bus i to bus j at time t for s^{th} scenario of season se
$\mathbf{B}_{s,se}$	3D matrix containing the time coupled susceptance matrices for s^{th} scenario of season se
$b_{t,s,se}^m$	Binary input parameter indicates the operation mode of the microgrid at time t for s^{th} scenario of season se
$\boldsymbol{b}_i$	Vector of biases for i^{th} hidden layer of DNN architecture
B_{ij}	Element of the susceptance matrix denote the connection of bus i to bus j
$\boldsymbol{b}_t^{\boldsymbol{m}}$	Vector containing binary elements $b_{i,t,s,se}^m$ indicates the operation mode for each bus at time t
$\boldsymbol{BFa}_t$	Binary vector represents the bus(es) affected/non-affected by fault(s) at time t
br_i^{fail}	Branch location corresponding to failure branch i
$\boldsymbol{bus}^{\boldsymbol{on}}$	Bus online or bus non affected by fault(s)
$\boldsymbol{bus}_t^{ne}$	Vector containing binary elements $bus_{i,t,s,se}^{ne}$ that indicates bus energize/non-energize at time t for s^{th} scenario of season se
cdf^{nor}	Normal Cumulative Distribution Function

$DDG_{n,sp}^{site}$ Location of n^{th} DDG of sample sp
$\boldsymbol{DDG}_{sp}^{site}$ Vector containing the location of the DDGs for sample sp
$\boldsymbol{DDG}_{sp}^{size}$ Vector containing the size of DDGs for sample sp
$\boldsymbol{DDG}_{t}^{down}$ Vector containing binary elements $DDG_{n,t}^{down}$ that indicate the n^{th} DDG deactivation at time t
$DIJK$ (.) Shortest path between two point by Dijkstra algorithm
DoD^{max} Maximum Depth of Discharge allowable for ES
$E_{i}^{ES,size}$ Energy rating of ES at candidate bus i
$\boldsymbol{ES}_{sp}^{site}$ Vector containing the location of the ESs for sample sp
$\boldsymbol{ES}_{t}^{down}$ Vector containing the status of the ESs (i.e., $ESS_{i,t,s,se}^{down}$) at time t
$f^{dnn'}$ Activation function for the output layer
$f_{i}^{dnn}(.)$ Activation function for the i^{th} hidden layer
$\boldsymbol{f}_{t}^{\boldsymbol{bus}}$ Vector containing $f_{n,t}^{bus}$ that indicate the location of the controllable bus at time t for a n^{th} DDG
$\mathbf{FA}^{\mathbf{br}}$ Binary matrix represents branches affected by the different locations of faults
$\mathbf{FA}^{\mathbf{bus}}$ Binary matrix represents buses affected by the different locations of faults
$fb(br_{i}^{fail})$ From bus of the failure overhead line of branch i
$\boldsymbol{fb}, \boldsymbol{tb}$ Set of from bus and to bus for the test case topology
$\boldsymbol{floc}_{t}$ Vector containing the i^{th} fault at location i.e., $floc_{i,t}$ at time t
$\mathbf{G}^{\mathbf{bus}}$ Undirected graph representation by set of vertices (nodes) $\boldsymbol{ND}^{\boldsymbol{bus}}$ and set of edge (branch) $\boldsymbol{ED}^{\boldsymbol{br}}$
$G_{ij,t,s,se}$ Element of the time-coupled conductance matrix denotes the connection of bus i to bus j at time t for s^{th} scenario of season se
$\boldsymbol{G}_{s,se}$ 3D matrix containing the time coupled conductance matrices for s^{th} scenario of season se
G_{ij} Element of the conductance matrix denotes the connection of bus i to bus j
$\boldsymbol{h}^{\boldsymbol{ddg}}$ Vector containing h_{m}^{ddg} that indicate the presents of DDG for m^{th} MG
$h_{1}^{high}/h_{2}^{high}$ Pre-determined range for determining φ^{br} for the case corresponding to higher wind $v_{t,s,se}^{gust} > v_{cri}^{high}$
h_{1}^{low}/h_{2}^{low} Pre-determined range for determining φ^{br} for the case corresponding to $v_{cri}^{low} \leq v_{t,s,se}^{gust} \leq v_{cri}^{high}$
$\bar{I}_{k}^{br}$ Maximum ampacity of the branch k
$\mathbf{IN}^{\boldsymbol{dnn}}$ Matrix containing vector $\boldsymbol{IN}_{sp}^{\boldsymbol{dnn}}$ for training DNN model, $sp \in \Omega_{SAM}$
$\boldsymbol{ISW}^{open}$ Vector containing the location of m^{th} ISW (i.e., ISW_{m}^{open}) in the open state
$\boldsymbol{ISW}^{site}$ Vector containing the location of ISWs
k^{gust} Constant factor for calculating wind-gust
$k^{i\omega}$ Integral gain for frequency restoration for DDG with droop/2nd
$K_{s,se}/K_{s,se}^{HI}$ Level of contingencies
K_{CO2}^{DDG} Carbon emission factor in kg/kWh according to energy generated by DDGs
K_{CO2}^{GRID} Carbon emission factor kg/kWh according to energy imported from the main grid
$L_{i,t,s,se}^{DDG}$ Set of piecewise linearization for DDG quadratic constraint
$L_{i,t,s,se}^{ES}$ Set of piecewise linearization for ES quadratic constraint
$L_{i,t,s,se}^{PCC}$ Set of piecewise linearization for PCC quadratic constraint
$L_{k,t,s,se}^{br}$ Set of piecewise linearization for line ampacity quadratic constraint
$\boldsymbol{LFa}_{t}$ Binary vector represents the line(s) affected/non-affected by fault(s) at time t
$\mathbf{M}^{\mathbf{adj}}$ Adjacency matrix
m_{i}^{p} Active droop gain of the i^{th} DDG unit with primary droop/2nd
M_{ij}^{adj} Binary element of $\mathbf{M}^{\mathbf{adj}}$ represents the connection between two adjacent node ij
$\boldsymbol{MG}_{m}^{\boldsymbol{DFS}}$ Vector of m^{th} microgrid obtained by DFS of $m^{th} root^{MG}$
$\boldsymbol{MG}^{\boldsymbol{set}}\mathbf{0}$ Initial set of microgrid formation
$\boldsymbol{MG}_{m,t}^{\boldsymbol{set}}$ Set of buses in m^{th} MG formed at time t
$\mathbf{MG}_{t}^{\mathbf{set}}$ Matrix containing the set of possible microgrids formation due to fault at time t
MSE Mean sum of squares of the DNN errors
MSW Mean sum of squares of the DNN weights
$MTTR^{nw}$ Specified mean time to repair under normal weather conditions
N_{i}^{pole} Number of the poles according to span length of branch i
n_{i}^{q} Reactive droop gain of the i^{th} DDG unit with primary droop/2nd
net^{n} (.) Trained DNN model for target n
$\overline{P}^{DDG}$ Planning upper bound for DDGs allocation
$\overline{P}^{ES}$ Planning upper bound for ESs allocation
$\overline{P}^{PV}$ Planning upper bound for PVs allocation
$\overline{P}^{WT}$ Planning upper bound for WTs allocation
$\boldsymbol{p}_{i,sp}^{\boldsymbol{dnn}}$ Vector of neuron pre-activation obtained by i^{th} hidden layer according to sample sp
$P_{i,t,s,se}$ Active power injected to bus i at time t for s^{th} scenario of season se
$P_{i,t,s,se}^{L}$ Active power load for bus i at time t for s^{th} scenario of season se
$P_{i,t,s,se}^{PV}$ Active power generated by i^{th} PV unit at time t for s^{th} scenario of season s

$P^{WT}_{i,t,s,se}$ Active power generated by i^{th} WT unit at time t for s^{th} scenario of season s

$P^{GRID+}_{t,s,se}$ Active power imported from the main grid at time t for s^{th} scenario of season se. Its corresponding to $P^{PCC}_{i=1,t,s,se} > 0$

$P^{DDG,size}_{i}$ Active power rating of DDG at candidate bus i

$P^{ES,size}_{i}$ Active power rating of ES at candidate bus i

$P^{L,peak}_{i,t,s,se}$ Original active peak load from data sheet, bus i at time t for s^{th} scenario of season se

$P^{PV,size}_{i}$ Active power rating of PV at candidate bus i

$P^{WT,size}_{i}$ Active power rating of WT at candidate bus i

$\overline{P}^{bus}_{i}$ Maximum installation power allowable for DERs at candidate bus i

P^{DDG}_{step} Step size for DDG allocation

P^{ES}_{step} Step size for ES allocation

P^{PV}_{step} Step size for PV allocation

P^{WT}_{step} Step size for WT allocation

$\mathbf{PATH}^{\mathbf{br}}$ Matrix containing the vector $\boldsymbol{path}^{\boldsymbol{br}}_{i}$ with $\forall i \in \Omega^{node}_{TG}$

$\mathbf{PAH}^{\mathbf{bus}}$ Matrix containing the vector $\boldsymbol{path}^{\boldsymbol{bus}}_{i}$ with $\forall i \in \Omega^{node}_{TG}$

$\boldsymbol{path}^{\boldsymbol{br}}_{i}$ Vectors containing the branches in i^{th} road

$\boldsymbol{path}^{\boldsymbol{bus}}_{i}$ Vectors containing the buses in i^{th} road

PC^{VI} Penalty coefficient of voltage violation in \$/kV

$PF^{DDG,4th}_{i}$, $PF^{DDG,1st}_{i}$ Minimum operating power factor allowable of the $1^{st}/4^{th}$ quadrant of the DDG unit i

$PF^{TR,4th}_{i}$, $PF^{TR,1st}_{i}$ Minimum operating power factor allowable of the $1^{st}/4^{th}$ quadrant of the transformer i

$\boldsymbol{PV}^{site}_{sp}$ Vector containing the location of the PVs for sample sp

$\boldsymbol{PV}^{down}_{t}$ Vector containing the status of the PVs (i.e., $PV^{down}_{i,t,se}$) at time t

$Q_{i,t,s,se}$ Reactive power injected to bus i at time t for s^{th} scenario of season se

$Q^{L}_{i,t,s,se}$ Reactive power load for bus i at time t for s^{th} scenario of season se

$Q^{L,peak}_{i,t,s,se}$ Original reactive peak load from data sheet, bus i at time t for s^{th} scenario of season se

R^{C}_{i} Certain solar radiation point of the i^{th} PV unit, typically set to 0.15 kW/m^2

R^{STD}_{i} Solar radiation in standard test conditions of the i^{th} PV un, typically specified as 1000 W/m^2

$\boldsymbol{r}^{dnn}_{ele,sp}$ Vector containing uniform random number between [0,1] for planning element ele for sample sp

$r_{i,t,s}$ Uniform random number for generating $a^{br}_{i,t,s,se}$

$\boldsymbol{r}^{\boldsymbol{m}}_{s,se}$ Vector constraining $r^{m}_{t,s,se}$ for s^{th} scenario of season se

$r^{m}_{i,t,s,se}$ Measured solar radiation of the i^{th} PV unit at time t for s^{th} scenario of season se (kW/m^2)

r^{ES}_{i} Ratio between the rated capacity and rated power for the ES

$\boldsymbol{root}^{\boldsymbol{MG}}$ Vector containing root of each microgrids

$round$ Round deployment, "1" for input $\geq$ 0.5 and "0" otherwise

S_{base} Setting power base value

$\overline{S}^{DDG}_{i}$ Capacity rating of the DDG unit i

$\overline{S}^{ES}_{i}$ Maximum rating power of the ES unit i

$\overline{S}^{TR}_{i}$ Capacity rate of the transformer

SOC^{0}_{i} Initial state of charge of the ES unit

SPF_0/SPF Expected/actual system performance

st^{isw}_{n} Status of ISW n

$t^{r'}$ Time t corresponding to first failure branch revered

t^{d} Time t corresponding to the end of event

t^{e} Time t corresponding to the beginning of impact or severe event

T^{event} Time segment period of the event Phase I

t^{r} Time t corresponding to the full system recovery

T^{repair} Time segment period of the event Phase II

$t^{br,fail}_{i,s,se}$ Time corresponding to the moment when branch i fail for s^{th} scenario of season se

$t^{br,rep}_{i,s,se}$ Time t when branch recovered or repared for s^{th} scenario of season se

$t^{d}_{s,se}$ Time t^{d} for s^{th} scenario of season se

$t^{e}_{s,se}$ Time t^{e} for s^{th} scenario of season se

$t^{r}_{s,se}$ Time t^{r} for s^{th} scenario of season se

$\boldsymbol{TG}^{node}$ Vector containing the set of target node TG^{node}_{i} with $\forall i \in \Omega^{node}_{TG}$

TL Project lifetime, typical set by 10 years

TTR Time to repair

$TTR^{br,fail}_{i,s,se}$ Time to repair of the failure branch i for s^{th} scenario of season se

$\boldsymbol{TTR}^{\boldsymbol{br,fail}}_{s,se}$ Vector TTR containing $TTR^{br,fail}_{i,s,se}$

$\overline{V}$, $\underline{V}$	Maximum/Minimum voltage violation of the bus
v_i^{ci}, v_i^{co}, v_i^{ra}	Cut-in, cut-out, and the rated speed of the i^{th} wind DG, respectively
$\boldsymbol{v}_{s,se}^{\boldsymbol{m}}$	Vector constraining $v_{t,s,se}^{m}$ for s^{th} scenario of season se
$v_{i,t,s,se}^{m}$	Measured wind speed of the i^{th} wind DG at time t for s^{th} scenario of season se
V_{base}	Setting voltage magnitude base value
$v_{cri}^{low}/v_{cri}^{high}$	Specified low and higher bound for critical wind
V_{GC}^{spec}	Nominal specified voltage during grid-connected mode
V_i^{**}	Voltage reference for secondary control of the DDG at candidate bus i operated with droop/2nd
V_i^{*}	Voltage reference for primary control of the DDG at candidate bus i operated with droop/2nd
$\boldsymbol{v}_{se}^{gust}$	Vector containing 3-Second wind gust in proportional to $\boldsymbol{v}_{se}^{worst}$
$\boldsymbol{v}_{se}^{\boldsymbol{m}}$	Matrix constraining $\boldsymbol{v}_{s,se}^{\boldsymbol{m}}$ for season se
$\boldsymbol{v}_{se}^{worst}$	Vector of wind scenario contains the word wind speed in m/s
$\boldsymbol{W}_i$	Matrix of weight for i^{th} hidden layer of DNN architecture
w_i^{load}	Weighing coefficient of loads
$\boldsymbol{WT}_{sp}^{site}$	Vector containing the location of the WTs for sample sp
$\boldsymbol{WT}_{t}^{down}$	Vector containing the status of the WTs (i.e., $WT_{i,t,s,se}^{down}$) at time t
$\mathbf{Y}_{s,se}^{\mathbf{bus}}$	3D matrix containing the time couple admittance matrix $\mathbf{Y}_{t,s,se}^{\mathbf{bus}}$ at time t for s^{th} scenario of season se
$Z_{i,t,s,se}$	Time coupled impedance of branch i at time t for s^{th} scenario of season se
Z_i^0	Initial impedance value for branch i
$\boldsymbol{a}_{0,sp}^{\boldsymbol{dnn}}$	Vector input sample sp for DNN architecture
$\boldsymbol{a}_{i,sp}^{\boldsymbol{dnn}}$	Vector of neuron activation obtained by i^{th} hidden layer according to sample sp
$a_{i,t,s,se}^{br,new}$	Updated number for $a_{i,t,s,se}^{br}$ at time $t = t_{i,s,se}^{br,rep}$
$a_{i,t,s,se}^{br}$	Binary element represents the availability of branch i at time t of season se
$a_{sp}^{dnn'}$	Neuron activation obtained by the output-layer according to sample sp
η^{DDG}	Power efficiency of the DDG
η_i^{ES}	Efficiency of the energy storage
μ^{cond}, σ^{cond}	Mean and Standard deviation of the normal distribution for conductor's fragility curve
μ^{pole}, σ^{pole}	Mean and Standard deviation of the normal distribution for pole's fragility curve
$\pi^{br,nvul}$	Vulnerability threshold for distribution branch
$\pi_{i,t,se}^{br}$	Failure probability of the branch i at time t of season se, considering $\pi_{i,t,se}^{poles}$ and $\pi_{i,t,se}^{cond}$
$\pi_{i,t,se}^{cond}$	Failure probability for a conductor of branch i at time t of season se
$\pi_{i,t,se}^{Pole}$	Failure probability for single pole of branch i at time t of season se
$\pi_{i,t,se}^{poles}$	Failure probability considering all poles of branch i at time t of season se
$\pi_{s,se}^{wiso}$	Probability for both wind and solar scenario for s^{th} scenario of season se obtained by forward reduction technique
$\boldsymbol{\pi}_{se}$	Matrix in 3D format containing the failure probability $\pi_{i,t,se}^{br}$ for season se
σ^{curt}	Cost of load curtailment in \$/kWh
σ^{fuel}	Fuel cost for DDG in \$/kWh
$\sigma_{O\&M}^{DDG}$	Cost \$/kWh for O&M the DDG
$\sigma_{O\&M}^{ES}$	Cost \$/kWh/year for O&M the ES
$\sigma_{O\&M}^{ISW}$	Cost \$/year for O&M the ISW
$\sigma_{O\&M}^{PV}$	Cost \$/kWh/year for O&M the PV
$\sigma_{O\&M}^{WT}$	Cost \$/kWh/year for O&M the WT
$\sigma_{t,s,se}^{PCC}$	Market energy price in \$/kWh corresponding to time t for s^{th} scenario of season se
σ_{INS}^{ES}	Installation cost \$/kWh of ES at candidate bus i
$\sigma_{INV}^{ES,E}$	Investment cost \$/kWh for energy density rating for ES
$\sigma_{INV}^{ES,P}$	Investment cost \$/kW for power rating for ES
σ_{INV}^{DDG}	Investment cost for DDG in \$/kW
σ_{INV}^{PV}	Investment cost for PV in \$/kW
σ_{INV}^{SSW}	Investment cost in \$ per allocated ISW
σ_{INV}^{WT}	Investment cost for WT in \$/kW
Δt	Step time (i.e., 1 segment = 1 hour)

D. CONTINUOUS VARIABLES

$E_{i,t,s,se}^{ES}$	Energy SOC of the ES unit i at time t for s^{th} scenario of season se
$P_{k,t,s,se}^{br}$	Active power flowing across the transmission branch k at time t for s^{th} scenario of season se
$P_{i,t,s,se}^{ch}$	Active power charge by i^{th} ES unit at time t for s^{th} scenario of season se
$P_{i,t,s,se}^{dch}$	Active power discharge by i^{th} ES unit at time t for s^{th} scenario of season se
$P_{i,t,s,se}^{DDG}$	Active power generated by DDG i at time t for s^{th} scenario of season se
$P_{i,t,s,se}^{PCC}$	Active power imported/exported from/to the main grid across the i^{th} PCC of the MG at time t for s^{th} scenario of season se
$P_{i,t,s,se}^{PV,use}$	PV's adjusting power output and used at time t for s^{th} scenario of season se
$P_{i,t,s,se}^{WT,use}$	WT's adjusting power output used at time t for s^{th} scenario of season se

$Q^{br}_{k,t,s,se}$	Reactive power flowing across the transmission branch k at time t for s^{th} scenario of season se
$Q^{DDG}_{i,t,s,se}$	Reactive power generated by the i^{th} DDG unit at time t for s^{th} scenario of season se
$Q^{ES}_{i,t,s,se}$	Reactive power generate/receive of the i^{th} ES unit, at time t for s^{th} scenario of season se
$Q^{PCC}_{i,t,s,se}$	Reactive power exchange with the main grid across the i^{th} PCC of the MG at time t for s^{th} scenario of season se
$u^{v}_{i,t,s,se}$	Integrator output of secondary voltage restoration of i^{th} DDG unit operating with droop/2nd at time t for s^{th} scenario of season se
$V_{i,t,s,se}$	Voltage magnitude of the bus i at time t for s^{th} scenario of season se
$\delta_{i,t,s,se}$	Voltage magnitude angle of bus i at time t for s^{th} scenario of season se
$\delta^{MG}_{f^{bus}_{i,t},t,s,se}$	Phase angle of the frequency controllable bus $f^{bus}_{i,t}$ at time t for s^{th} scenario of season se
$\delta^{MG}_{t,s,se}$	Phase angle of the bus where the frequency control act at time t for s^{th} scenario of season se

E. INTEGER AND BINARY VARIABLES

$b^{curt}_{i,t,s,se}$	Binary variable for load curtailment (1: load shaded and 0: load fed) for bus i at time t for s^{th} scenario of season se
$b^{DDG,size}_{i}$	Integer variable for DDG allocation at candidate bus i
$b^{ES}_{i,t,s,se}$	Binary variable indicates the status of ES i.e. 1: discharge and 0: charge
$b^{ES,size}_{i}$	Integer variable for ES allocation at candidate bus i
b^{ISW}_{i}	Binary decision variable for ISW allocation at candidate branch i
$b^{PV,size}_{i}$	Integer variable for PV allocation at candidate bus i
$b^{WT,size}_{i}$	Integer variable for WT allocation at candidate bus i

F. FUNCTION AND METRIC

$AEMIS^{DDG}$	Annual CO_2 emission in kg/kWh/year according to DDGs generation
$AEMIS^{DDG,dl}$	$AEMIS^{DDG}$ based on DNN model
$AEMIS^{GRID}$	Annual CO_2 emission in kg/kWh/year according to power imported from main grid
$AEMIS^{GRID,dl}$	$AEMIS^{GRID}$ based on DNN model
$AEMIS^{OLEV}$	Total CO_2 emission, use as an objective function for the outer level problem
$AEMIS^{OLEV,dl}$	$AEMIS^{OLEV}$ based on DNN model
$AOMC^{DDG}$	Annual O&M cost for DDGs in \$/kWh/year
$AOMC^{DDG,dl}$	$AOMC^{DDG}$ based on DNN model
$AOMC^{ES}$	Annual O&M cost for ESs in \$/kWh/year
$AOMC^{ISW}$	Annual O&M cost for ISWs in \$/year
$AOMC^{PV}$	Annual O&M cost for PVs in \$/kWh/year
$AOMC^{WT}$	Annual O&M cost for WTs in \$/kWh/year
$C^{DDG,dl}$	C^{DDG} based on DNN model
$C^{CURT}_{t,s,se}$	Cost of energy curtailment during IS mode at time t for s^{th} scenario of season se
C^{DDG}	Total cost in \$ for DDGs considering TL
$C^{DDG}_{t,s,se}$	Cost of natural gas consumption by the DDG units at time t for s^{th} scenario of season se
C^{ES}	Total cost in \$ for ESs considering TL
C^{ISW}	Total cost in \$ for ISWs considering TL
$C^{PCC}_{t,s,se}$	Cost of energy imported from the substation across the PCC of the microgrid at time t for s^{th} scenario of season se
C^{PV}	Total cost in \$ for PVs considering TL
$C^{VI}_{t,s,se}$	Cost of voltage violation at time t for s^{th} scenario of season
$C^{VI,MGs}_{t,s,se}$	Cost of voltage violation considering MGs at time t for s^{th} scenario of season se
C^{WT}	Total cost in \$ for WTs considering TL
$CPC^{ES,E}$	Total capital cost for ESs in \$/kWh
$CPC^{ES,P}$	Total capital cost for ESs in \$/kW
CPC^{DDG}	Total capital cost for DDGs in \$/kW
CPC^{ISW}	Total capital cost for ISWs in \$
CPC^{PV}	Total capital cost for PVs in \$/kW
CPC^{WT}	Total capital cost for WTs in \$/kW
$EMIS^{DDG}_{s,se}$	Daily CO_2 emission in kg/kWh according to DDGs generation
$EMIS^{GRID}_{s,se}$	Daily CO_2 emission in kg/kWh according to power imported from main grid
$INSC^{ES}$	Installation cost in \$ for ESs
$OF^{MILP}_{s,se}$	Normalized objective function for MILP problem at time t for s^{th} scenario of season se
$OF^{MILP,MGs}_{s,se}$	Normalized objective function for MILP problem considering microgrid formations at time t for s^{th} scenario of season se
$OMC^{DDG}_{s,se}$	Pre-representation O&M cost for DDGs in kWh/day for s^{th} scenario of season se
$RESI$	Basic resilience index
$RESI^{OLEV}$	Resilience index considering SPF progression phase I and II, use as an objective function for the outer level problem.
$RESI^{OLEV,dl}$	$RESI^{OLEV}$ based on DNN model
TC^{OLEV}	Total cost in \$, use as an objective function of the outer level

$TC^{OLEV,dl}$	TC^{OLEV} based on DNN model
$TG_{sp,n}$	Target n for training DDN model corresponding to LOPF solution of sample sp
$\boldsymbol{X^{MILP}}$	Vector containing the decision variables for the MILP problem formulation
$\boldsymbol{X^{OLEV}}$	Vector containing the decision variables for the outer level problem

I. INTRODUCTION

Power distribution systems are currently undergoing a major transition toward sustainability. The key drivers for this transition include the need to control electricity costs to mitigate global climate change, enhance/replace aging infrastructure, and provide reliable service [1]. On the other hand, the increasing recurrence of extreme weather events is demanding significant changes to the distribution networks' operation and design. Extreme weather events can cause power outages in what would otherwise be a reliable distribution system. In fact, many distribution utilities worldwide are increasingly suffering from power outages due to High Impact Low Probability (HILP) events. For instance, in the ten years from 2003 to 2013 more than 70 million customers in the United States were affected by HILP events [2]. In order to address this issue, major efforts toward distribution system resilience enhancement have been introduced recently. In this context, resilience generally refers to the ability of the system to anticipate and withstand extreme HILP events, allowing for a rapid recovery from possible interruptions due to the event [3]. To date, power distribution utilities are on the lookout for practical solutions to increase their distribution systems' resiliency, allowing for continuous supply for critical loads, e.g., hospitals and data centers, during HILP events [4]. To this end, resilience enhancement solutions have been recently put forward in the literature. Generally, these solutions can be categorized into 1) planning and infrastructure-oriented strategies, and 2) operational strategies. The first kind of solution mainly focuses on preventive actions to protect the power distribution system against contingencies that may arise due to HILP events, e.g., distributed energy resource (DER) allocation [5], optimal sizing [6] and hardening [7]. On the other hand, operational strategies seek to improve the load restoration ability in case of a HILP event, e.g., pro-active operation [8], network configuration [9], and microgrids (MGs) formation [10].

The concept of microgrids planning for resilience enhancement was recently introduced in the literature. The majority of the work in this area opted for a multi-stage optimization problem for delivering the optimal resilience enhancement solutions. Generally, the outer level is dedicated to the investment decisions pertaining to the planning elements. On the other hand, the inner level deals with the microgrids operation strategy to hedge the contingencies as well as to consider the microgrids operation and control behavior. In [11], the authors proposed a two-stage model for planning microgrids considering both economics and resilience enhancement. In this work, the determination of the optimal site/size of the DERs and the backup distribution lines were considered. The problem was formulated as a master/sub-problem and solved iteratively. The master problem focused on deploying DERs and distribution lines while the sub problem identified the extreme events scenarios allowing for up to N-3 contingencies. The solution delivered by this method improved the ability of the microgrids to restore the power supply to loads during contingencies using either DERs or backup distribution lines. Still, this work lacked in terms of accounting for the AC optimal power flow representing the microgrid operation with hierarchical control. In [12] a stochastic planning model was proposed for enhancing the distribution systems' resilience using a microgrid formation strategy. The proposed method was formulated as a multiple-stage optimization model. The upper stage dealt with the optimal line hardening and distributed generation (DG) allocation while the lower stage dealt with the optimum operation strategies,i.e., network reconfiguration, microgrids formation and demand-side management. This work considered the uncertainty of loads as well as the uncertainty of the damage in the feeders caused by the weather events. Still, this work only considered dispatchable DG units. Renewable energy resources and energy storage units were not considered. Additionally, the microgrid hierarchical control structure was not considered in modeling the microgrid operation. The work in [6] focused on developing a planning model for the optimal sizing of isolated networked MGs considering the trade-off between economics and resilience enhancement. In this work, the problem was formulated as a three-level, wherein the first level focused on the optimal sizing of the DERs and energy storage considering the normal operation (without contingencies). The second level coordinated with the third level allowed for considering both normal operation and emergency operation of isolated networked MGs. For each level, the AC optimal power flow has been used for delivering the minimum of the generation cost, load shedding, or both according to the operation condition (i.e., normal and emergency). A time-coupled AC optimal power flow has been simulated for 4 representative days to allow for the uncertain characteristics of the seasonal load profile. Still, renewable energy resources were not considered in this work. Moreover, the location of the DERs and storage were pre-predetermined a priori to the solution. Authors in [13] proposed the optimal sizing of mobile energy storage system in networked MGs. This work considered renewable energy resources, i.e., photovoltaic (PV), wherein different scenarios were adopted for considering the uncertain characteristic of the PV generation as well as the load. Still, the microgrid hierarchical control structure was not considered in modeling the microgrid operation. Moreover, this problem was limited to the optimal sizing and placement of mobile energy storage, while the location and size of PV and DGs were pre-predetermined a priori.

In regards to the existing resilience-oriented microgrids planning methodologies, one of the main concerns is the

computational burden. Attempting to manage their computational burden, existing work endeavored to minimize the problem size by omitting renewable energy resources, prespecifying the location of some resources, neglecting the microgrid hierarchical control structure, and/or considering a limited number of stochastic scenarios. While these techniques can reduce the problem size, they on the other hand render the planning problem incomplete and only applicable to particular planning instances. As a possible solution to this problem, the concept of deep learning can provide an attractive solution for handling computationally demanding problems, i.e., its ability to significantly increase the computation performance of large scale analysis/optimization problems make their solution more attainable in comparison to traditional methods. For instance, the concept of deep learning has been applied for in the development of power flow and optimal power flow tools, respectively, [14] and [15]. In these works, the deep learning technique was used for enhancing the performance and computation efficiency of the power flow/optimal power flow solution approach. Still, the concept of AC microgrids considering hierarchical control solutions has not been introduced in this work and making its application not appropriate for microgrid planning problems. On the other hand, the work in [16], proposes the use of deep learning for the restoration problem of critical loads after experiencing a major outage. In this work, the deep Q-learning method is applied for speeding up the solution approach, making the problem solvable for small distribution system up to large-scale network. However, there is no consideration of the microgrid concept and its planning in this work. Next, a new planning problem based on deep learning for a resilient transmission system is introduced in [17]. In this work, a deep learning technique is adopted to forecast the load growth while improving the forecasting task compared to an existing method. Still, the concept of microgrids is also not introduced in this work. Recently, in [18], the concept of microgrid has been introduced while coordinating several renewable resources and Plug-In Hybrid Electric Vehicles (PHEVs). In this work, the deep learning technique is adopted to forecast the renewable output seeking to mitigate the uncertainty caused by the renewable energy elements in the microgrid. While the deep learning technique is adopted in this work, this work only discusses the operation stage and presents a simplified problem by omitting the hierarchical control philosophy of the microgrid in its problem formulation.

Considering the abovementioned advancements and current challenges described in the literature, in this work, a new general framework for resilience-oriented microgrid(s) planning is proposed exploiting deep learning technique ability to alleviate the computational burden associated with planning problem without sacrificing modelling accuracy. The remainder of this paper is organized as follows: First, a basic outline for the proposed resilience-oriented microgrid planning framework is presented in Section II. Subsequently, the problem formulation for the outer and inner levels is described in Section III. Then, the data preparation stage for the proposed planning approach is presented in Section IV. Next, the deep learning approach for a stochastic optimal operation level is discussed in Section V. Later, Section VI exhibits the details of the optimal microgrid planning approach Non-dominated Sorting Genetic Algorithm II (NSGA-II) based deep neural network (DNN) models. Finally, sections VII and VIII present the results and conclude the paper, respectively.

II. PROPOSED RESILIENCE-ORIENTED PLANNING FRAMEWORK

The availability of isolate switches (ISWs) along with the locations and capacities of the DERs, including DG units, renewable DG units and energy storage (ES) units, are salient for the successful creation of MG(s) in a distribution network. Additionally, the optimal operation of the MG's resources should be considered to ensure the MG successful operation, minimize its operational costs and maximize its resilience. As such, the proposed resilience-oriented planning framework seeks to identify the optimal allocation of DERs and ISWs in a distribution network considering the optimal operation of the MG(s) that will be created using these components. To this end, the analyzed problem is formulated as a stochastic bilevel optimization framework. First, an outer level featuring a metaheuristic multi-objective optimization is adopted for the optimal allocation of the DERs and ISWs seeking to balance the competing objectives of cost, resilience and environmental impact. Then, an inner level is proposed to handle the optimization problem pertaining to the optimal operation of the MG(s) that can be created by the DERs and ISWs allocated in the outer level. The problem of the MG's optimal operation is cast as a linear optimum power flow (LOPF) problem. In this work, the adopted LOPF model considers the operational behavior of the MG in both grid-connected (GC) and islanded (IS) modes of operation. Additionally, different scenarios are considered to account for the stochastic nature of the HILP events, as well as renewable DG units. In this sense, despite using a LOPF model, the detailed modeling of MGs and consideration of different stochastic scenarios in the inner level along with the metaheuristic nature of the outer level make solving the LOPF, for each of the stochastic scenarios for each individual in the metaheuristic optimization's population, using a numerical optimization solver computationally challenging. In other words, the combination of the need for numerous iterations to solve the LOPF of the inner level and the large populations from the metaheuristic presented in the outer level before reaching the final planning solution, make this problem computationally extremely demanding that it may be unsolvable with the traditional analytical methods. In this sense, in this work, a deep learning technique is adopted for deriving the information required from the LOPF solution for the stochastic scenarios under consideration. With this technique, DNN models are developed and trained to predict the solution delivered by the inner level that comprises the LOPF solution with the numerous stochastic scenarios, significantly

reducing the computation burden, and thus eliminating the possible requirement for modelling simplication. This new perspective provides an effective strategy for solving MG planning framework, overcoming computation constraints that limit the consideration of detailed systems' modeling and scenarios, which are especially critical features for guaranteeing feasible solutions under a resilience-oriented outlook.

The proposed planning framework comprises four cascading stages for delivering the final optimal allocation of the DERs and switches. 1) The first stage is concerned with data preparation. In this stage, the distribution system under consideration and its planning elements are identified along with the uncertainty scenarios describing the stochastic nature of the system and the planning elements. The target system for this work is a typical distribution system with the ability to disconnect from the main grid via a main isolate switch, denoted by ISW^{sub}. The planning elements include dispatchable distributed generation (DDG), wind turbine (WT), PV, ES and ISW. Candidate buses and branches are specified as potential locations for the system's planning elements. Stochastic scenarios are considered for allowing for the uncertainty associated with the MG(s) creation, i.e., HILP, and operation (renewable generation and load). These uncertainty scenarios are seasonal and include a set of scenarios representing the normal operation of the system and another set of scenarios representing the severe HILP events in which N-K contingencies occurred in the network within a certain time interval. 2) The second stage corresponds to the problem formulation of the proposed stochastic bilevel optimization framework. In this formulation, the outer level's objective functions are cost, resilience and environmental metrics (indices) that depend on the solution of LOPF for different stochastic scenarios in the inner level. 3) The third stage seeks to deliver the deep learning models that are used to determine the stochastic LOPF dependent indices required for the outer level. To this end, a set of sample DERs and switches allocation is developed considering randomly generated combinations of possible installation decisions for the candidate planning elements' locations and capacities. Next, the stochastic LOPF is solved using a numerical optimization solver for each of the allocation samples under consideration for each of the stochastic scenarios. Based on the LOPF solutions obtained for these samples, the outer level cost, resilience and environmental indices are calculated. The calculated indices are considered the target values of the allocation samples. The allocation samples and their corresponding target values are then employed for training the DNN models that map the planning elements installation decisions to the outer level's cost, resilience and environmental indices. Finally, in the fourth stage, the optimal planning approach is held. Using a population-based metaheuristic optimization exploiting the DNN models derived in the third stage, the optimal solution describing the optimal allocation of DERs and ISWs is determined by respecting the optimal trade-off between the multi-objective functions, i.e., resilience, economic and environmental impact. Each of these four stages is individually addressed in the following sections.

III. STAGE 1: DATA PREPARATION

In this section, the first stage responsible for data preparation is addressed, including the modeling of the distribution system and planning elements, as well as generation uncertainty, normal operation and HILP event scenarios.

A. DISTRIBUTION SYSTEM AND PLANNING ELEMENTS

The distribution system considered in this work is a typical distribution network with the ability to disconnect from the main grid via a main ISW^{sub} located at the upstream interfacing substation. Candidate buses and branches for the installation of DERs and isolation switches, respectively, are assumed to be selected arbitrarily by the distribution system operator (DSO). The planning elements include the DDGs, WTs, PVs, ESs and ISWs. In GC mode, the DDGs are controlled to inject constant amounts of power prespecified by a higher level control layer typically seeking to realize an economic benefit [19]. On the other hand, in the islanding mode of operation, the DDGs are controlled using primary droop mode with a supervisory secondary control layer (droop/2^{nd}) control to follow the load variation and maintain the system voltage and frequency within adequate bounds, allowing for quick synchronization back with the main grid when it is ready. The WTs and PVs are intermittent resources and are as such operated in power control mode to allow for maximum power tracking. The ESs are interfaced with a power electronic inverter and are controlled in a power control mode to inject/absorb power from the microgrid as needed. The ISWs are used to isolate faults according to the considered N-K contingencies.

B. WT AND PV GENERATION MODEL

The power generated by the WTs and PVs depends on the wind velocity and solar irradiance, respectively, and can be modeled using (1) and (2) similar to the work in [20].

$$P^{WT}_{i,t,s,se} = \begin{cases} 0, & v^{m}_{i,t,s,se} < v^{ci}_{i},\ v^{m}_{i,t,s,se} \geq v^{co}_{i} \\ P^{WT,size}_{i} \dfrac{\left(v^{m}_{i,t,s,se} - v^{ci}_{i}\right)}{\left(v^{ra}_{i} - v^{ci}_{i}\right)}, & v^{ci}_{i} \leq v^{m}_{i,t,s,se} \leq v^{ra}_{i} \\ P^{WT,size}_{i}, & v^{ra}_{i} < v^{m}_{i,t,s,se} < v^{co}_{i}, \end{cases}$$
$$\forall i \in \Omega^{can}_{WT}, \quad \forall t \in \Omega_{T}, \ \forall s \in \Omega'_{s} \cup \Omega''_{s}, \ \forall se \in \Omega_{se} \tag{1}$$

$$P^{PV}_{i,t,s,se} = \begin{cases} P^{PV,size}_{i} \left(r^{m}_{i,t,s,se}\right)^{2} \Big/ \left(R^{STD}_{i} - R^{C}_{i}\right), & r^{m}_{i,t,s,se} \leq R^{C}_{i} \\ P^{PV,size}_{i} \left(r^{m}_{i,t,s,se}\right)^{2} \Big/ R^{STD}_{i}, & R^{C} < r^{m}_{i,t,s,se} < R^{STD}_{i} \\ P^{PV,size}_{i}, & r^{m}_{i,t,s,se} \geq R^{STD}_{i}, \end{cases}$$

$$\forall i \in \Omega_{PV}^{can}, \quad \forall t \in \Omega_T, \ \forall s \in \Omega_s' \cup \Omega_s'', \forall se \in \Omega_{se} \tag{2}$$

where, $P_{i,t,s,se}^{WT}$ denote an active power generated by i^{th} WT unit at time t for s^{th} scenario of season se. $P_i^{WT,size}$ is the active power rating of WT unit at candidate bus i. $v_{i,t,s,se}^{m}$ denote a measured wind speed of the i^{th} WT unit at time t for s^{th} scenario of season se. Then, v_i^{ci}, v_i^{co} and v_i^{ra} denotes cut-in, cut-out, and the rated speed of the i^{th} WT unit, respectively. Ω_{WT}^{can} is the set of candidate buses for WT units. Ω_T is the set of time segment in planning horizon. Ω_s', Ω_s'' and Ω_{se} are the set of generated scenarios for normal situation, severe situation and seasonal periods, respectively. Then, for (2), $P_{i,t,s,se}^{PV}$ denote an active power generated by i^{th} PV unit at time t for s^{th} scenario of season se. $P_i^{PV,size}$ denote the active power rating of PV unit at candidate bus i. $r_{i,t,s,se}^{m}$ denote a measured solar radiation in kW/m^2 of the i^{th} PV unit at time t for s^{th} scenario of season se. R_i^{STD} and R_i^{C} are the solar radiation in standard test conditions and certain solar radiation point of the i^{th} PV unit, respectively. Ω_{PV}^{can} is the set of candidate buses for PV units.

In this work, it is assumed that the WTs and PVs are operating with a unity power factor. Thus, there is no reactive power injected by these units leading to (1) and (2) exclusively representing active power relations.

C. LOAD MODEL

The varying seasonal behavior of the loads is modeled using the annual peak load pattern [21]. In this sense, the load on bus $i \in \Omega_{BUS}$ at time $t \in \Omega_T$ can be calculated as the multiplication between the peak demand at this bus and the annual peak load factor at time $t \in \Omega_T$ for the season under consideration. The active and reactive power demand for bus i at time t for scenarios s and season se can be calculated using (3) and (4).

$$\begin{aligned} P_{i,t,s,se}^{L} &= \left(APL_{t,s,se}/100\right) \times P_{i,t,s,se}^{L,peak}, \\ &\forall i \in \Omega_{BUS}, \quad \forall t \in \Omega_T, \ \forall s \in \Omega_s' \cup \Omega_s'', \\ &\forall se \in \Omega_{se} \end{aligned} \tag{3}$$

$$\begin{aligned} Q_{i,t,s,se}^{L} &= \left(APL_{t,s,se}/100\right) \times Q_{i,t,s,se}^{L,peak}, \\ &\forall i \in \Omega_{BUS}, \quad \forall t \in \Omega_T, \ \forall s \in \Omega_s' \cup \Omega_s'', \\ &\forall se \in \Omega_{se} \end{aligned} \tag{4}$$

where, $P_{i,t,s,se}^{L}$ and $Q_{i,t,s,se}^{L}$ are the active and reactive power load for bus i at time t for s^{th} scenario of season se. Then, $P_{i,t,s,se}^{L,peak}$ and $Q_{i,t,s,se}^{L,peak}$ denotes original active and reactive peak load from data sheet of bus i at time t for s^{th} scenario of season se. $APL_{t,s,se}$ is an annual peak load pattern in percentage at time t for s^{th} scenario of season se. Ω_{BUS} is the set of buses in the test system.

D. OPERATION SCENARIOS

Given the resilience-based planning perspective of the proposed work, two sets of scenarios have been considered. First, scenarios representing normal system operations without contingencies are addressed. Second, scenarios representing severe HILP events, in which N-K contingencies occur during a certain time interval are tackled. These scenario generation processes are described in the following subsections.

1) NORMAL OPERATION SCENARIOS

In the normal operation scenarios, the system is assumed to operate in GC mode considering uncertainties associated with the renewable resources. For this, historical data sets comprising different 24-hours time series of wind speeds and solar irradiance are considered. Next, based on this data a fast forward reduction approach is employed [22], extracting a number of normal scenarios (N_s') per season representing the uncertainty associated with the renewable resources. This step seeks to avoid the higher computation burden, while keep a good approximation of the system. The wind speed and solar irradiance in a given scenario s can be expressed by (5) and (6), respectively.

$$\boldsymbol{v_{s,se}^{m}} = [v_{1,s,se}^{m}, v_{2,s,se}^{m}, \ldots, v_{N_T,s,se}^{m}], \quad \forall s \in \Omega_s', \ \forall se \in \Omega_{se} \tag{5}$$

$$\boldsymbol{r_{s,se}^{m}} = [r_{1,s,se}^{m}, r_{2,s,se}^{m}, \ldots, r_{N_T,s,se}^{m}], \quad \forall s \in \Omega_s', \ \forall se \in \Omega_{se} \tag{6}$$

where, $\boldsymbol{v_{s,se}^{m}}$ and $\boldsymbol{r_{s,se}^{m}}$ are the vectors constraining $v_{t,s,se}^{m}$ and $r_{t,s,se}^{m}$ for s^{th} scenario of season se, respectively. Then, N_T denote planning horizon time.

2) SEVERE HILP OPERATION SCENARIOS

For scenarios representing the operation of the distribution system under severe HILP events, a similar approach to the work developed in [23] is employed. In this sense, by using the component availability matrix **AV**, the availability of the different system components (e.g., branch) at different time segments in the planning horizon is depicted. This matrix allows for the identification of the contingency level, as well as the fault location(s) at any instant in the planning horizons. This in turn enables the development of effective microgrid formation solutions that can meaningfully improve distribution system resiliency. For considering the distribution system operation under severe HILP events, the following assumptions are made in this work:

1) Severe wind events are considered the main source of contingencies affecting the distribution network, similar to the work developed in [23].
2) Only overhead lines are considered to be vulnerable to severe winds. Distribution substations and underground lines are able to withstand severe winds as depicted in [24].
3) The distribution system buses are assumed to be geographically close enough that the trajectory of the wind passing through the distribution network causes the entire network to be exposed to the same weather conditions [25].

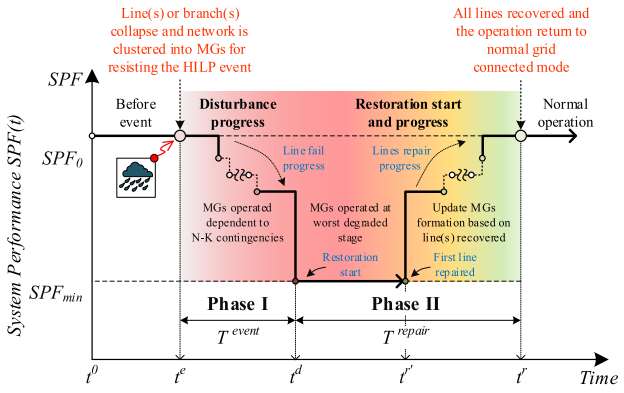

FIGURE 1. Evolution of network's system performance during a severe event.

a: SYSTEM PERFORMANCE ANALYSIS FOR HILP SCENARIOS SELECTION

Next, considering the aforementioned assumptions, when a severe wind event arises, the supply availability and the corresponding system performance progress through multiple phases along Ω_T, leading to the typical progression curve for the system performance (SPF) during a severe event depicted in Fig. 1 [3], [23]. In this perspective, the system performance can be represented as a function of the electricity supply level at time t, being divided into Phase I and II, where Phase I represents the disturbance progress period between the event start, t^e, and maximum system degradation state, t^d, i.e. $T^{event} = t^e - t^d$, and Phase II depicts the recovery period between the maximum degradation time until reparations conclusion, i.e., $T^{repair} = t^d - t^r$. Here it is important to note that there is typically a lead time in Phase II between the moment where the event disturbance progression stops and the time where repairs' impact is effectively observed, i.e., $t^{r'}$.

Detailed descriptions of Phase I and II leading to the developed weather-related algorithm for HILP scenarios selection and component availability matrix **AV** derivation are following presented.

b: PHASE I: DISTURBANCE PERIOD

Assuming the event start and progression, during Phase I the affected system clusters into multiple MGs with topologies respecting local resources availability and ISWs allocated in the network. The formation of MGs allows the system to improve its withstanding ability against the N-K contingencies caused by the severe wind and enhance the maintenance of the loads' service. In this sense, given this work focus on resilience-based planning, the single most vulnerable wind scenario needs to be identified for each season in order to stress the system performance under worst-case condition, i.e., $\boldsymbol{v}_{se}^{worst}$. For this, based on works [26], [27] wind gusts can be calculated using (7), where the system's most vulnerable scenario under a resilience perspective is given by the wind scenario within the matrix $\mathbf{v}_{se}^{\mathbf{m}}$ containing the highest wind

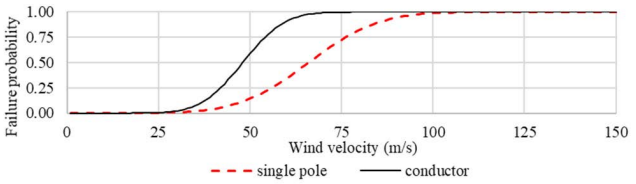

FIGURE 2. Generic fragility curve for single pole and conductor against wind gust.

velocity.

$$\boldsymbol{v}_{se}^{gust} = k^{gust}\boldsymbol{v}_{se}^{worst}, \quad \forall se \in \Omega_{se} \tag{7}$$

where, $\mathbf{v}_{se}^{\mathbf{m}}$ is a matrix constraining $\boldsymbol{v}_{s,se}^{\boldsymbol{m}}$ for season se. $\boldsymbol{v}_{se}^{gust}$ is a vector containing 3-Second wind gust in proportional to $\boldsymbol{v}_{se}^{worst}$. Then, k^{gust} is the constant factor for calculating $\boldsymbol{v}_{se}^{gust}$.

Following, the failure probability of overhead lines for season se can be extracted by mapping poles and conductors' fragility curve for the calculated wind gust profile $\boldsymbol{v}_{se}^{gust}$. The fragility curve can be generated using the normal cumulative distribution function as generically illustrated in Fig. 2 for the distribution overhead line depicted in [24].

Here, it is worth noting that a branch fails if a conductor, or any pole overhead line, connected between two adjacent nodes fails. In this sense, the total failure probability of the distribution overhead line should be calculated using (8a)-(8d).

$$\pi_{i,t,se}^{pole}\left(v_{t,se}^{gust}\right) = cdf^{nor}(v_{t,se}^{gust}, \mu_i^{pole}, \sigma_i^{pole}), \quad \forall i \in \Omega_{LIN},\ \forall t \in \Omega_T,\ \forall se \in \Omega_{se} \tag{8a}$$

$$\pi_{i,t,se}^{cond}\left(v_{t,se}^{gust}\right) = cdf^{nor}(v_{t,se}^{gust}, \mu_i^{cond}, \sigma_i^{cond}), \quad \forall i \in \Omega_{LIN},\ \forall t \in \Omega_T,\ \forall se \in \Omega_{se} \tag{8b}$$

$$\pi_{i,t,se}^{poles}\left(v_{t,se}^{gust}\right) = 1 - \left[\left(1 - \pi_{i,t,se}^{pole}\left(v_{t,se}^{gust}\right)\right)^{N_i^{pole}}\right], \quad \forall i \in \Omega_{LIN}, \forall t \in \Omega_T, \forall se \in \Omega_{se} \tag{8c}$$

$$\pi_{i,t,se}^{br}\left(v_{t,se}^{gust}\right) = \begin{pmatrix} \pi_{i,t,se}^{cond}\left(v_{t,se}^{gust}\right) + \pi_{i,t,se}^{poles}\left(v_{t,se}^{gust}\right) \\ -\pi_{i,t,se}^{cond}\left(v_{t,se}^{gust}\right) \times \pi_{i,t,se}^{poles}\left(v_{t,se}^{gust}\right) \end{pmatrix}, \quad \forall i \in \Omega_{LIN}, \forall t \in \Omega_T, \forall se \in \Omega_{se} \tag{8d}$$

where, $\pi_{i,t,se}^{pole}$ and $\pi_{i,t,se}^{cond}$ denotes the failure probability for a single pole and conductor of branch i at time t of season se. cdf^{nor} (.) denote a normal cumulative distribution function. Then, μ^{pole}, σ^{pole}, μ^{cond} and σ^{cond} denotes the mean and standard deviation of cdf^{nor} (.) for pole and conductor's fragility curve. Next, N_i^{pole} denote number of the poles according to span length of branch i. While, $\pi_{i,t,se}^{poles}$ in which denote a failure probability considering N_i^{pole} of branch i at time t of season se. At the end, $\pi_{i,t,se}^{br}$ is a failure probability of the branch i at time t of season se, considering $\pi_{i,t,se}^{poles}$ and $\pi_{i,t,se}^{cond}$. In this work, a set of lines or branches in the test system denoted by Ω_{LIN}.

In this case, eqs. (8a) and (8b) define the failure probability for a single pole and conductor during $v_{t,se}^{gust}$ based on

the normal cumulative distribution function with parameter $\mu^{pole}, \sigma^{pole}, \mu^{cond}$ and σ^{cond}. Eqs. (8c) and (8d) determine the general formulation for dealing with the failure probability of branch i according to the number of poles N_i^{pole} for the overhead line of branch i, assuming that the poles and conductor in the distribution system have the same characteristics and age. For this, N_i^{pole} can be estimated based on the span length of the distribution overhead line [28]. For distribution systems, the span length is typically between 100 ft to 150 ft, significantly shorter when compared to those used for the transmission system [29].

The failure probability obtained for the branches is stored in 3D matrix $\boldsymbol{\pi}_{se}$ (9). Next, similar to the work in [24], non-vulnerable branches are identified and disregarded by $\boldsymbol{\pi}_{se} = 0 | \boldsymbol{\pi}_{se} \left(\pi^{br}_{i,t,se} < \pi^{br,nvul} \right)$. Where, $\pi^{br,nvul}$ denote a vulnerability threshold for distribution branch. Following, for enlarging the possibility space of N-K contingencies, N_s^{pre} scenarios of **AV** are generated and represented by $\mathbf{AV}^{\mathrm{I}}_{s,se}$ considering Phase I. Where, N_s^{pre} denote a number pre-scenarios for severe situations considering only network SPF pregression phase (i.e., $t^e \rightarrow t^d$).

$$\boldsymbol{\pi}_{se}\left(\boldsymbol{v}^{gust}_{se}\right) = \begin{bmatrix} \pi^{br}_{i,t,se} & \cdots & \pi^{br}_{i,N_T,se} \\ \vdots & \ddots & \vdots \\ \pi^{br}_{n_{br},t,se} & \cdots & \pi^{br}_{n_{br},N_T,se} \end{bmatrix}, \quad \forall se \in \Omega_{se} \tag{9}$$

$$\mathbf{AV}^{\mathrm{I}}_{s,se} = \begin{bmatrix} a^{br}_{i,t,s,se} & \cdots & a^{br}_{i,N_T,s,se} \\ \vdots & \ddots & \vdots \\ a^{br}_{n_{br},t,s,se} & \cdots & a^{br}_{n_{br},N_T,s,se} \end{bmatrix}, \quad \forall i \in \Omega_{LIN}, \quad \forall t \in \Omega_T, \ \forall s \in \Omega_s^{pre}, \ \forall se \in \Omega_{se} \tag{10}$$

where, $a^{br}_{i,t,s,se}$ is 0 if the i^{th} branch fails at time t for scenario s of season se, otherwise, $a^{br}_{i,t,s,se} = 1$. $a^{br}_{i,t,s,se}$ can be determined by comparing the failure probability $\pi^{br}_{i,t,se}$ to the generated uniformed random binary number (i.e., $r_{i,t,s}$), as expressed by (11).

$$a^{br}_{i,t,s,se} = \begin{cases} a^{br}_{i,t-1,s,se} \times 1, & \pi^{br}_{i,t,se} \le r_{i,t,s} \\ a^{br}_{i,t-1,s,se} \times 0, & \pi^{br}_{i,t,se} > r_{i,t,s}, \end{cases} \quad \forall i \in \Omega_{LIN}, \quad \forall t \in \Omega_T, \ \forall s \in \Omega_s^{pre}, \ \forall se \in \Omega_{se} \tag{11}$$

c: PHASE II: RESTORATION PERIOD

Once the system reaches the maximum degradation condition, Phase II begins repairing the system until all branches are fully recovered at t^r and the system is back to normal operation, i.e., grid connected. In this sense, considering the time to repair (TTR) overhead lines dependency on the wind velocity at the time of failure, i.e., $t = t^{br,fail}_{i,s,se}$ [23], while aware that due to safety reasons, there are no repair actions implemented until the end of the event at $t^d_{s,se}$ [23]. The weather-related restoration time expressed by (12a) and (12b) is employed for determining TTR, and $\varphi^{br}\left(v^{gust}_{t,s,se}\right)$ is determined using uniform distributed sampling $\varphi \sim U[h_1, h_2]$ as depicted in (12c) [23], [30]. Once $\boldsymbol{TTR}^{\boldsymbol{br,fail}}_{s,se}$ and $t^d_{s,se}$ are determined, the recovered time for a single branch i can be determined by $t^{br,rep}_{i,s,se} = t^d_{s,se} + TTR^{br,fail}_{i,s,se}$. Thus, at $t^{br,rep}_{i,s,se}$, $a^{br}_{i,t,s,se}(t^{br,rep}_{i,s,se}) = a^{br,new}_{i,t,s,se} = 1$, which represents that branch i is recovered and turned back to the online state. Finally, the branch availability matrix considering Phase I and II $\mathbf{AV}^{\mathbf{I-II,orig}}_{s,se}$ can be obtained updating $\mathbf{AV}^{\mathrm{I}}_{s,se}$ with the new $a^{br,new}_{i,t,s,se}$ information as shown in (12a)-(12d).

$$\boldsymbol{TTR}^{\boldsymbol{br,fail}}_{s,se} = \left[TTR^{br,fail}_{1,s,se}, TTR^{br,fail}_{2,s,se}, \ldots, TTR^{br,fail}_{n_{br},s,se} \right], \quad \forall s \in \Omega_s', \quad \forall se \in \Omega_{se} \tag{12a}$$

$$TTR^{br,fail}_{i,s,se} = round\left(\varphi^{br}\left(v^{gust}_{t=t^{br,fail}_{i,s,se},s,se} \right) . MTTR^{nw} \right), \quad \forall i \in \Omega^{fail}_{LIN}, \quad \forall s \in \Omega^{pre}_s, \ \forall se \in \Omega_{se} \tag{12b}$$

$$\varphi^{br}\left(v^{gust}_{t,s,se}\right) = \begin{cases} 1, & if \ v^{gust}_{t,s,se} < v^{low}_{cri} \\ \varphi \sim U[h^{low}_1, h^{low}_2], & if \ v^{low}_{cri} \le v^{gust}_{t,s,se} \le v^{high}_{cri} \\ \varphi \sim U[h^{high}_1, h^{high}_2], & if \ v^{gust}_{t,s,se} > v^{high}_{cri}, \end{cases} \quad \forall i \in \Omega^{fail}_{LIN}, \quad \forall s \in \Omega^{pre}_s, \ \forall se \in \Omega_{se} \tag{12c}$$

$$\mathbf{AV}^{\mathbf{I-II,orig}}_{s,se} = \begin{bmatrix} a^{br}_{1,1,s,se}, a^{br,new}_{1,t=t^{br,rep}_{i,s,se},s,se}, \ldots, a^{br,new}_{1,N_T,s,se} \\ a^{br}_{2,1,s,se}, a^{br,new}_{2,t=t^{br,rep}_{i,s,se},s,se}, \ldots, a^{br,new}_{2,N_T,s,se} \\ \vdots \\ a^{br}_{n_{br},1,s,se}, a^{br,new}_{n_{br},t=t^{br,rep}_{i,s,se},s,se}, \ldots, a^{br,new}_{n_{br},N_T,s,se} \end{bmatrix}, \quad \forall s \in \Omega_s^{'',orig}, \quad \forall se \in \Omega_{se} \tag{12d}$$

where, $\boldsymbol{TTR}^{\boldsymbol{br,fail}}_{s,se}$ is a vector TTR containing $TTR^{br,fail}_{i,s,se}$. Whereas, $TTR^{br,fail}_{i,s,se}$ denote a time to repair of the failure branch i for s^{th} scenario of season se. $t^{br,fail}_{i,s,se}$ is a time corresponding to the moment when branch i fail for s^{th} scenario of season se. $MTTR^{nw}$ denotes a specified mean time to repair under normal weather conditions. v^{low}_{cri} and v^{high}_{cri} are the specified low and higher bound for critical wind. Then, h^{high}_1/h^{high}_2 are the pre-determined range for determining φ^{br} for the case corresponding to higher wind $v^{gust}_{t,s,se} > v^{high}_{cri}$, while h^{low}_1/h^{low}_2 are for the case corresponding to $v^{low}_{cri} \le v^{gust}_{t,s,se} \le v^{high}_{cri}$. Next, $t^{br,rep}_{i,s,se}$ denote a time t when branch recovered or repared for s^{th} scenario of season se, while $a^{br,new}_{i,t,s,se}$ is an updated number for $a^{br}_{i,t,s,se}$ at time $t = t^{br,rep}_{i,s,se}$. Ω^{fail}_{LIN} is a set of failure branches in the test system. Ω^{pre}_s is a set of generated pre-scenarios for severe situations considering only network SPF progression phase I (i.e., $t^e \rightarrow t^d$). $\Omega_s^{'',orig}$ is an original set before

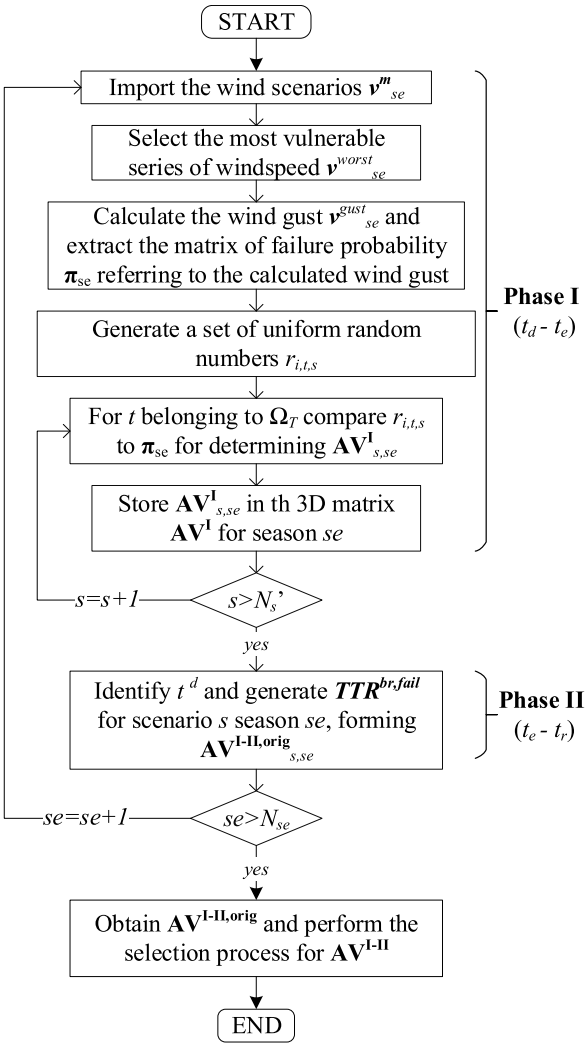

FIGURE 3. Weather-related algorithm for generating branch availability matrix.

reduction of generated scenarios for severe situation considering network SPF progression phase I and II (i.e., $t^e \rightarrow t^r$).

Next, the highest impact scenarios are determined for each season se until reaching the desired number of samples, i.e., $N - \left(K^{HI}_{s,se}\right)$ are chosen first, where $N - \left(K_{s,se}\right)$ denotes N-K contingencies for scenarios s, se, $K_{s,se}$ corresponds to the number of fault locations that occurred in the network for scenarios s, se. In case the highest impact selected scenarios do not reach the expected number of samples, available space(s) are fulfilled by the scenarios $N - \left(K^{HI}_{s,se} - 1\right)$, then $N - \left(K^{HI}_{s,se} - 2\right)$ until the N-1 contingency. The procedure for generating the **AV** matrix is illustrated in Fig. 3.

$$\mathbf{AV}^{\mathbf{I-II}}_{s,se} = \mathbf{AV}^{\mathbf{I-II,orig}}_{s,se}\{N - (K)\}, \quad \forall s \in \Omega''_s, \quad \forall se \in \Omega_{se} \tag{13}$$

where, $\mathbf{AV}^{\mathbf{I-II}}_{s,se}$ is the reduction version of $\mathbf{AV}^{\mathbf{I-II,orig}}_{s,se}$.

IV. STAGE 2: PLANNING PROBLEM FORMULATION

In this section, the problem formulation is detailed for both outer and lower levels, including respective discussions on objective functions, constraints, and decision variables.

A. OUTER LEVEL: OPTIMAL ALLOCATION LEVEL

The outer level problem formulation is responsible for the allocation of the planning elements including the DDGs, WTs, PVs, ESs and ISWs. For this, the following multi-objective problem formulations are developed.

1) OBJECTIVE FUNCTION - OUTER LEVEL

The multi-objective function for the outer level considers three main perspectives, i.e., 1) resilience enhancement, 2) economic benefit, and 3) environmental impact mitigation. The proposed optimization problem is solved using multi-objective optimization. This allows the solution to this problem to entail the best trade-off between these possibly conflicting objectives and enables the selection of the optimal design under each objective's consideration i.e., through the Pareto set. In this work, each objective detailed described in the following subsections.

a: RESILIENCE INDEX

The resilience index is responsible for ensuring the system's capacity to withstand HILP events. For this, the system's loss performance considering the duration of degradation and the importance of rapid recovery has been used [3]. The resilience index considering Phase I and II can be expressed using (14a).

$$RESI = \frac{1}{t^r - t^e}\int_{t^e}^{t^r}\left[\frac{SPF_0\,(t) - SPF\,(t)}{SPF\,(t)}\right]dt \tag{14a}$$

Then, by considering the set of scenarios s and season se according to Fig. 2, eq. (14a) can be re-formulated into (14b)-(14c). This perspective allows for combining the multiple inner level season and scenarios information, i.e., $\forall s \in \Omega''_s$ and $\forall se \in \Omega_{se}$, in a way to determine a single value for the outer level resilience index.

$$RESI_{s,se} = \frac{1}{t^r_{s,se} - t^e_{s,se}}\int_{t^e_{s,se}}^{t^r_{s,se}} \times \left(\frac{\sum_{i\in\Omega_{BUS}} P^L_{i,t,s,se} - \sum_{i\in\Omega_{BUS}}(1 - b^{curt}_{i,t,s,se})P^L_{i,t,s,se}}{\sum_{i\in\Omega_{BUS}} P^L_{i,t,s,se}}\right)dt, \quad \forall s \in \Omega''_s, \quad \forall se \in \Omega_{se} \tag{14b}$$

$$RESI^{OLEV} = \sum\nolimits_{s\in\Omega_{se}} \frac{1}{N''_s}\sum\nolimits_{s\in\Omega''_s} RESI_{s,se} \tag{14c}$$

where, $t^e_{s,se}$ and $t^r_{s,se}$ corresponding to the beginning and end of the event for s^{th} scenario of season se. Next, $b^{curt}_{i,t,s,se}$ denote binary variable for load curtailment (i.e., 1: load shaded and 0: load fed) for bus i at time t for s^{th} scenario of season se. N''_s is the number of severe scenarios.

b: ECONOMIC INDEX

The second objective function relates to the economic benefit, i.e., capital cost, installation cost, and operation and maintenance (O&M) cost for ISWs [31] and DERs [32], [33], [34]. Where, eq. (15) defines the total cost as the second objective function for the outer level. Eqs. (16a)-(16c) determine the capital and O&M cost for the DDG, while (16d) normalizes the cost (16a) and (16c) for DDG units by considering the planning lifetime TL. Similarly, eqs. (17a)-(18c) summarize the capital and O&M cost for the allocated WTs and PVs. In term of the ES, (19a) and (19b) determine the capital cost depending to ES power and energy density, respectively. The annual O&M cost and the installation cost for the ES can be calculated using (19c) and (19d), respectively. In (19e) the normalized cost for ES considering TL is expressed. Finally, the cost for ISWs can be determined using (20a)-(20c).

$$TC^{OLEV} = \begin{pmatrix} C^{DDG} + C^{PV} \\ +C^{WT} + C^{ES} + C^{ISW} \end{pmatrix} \tag{15}$$

$$CPC^{DDG} = \sum\nolimits_{\forall i \in \Omega^{can}_{DDG}} \left(P^{DDG,size}_{i} \sigma^{DDG}_{INV} \right) \tag{16a}$$

$$OMC^{DDG}_{s,se} = S_{base} \begin{pmatrix} \sigma^{fuel} / \eta^{DDG} \\ +\sigma^{DDG}_{O\&M} \end{pmatrix} \sum\nolimits_{\forall i \in \Omega^{can}_{DDG}} \sum\nolimits_{\forall t \in \Omega_T} \times P^{DDG}_{i,t,s,se}, \quad \forall s \in \Omega'_s, \ \forall se \in \Omega_{se} \tag{16b}$$

$$AOMC^{DDG} = \frac{365}{4} \sum\nolimits_{\forall se \in \Omega_{se}} \sum\nolimits_{\forall s \in \Omega'_s} \left(\pi^{wiso}_{s,se} OMC^{DDG}_{s,se} \right) \tag{16c}$$

$$C^{DDG} = CPC^{DDG} + TL \times AOMC^{DDG} \tag{16d}$$

$$CPC^{PV} = \sum\nolimits_{\forall i \in \Omega^{can}_{PV}} \left(P^{PV,size}_{i} \sigma^{PV}_{INV} \right) \tag{17a}$$

$$AOMC^{PV} = \sum\nolimits_{\forall i \in \Omega^{can}_{PV}} \left(P^{PV,size}_{i} \sigma^{PV}_{O\&M} \right) \tag{17b}$$

$$C^{PV} = CPC^{PV} + TL \times AOMC^{PV} \tag{17c}$$

$$CPC^{WT} = \sum\nolimits_{\forall i \in \Omega^{can}_{WT}} \left(P^{WT,size}_{i} \sigma^{WT}_{INV} \right) \tag{18a}$$

$$AOMC^{WT} = \sum\nolimits_{\forall i \in \Omega^{can}_{WT}} \left(P^{WT,size}_{i} \sigma^{WT}_{O\&M} \right) \tag{18b}$$

$$C^{WT} = CPC^{WT} + TL \times AOMC^{WT} \tag{18c}$$

$$CPC^{ES,P} = \sum\nolimits_{\forall i \in \Omega^{can}_{ES}} \left(P^{ES,size}_{i} \sigma^{ES,P}_{INV} \right) \tag{19a}$$

$$CPC^{ES,E} = \sum\nolimits_{\forall i \in \Omega^{can}_{ES}} \left(E^{ES,size}_{i} \sigma^{ES,E}_{INV} \right) \tag{19b}$$

$$AOMC^{ES} = \sum\nolimits_{\forall i \in \Omega^{can}_{ES}} \left(P^{ES,size}_{i} \sigma^{ES}_{O\&M} \right) \tag{19c}$$

$$INSC^{ES} = \sum\nolimits_{\forall i \in \Omega^{can}_{ES}} \left(E^{ES,size}_{i} \sigma^{ES}_{INS} \right) \tag{19d}$$

$$C^{ES} = \begin{pmatrix} CPC^{ES,P} + TL \times AOMC^{ES} \\ +CPC^{ES,E} + INSC^{ES} \end{pmatrix} \tag{19e}$$

$$CPC^{ISW} = \sum\nolimits_{\forall i \in \Omega^{can}_{ISW}} (b^{ISW}_{i} \sigma^{ISW}_{INV}) \tag{20a}$$

$$AOMC^{ISW} = 8760 \sum\nolimits_{\forall i \in \Omega^{can}_{ISW}} (b^{ISW}_{i} \sigma^{ISW}_{O\&M}) \tag{20b}$$

$$C^{ISW} = CPC^{ISW} + TL \times AOMC^{ISW} \tag{20c}$$

where, for (16a)-(16c) $P^{DDG}_{i,t,s,se}$ is a variable denotes an active power generated by DDG i at time t for s^{th} scenario of season se. Then, $P^{DDG,size}_{i}$ denotes an active power rating of DDG at candidate bus i. σ^{DDG}_{INV}, $\sigma^{DDG}_{O\&M}$ and σ^{fuel} are the DDG's investment cost in \$/kW, O&M cost in \$/kWh and fuel cost in \$/kWh, respectively. η^{DDG} denotes a power efficiency of the DDG unit. S_{base} is the setting power base value. $\pi^{wiso}_{s,se}$ is a probability for both wind and solar scenario for s^{th} scenario of season se obtained by forward reduction technique. Ω^{can}_{DDG} is the set of candidate buses for DDG units. In term of (17a)-(18c), σ^{PV}_{INV} and σ^{WT}_{INV} denotes the investment cost in \$/kW for PV and WT, respectively. Then, $\sigma^{PV}_{O\&M}$ and $\sigma^{WT}_{O\&M}$ denotes the O&M cost in \$/kWh/year for the PV and WT. Then, for the energy storage unit in (19a)-(19d), $P^{ES,size}_{i}$ and $E^{ES,size}_{i}$ denotes active power rating and energy rationg of the ES at the candidate bus i, respectively. Then, $\sigma^{ES,P}_{INV}$ and $\sigma^{ES,E}_{INV}$ are the investment cost in \$/kWh for energy density rating and power rating of the ES unit, respectively. While, $\sigma^{ES}_{O\&M}$ and σ^{ES}_{INS} are the O&M cost in \$/kWh/year and installation cost in \$/kWh for ES, respectively. At the end, Ω^{can}_{ES} is the set of candidate buses for ES units. Finally, for (20a) and (20b), b^{ISW}_{i} is the binary decision variable for ISW allocation at candidate branch i. σ^{ISW}_{INV} and $\sigma^{ISW}_{O\&M}$ are investment cost in \$ per allocated ISW and it O&M cost in \$/year, respectively. Ω^{can}_{ISW} is the set of candidate branches for SSWs.

c: ENVIRONMENTAL IMPACT INDEX

The environment impact index aims to reduce the carbon footprint due to energy purchases from the main grid and energy generated by DDG [34], [35]. The annual carbon emission can be calculated using the expressions below. Eqs. (21a) and (21b) are the CO_2 emission quantity and their annualized kg/year from the DDGs generation. Eqs. (21c) and (21d) represent the CO_2 emission depending on the power imported from the main grid. Finally, (22) defines the total annualized Carbon emission as the third objective function for the outer level.

$$EMIS^{DDG}_{s,se} = K^{DDG}_{CO2} S_{base} \sum\nolimits_{\forall i \in \Omega_{DDG}} \sum\nolimits_{\forall t \in \Omega_T} P^{DDG}_{i,t,s,se}, \quad \forall s \in \Omega'_s, \quad \forall se \in \Omega_{se} \tag{21a}$$

$$AEMIS^{DDG} = \frac{365}{4} \sum\nolimits_{\forall se \in \Omega_{se}} \sum\nolimits_{\forall s \in \Omega'_s} \left(\pi^{wiso}_{s,se} EMIS^{DDG}_{s,se} \right) \tag{21b}$$

$$EMIS^{GRID}_{s,se} = K^{GRID}_{CO2} S_{base} \sum\nolimits_{\forall t \in \Omega_T} P^{GRID+}_{t,s,se}, \quad \forall s \in \Omega'_s, \ \forall se \in \Omega_{se} \tag{21c}$$

$$AEMIS^{GRID} = \frac{365}{4} \sum\nolimits_{\forall se \in \Omega_{se}} \sum\nolimits_{\forall s \in \Omega'_s} \left(\pi^{wiso}_{s,se} EMIS^{GRID}_{s,se} \right) \tag{21d}$$

$$AEMIS^{OLEV} = AEMIS^{DDG} + AEMIS^{GRID} \tag{22}$$

where, K^{DDG}_{CO2} and K^{GRID}_{CO2} are the carbon emission factor in kg/kWh according to energy generated by DDGs and energy imported from the main grid, respectively. $P^{GRID+}_{t,s,se}$ denotes active power imported from the main grid across the i^{th} PCC of the MG at time t for s^{th} scenario of season se.

TABLE 1. Decision variables type and set belonging for the outer level problem.

Variables X^{OLEV}	type	Set $\forall i \in$
$b_i^{DDG,size}$	$\mathbb{Z}$	Ω_{DDG}^{can}
$b_i^{WT,size}$	$\mathbb{Z}$	Ω_{WT}^{can}
$b_i^{PV,size}$	$\mathbb{Z}$	Ω_{PV}^{can}
$b_i^{ES,size}$	$\mathbb{Z}$	Ω_{ES}^{can}
b_i^{ISW}	$\mathbb{Z}$	Ω_{ISW}^{can}

2) CONSTRAINTS AND DECISION VARIABLES - OUTER LEVEL

Next, the system's constraints and decision variables for optimizing the outer level are following depicted.

a: DISCRETE SIZE FOR DERS CONSTRAINT:

The DERs size was discretized with a fixed step [35].

$$P_i^{DER,size} = b_i^{DER,size} P_{step}^{DER}, \quad \forall DER \in \{DDG, PV, WT, ES\}, \quad \forall i \in \Omega_{DER}^{can} \tag{23}$$

$$E_i^{ES,size} = r_i^{ES} \times P_i^{ES,size}, \quad \forall i \in \Omega_{ES}^{can} \tag{24}$$

where, $b_i^{DER,size}$ denotes the integer variable for DER allocation at candidate bus i. P_{step}^{DER} is the step size for DER allocation. Finally, r_i^{ES} is a ratio between the rated capacity and rated power for the ES.

b: MAXIMUM BUS POWER ALLOWABLE CONSTRAINT

The DER(s) connected to an individual bus must respect the technical constraints defined by (25) [35]:

$$\sum\nolimits_{\forall DER \in \{DDG,PV,WT,ES\}} P_i^{DER,size} \leq \overline{P}_i^{bus}, \quad \forall i \in \Omega_{BUS} \tag{25}$$

where, $\overline{P}_i^{bus}$ is a maximum installation power allowable for DERs at candidate bus i.

c: INSTALLATION DISCRETE BINARY CONSTRAINTS

$$0 \leq b_i^{DER,size} \leq \overline{P}^{DER}/P_{step}^{DER}, \quad \forall DER \in \{DDG, PV, WT, ES\}, \ \forall i \in \Omega_{DER}^{can} \tag{26}$$

$$0 \leq b_i^{ISW} \leq 1, \quad \forall i \in \Omega_{ISW}^{can} \tag{27}$$

where, $\overline{P}^{DER}$ denotes a planning upper bound for DER allocation in the system. b_i^{ISW} is a binary decision variable for ISW allocation at candidate branch i.

3) DECISION VARIABLES FOR OUTER LEVEL

The decision variables for optimizing the outer level are summarized in Table 1. Here one should note that variables associated with each planning element are respectively set to zero for the case that the optimization decides to not place these elements on the candidate buses or branches. Otherwise, these variables are the integer numbers respecting the upper bounds defined in (26)-(27), and the binary value '1' for b_i^{ISW}.

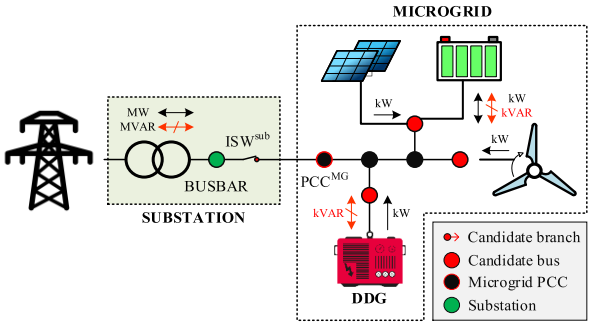

FIGURE 4. Basic scheme of the single microgrid base ISW^{sub}.

B. INNER LEVEL: OPTIMAL POWER FLOW FOR MICROGRIDS

This level presents the problem to be solved using the proposed machine learning based technique. Still, first, a pre-problem formulated as a Mixed Integer Linear Programming (MILP) model similar to the work in [19] is developed. This inner level optimization solutions provide the sample solutions needed to train the proposed machine learning-based strategy using the upper level solutions as inputs. For this, this problem models the ability of microgrids to operate in both GC and IS mode, depending on the operation status of the ISW^{sub} as shown in Fig. 4. Details on the problem formulation and optimization strategy including objective function, constraints and decision variables are following depicted.

1) OBJECTIVE FUNCTION AND CONSTRAINTS INNER LEVEL

The objective function formulated for the optimal operation in the inner level is expressed by (28a)-(28e). First, in (28a) the objective function is obtained by normalizing the four terms as a single total operation cost to be minimized. The first term in (28a) represents the cost of power exchange between the microgrid and the main grid, which can be determined using (28b). Then, the second term is given by (28c), which refers to the fuel consumption cost for the DDG units in use at the MGs [36], [34]. As one may observe, (28a), (28b) and (28c) are restricted to the GC mode due to the association of the binary input $b_{t,s,se}^{m}$, i.e., $b_{t,s,se}^{m}$ is the binary number that denotes the operation status for ISW^{sub} along Ω_T, where $b_{t,s,se}^{m} = 1$ represents the microgrid operation in islanding mode, otherwise $b_{t,s,se}^{m} = 0$ denotes the system operation in GC mode. In this sense, $b_{t,s,se}^{m}$ can be used as multiplication and integrated in the MILP model for allowing the objective function and constraints pertaining to the operation mode for microgrid. The third term given by (28d) represents the cost for load curtailment, being restricted to IS mode only [37]. The last term depicted in (28e) represents the voltage violation index. This term seeks to improve the voltage quality of the microgrid during both operation modes. For this, the following assumptions are made: 1) during GC mode, the DDG units are operated in active and reactive power control (PQ) mode [38], [39], 2) during IS mode the DDG units are operated under a secondary control layer with V^{**} identically

set for all DDG units.

$$OF_{s,se}^{MILP} = \sum_{t\in\Omega_T}\begin{bmatrix} C_{t,s,se}^{PCC}\left(1-b_{t,s,se}^{m}\right) \\ +C_{t,s,se}^{DDG}\left(1-b_{t,s,se}^{m}\right) \\ +C_{t,s,se}^{CURT}b_{t,s,se}^{m}+C_{t,s,se}^{VI}\end{bmatrix}, \quad \forall s\in\Omega_s'\cup\Omega_s'', \ \forall se\in\Omega_{se} \tag{28a}$$

$$C_{t,s,se}^{PCC} = S_{base}\left(\sigma_{t,s,se}^{PCC}P_{i=1,t,s,se}^{PCC}\right)\Delta t, \quad \forall t\in\Omega_T,\ \forall s\in\Omega_s'\cup\Omega_s'', \ \forall se\in\Omega_{se} \tag{28b}$$

$$C_{t,s,se}^{DDG} = S_{base}\left(\sum_{i\in\Omega_{DDG}}P_{i,t,s,se}^{DDG}\left(\sigma^{fuel}\Big/\eta^{DDG}+\sigma_{O\&M}^{DDG}\right)\right)\Delta t, \quad \forall t\in\Omega_T,\ \forall s\in\Omega_s'\cup\Omega_s'',\ \forall se\in\Omega_{se} \tag{28c}$$

$$C_{t,s,se}^{CURT} = S_{base}\left(\sigma^{curt}\sum_{i\in\Omega_{BUS}}b_{i,t,s,se}^{curt}w_i^{load}P_{i,t,s,se}^{L}\right)\Delta t, \quad \forall t\in\Omega_T,\ \forall s\in\Omega_s'\cup\Omega_s',\ \forall se\in\Omega_{se} \tag{28d}$$

$$C_{t,s,se}^{VI} = V_{base}\left(PC^{VI}\left[\sum_{i\in\Omega_{BUS}}\begin{pmatrix}\left(1-b_{t,s,se}^{m}\right)V_{GC}^{spec} \\ +b_{t,s,se}^{m}V_i^{**}-V_{i,t,s,se}\end{pmatrix}\right]\right)\Delta t, \quad \forall t\in\Omega_T,\ \forall s\in\Omega_s'\cup\Omega_s'',\ \forall se\in\Omega_{se} \tag{28e}$$

Subject to:

$$\underline{V}\le V_{i,t,s,se}\le\overline{V}, \quad \forall i\in\Omega_{BUS},\ \forall t\in\Omega_T, \ \forall s\in\Omega_s'\cup\Omega_s'', \quad \forall se\in\Omega_{se} \tag{29}$$

$$0\le b_{i,t,s,se}^{curt}\le b_{t,s,se}^{m}, \quad \forall i\in\Omega_{BUS},\ \forall t\in\Omega_T, \ \forall s\in\Omega_s'\cup\Omega_s'', \quad \forall se\in\Omega_{se} \tag{30}$$

$$P_{i,t,s,se} = \begin{pmatrix}\sum_{j\in\Omega_{BUS}}G_{ij}V_{i,t,s,se} \\ -\sum_{j\in\Omega_{BUS}}B_{ij}\delta_{j,t,s,se}\end{pmatrix} = \begin{pmatrix}P_{i,t,s,se}^{PCC}+P_{i,t,s,se}^{DDG} \\ +P_{i,t,s,se}^{WT,use}+P_{i,t,s,se}^{PV,use} \\ +P_{i,t,s,se}^{dch}-\eta_i^{ES}P_{i,t,s,se}^{ch} \\ -P_{i,t,s,se}^{L}\left(1-b_{i,t,s,se}^{curt}\right)\end{pmatrix}, \quad \forall i\in\Omega_{BUS}, \quad \forall t\in\Omega_T,\ \forall s\in\Omega_s'\cup\Omega_s'', \ \forall se\in\Omega_{se} \tag{31}$$

$$Q_{i,t,s,se} = \begin{pmatrix}-\sum_{j\in\Omega_{BUS}}B_{ij}V_{i,t,s,se} \\ -\sum_{j\in\Omega_{BUS}}G_{ij}\delta_{j,t,s,se}\end{pmatrix} = \begin{pmatrix}+Q_{i,t,s,se}^{PCC}+Q_{i,t,s,se}^{DDG} \\ +Q_{i,t,s,se}^{ES} \\ -Q_{i,t,s,se}^{L}\left(1-b_{i,t,s,se}^{curt}\right)\end{pmatrix}, \quad \forall i\in\Omega_{BUS}, \quad \forall t\in\Omega_T,\ \forall s\in\Omega_s'\cup\Omega_s'', \ \forall se\in\Omega_{se} \tag{32}$$

$$P_{k,t,s,se}^{br} = g_{i(k)j(k)}\left(V_{i,t,s,se}-V_{j,t,s,se}\right) + b_{i(k)j(k)}(\delta_{i,t,s,se}-\delta_{j,t,s,se}), \quad \forall k\in\Omega_{LIN}, \quad \forall t\in\Omega_T,\ \forall s\in\Omega_s'\cup\Omega_s'', \ \forall se\in\Omega_{se} \tag{33}$$

$$Q_{k,t,s,se}^{br} = \begin{pmatrix}b_{i(k)j(k)}\left(V_{i,t,s,se}-V_{j,t,s,se}\right) \\ +g_{i(k)j(k)}\left(\delta_{i,t,s,se}-\delta_{j,t,s,se}\right)\end{pmatrix}, \quad \forall k\in\Omega_{LIN}, \quad \forall t\in\Omega_T,\ \forall s\in\Omega_s'\cup\Omega_s'', \ \forall se\in\Omega_{se} \tag{34}$$

$$L_{k,t,s,se}^{br} = \begin{cases}\alpha_n^{1^{st}}P_{k,t,s,se}^{br}+\beta_n^{1^{st}}Q_{k,t,s,se}^{br} \\ -\gamma^{1^{st}}\overline{I}_k^{br}V_{i(k),t,s,se}\le 0 \\ -\alpha_n^{1^{st}}P_{k,t,s,se}^{br}+\beta_n^{1^{st}}Q_{k,t,s,se}^{br} \\ -\gamma^{1^{st}}\overline{I}_k^{br}V_{i(k),t,s,se}\le 0 \\ -\alpha_n^{4^{th}}P_{k,t,s,se}^{br}-\beta_n^{4^{th}}Q_{k,t,s,se}^{br} \\ -\gamma^{4^{th}}\overline{I}_k^{br}V_{i(k),t,s,se}\le 0 \\ \alpha_n^{4^{th}}P_{k,t,s,se}^{br}-\beta_n^{4^{th}}Q_{k,t,s,se}^{br} \\ -\gamma^{4^{th}}\overline{I}_k^{br}V_{i(k),t,s,se}\le 0,\end{cases} \quad n=1,2,\ldots,n_{pw}, \quad \forall t\in\Omega_T,\ \forall k\in\Omega_{LIN}, \ \forall i\in\Omega_{BUS}, \quad \forall s\in\Omega_s'\cup\Omega_s'',\ \forall se\in\Omega_{se} \tag{35}$$

$$P_{i,t,s,se}^{DDG} = \begin{pmatrix}\left[-k^{i\omega}\left(\delta_{t,s,se}^{MG}-\pi/2\right)\Big/m_i^p\right]b_{t,s,se}^{m} \\ +\left(1-b_{t,s,se}^{m}\right)P_{i,t,s,se}^{DDG}\end{pmatrix}, \quad \forall i\in\Omega_{DDG}, \quad \forall t\in\Omega_T,\ \forall s\in\Omega_s'\cup\Omega_s'', \ \forall se\in\Omega_{se} \tag{36}$$

$$Q_{i,t,s,se}^{DDG} = \begin{pmatrix}\left[\left(V_i^{*}-V_{i,t,s,se}+u_{i,t,s,se}^{v}\right)\Big/n_i^q\right]b_{t,s,se}^{m} \\ +\left(1-b_{t,s,se}^{m}\right)Q_{i,t,s,se}^{DDG}\end{pmatrix}, \quad \forall i\in\Omega_{DDG}, \quad \forall t\in\Omega_T,\ \forall s\in\Omega_s'\cup\Omega_s'', \ \forall se\in\Omega_{se} \tag{37}$$

$$V_{i,t,s,se}b_{t,s,se}^{m} = V_i^{**}b_{t,s,se}^{m}, \quad \forall i\in\Omega_{DDG},\ \forall t\in\Omega_T, \ \forall s\in\Omega_s'\cup\Omega_s'',\ \forall se\in\Omega_{se} \tag{38}$$

$$\overline{S}_i^{DDG} = P_i^{DDG,size}, \quad \forall i\in\Omega_{DDG} \tag{39}$$

$$m_i^p = \Delta\omega\Big/\overline{S}_i^{DDG}, \quad \forall i\in\Omega_{DDG} \tag{40}$$

$$n_i^q = \Delta V\Big/2\overline{\chi}^{DDG}\overline{S}_i^{DDG}, \quad \forall i\in\Omega_{DDG} \tag{41}$$

$$0\le P_{i,t,s,se}^{DDG}\le\overline{S}_i^{DDG}, \quad \forall i\in\Omega_{DDG},\ \forall t\in\Omega_T, \ \forall s\in\Omega_s'\cup\Omega_s'', \quad \forall se\in\Omega_{se} \tag{42}$$

$$\underline{\chi}^{DDG}\overline{S}_i^{DDG}\le Q_{i,t,s,se}^{DDG}\le\overline{\chi}^{DDG}\overline{S}_i^{DDG}, \quad \forall i\in\Omega_{DDG}, \ \forall t\in\Omega_T, \quad \forall s\in\Omega_s'\cup\Omega_s'',\ \forall se\in\Omega_{se} \tag{43}$$

$$-P_{i,t,s,se}^{DDG}tg\left(\cos^{-1}PF_i^{DDG,4th}\right) \le Q_{i,t,s,se}^{DDG}\le P_{i,t,s,se}^{DDG}tg\left(\cos^{-1}PF_i^{DDG,1st}\right), \quad \forall i\in\Omega_{DDG}, \quad \forall t\in\Omega_T,\ \forall s\in\Omega_s'\cup\Omega_s'', \ \forall se\in\Omega_{se} \tag{44}$$

$$L_{i,t,s,se}^{DDG} = \begin{cases}\alpha_n^{1^{st}}P_{i,t,s,se}^{DDG}+\beta_n^{1^{st}}Q_{i,t,s,se}^{DDG} \\ -\gamma^{1^{st}}\overline{S}_i^{DDG}\le 0 \\ \alpha_n^{4^{th}}P_{i,t,s,se}^{DDG}-\beta_n^{4^{th}}Q_{i,t,s,se}^{DDG} \\ -\gamma^{4^{th}}\overline{S}_i^{DDG}\le 0,\end{cases} \quad n=1,2,\ldots,n_{pw}, \quad \forall t\in\Omega_T,\forall i\in\Omega_{DDG} \ \forall s\in\Omega_s'\cup\Omega_s'',\ \forall se\in\Omega_{se} \tag{45}$$

$$0 \le P^{WT,use}_{i,t,s,se} \le P^{WT}_{i,t,s,se}, \quad \forall i \in \Omega_{WT},\ \forall t \in \Omega_T, \quad \forall s \in \Omega'_s \cup \Omega''_s, \quad \forall se \in \Omega_{se} \tag{46}$$

$$0 \le P^{PV,use}_{i,t,s,se} \le P^{PV}_{i,t,s,se}, \quad \forall i \in \Omega_{PV},\ \forall t \in \Omega_T, \quad \forall s \in \Omega'_s \cup \Omega''_s, \quad \forall se \in \Omega_{se} \tag{47}$$

$$\overline{S}^{ES}_i = P^{ES,size}_i, \quad \forall i \in \Omega_{ES} \tag{48}$$

$$0 \le P^{dch}_{i,t,s,se} \le \overline{S}^{ES}_i b^{ES}_{i,t,s,se}, \quad \forall i \in \Omega_{ES}, \quad \forall t \in \Omega_T, \quad \forall s \in \Omega'_s \cup \Omega''_s, \quad \forall se \in \Omega_{se} \tag{49}$$

$$0 \le P^{ch}_{i,t,s,se} \le \overline{S}^{ES}_i \left(1 - b^{ES}_{i,t,s,se}\right), \quad \forall i \in \Omega_{ES}, \quad \forall t \in \Omega_T, \quad \forall s \in \Omega'_s \cup \Omega''_s, \ \forall se \in \Omega_{se} \tag{50}$$

$$\underline{\chi}^{ES}\overline{S}^{ES}_i \le Q^{ES}_{i,t,s,se} \le \overline{\chi}^{ES}\overline{S}^{ES}_i, \quad \forall i \in \Omega_{ES},\ \forall t \in \Omega_T, \quad \forall s \in \Omega'_s \cup \Omega''_s, \quad \forall se \in \Omega_{se} \tag{51}$$

$$L^{ES}_{i,t,s,se} = \begin{cases} \alpha^{1st}_n \left(P^{dch}_{i,t,s,se} - P^{ch}_{i,t,s,se}\right) + \beta^{1st}_n Q^{ES}_{i,t,s,se} - \gamma^{1st}\overline{S}^{ES}_i \le 0 \\ -\alpha^{1st}_n \left(P^{dch}_{i,t,s,se} - P^{ch}_{i,t,s,se}\right) + \beta^{1st}_n Q^{ES}_{i,t,s,se} - \gamma^{1st}\overline{S}^{ES}_i \le 0 \\ -\alpha^{4th}_n \left(P^{dch}_{i,t,s,se} - P^{ch}_{i,t,s,se}\right) - \beta^{4th}_n Q^{ES}_{i,t,s,se} - \gamma^{4th}\overline{S}^{ES}_i \le 0 \\ \alpha^{4th}_n \left(P^{dch}_{i,t,s,se} - P^{ch}_{i,t,s,se}\right) - \beta^{4th}_n Q^{ES}_{i,t,s,se} - \gamma^{4th}\overline{S}^{ES}_i \le 0, \end{cases}$$
$$n = 1, 2, \ldots, n_{pw}, \quad \forall t \in \Omega_T,\ \forall i \in \Omega_{ES}, \quad \forall s \in \Omega'_s \cup \Omega''_s, \quad \forall se \in \Omega_{se} \tag{52}$$

$$E^{ES}_{i,t,s,se} = \begin{cases} SOC^0_i E^{ES,size}_i + \left(\eta^{ES}_i P^{ch}_{i,t,s,se} - P^{dch}_{i,t,s,se}\right)\Delta t, \quad t = 1 \\ E^{ES}_{i,t-1,s,se} + \left(\eta^{ES}_i P^{ch}_{i,t,s,se} - P^{dch}_{i,t,s,se}\right)\Delta t, \quad t \ge 2, \end{cases}$$
$$\forall i \in \Omega_{ES}, \quad \forall t \in \Omega_T,\ \forall s \in \Omega'_s \cup \Omega''_s, \quad \forall se \in \Omega_{se} \tag{53}$$

$$DoD^{max} E^{ES,size}_i \le E^{ES}_{i,t,s,se} \le E^{ES,size}_i, \quad \forall i \in \Omega_{ES},\ \forall t \in \Omega_T, \quad \forall s \in \Omega'_s \cup \Omega''_s, \quad \forall se \in \Omega_{se} \tag{54}$$

$$E^{ES}_{i,t=N_T,s,se} \ge SOC^0_i E^{ES,size}_i, \quad \forall i \in \Omega_{ES},\ \forall s \in \Omega'_s \cup \Omega''_s, \quad \forall se \in \Omega_{se} \tag{55}$$

$$-\overline{S}^{TR}_i \left(1 - b^m_{t,s,se}\right) \le P^{PCC}_{i,t,s,se} \le \overline{S}^{TR}_i \left(1 - b^m_{t,s,se}\right), \quad \forall i \in \Omega_{PCC},\ \forall t \in \Omega_T, \quad \forall s \in \Omega'_s \cup \Omega''_s,\ \forall se \in \Omega_{se} \tag{56}$$

$$\underline{\chi}^{TR}\overline{S}^{TR}_i \left(1 - b^m_{t,s,se}\right) \le Q^{PCC}_{i,t,s,se} \le \overline{\chi}^{TR}\overline{S}^{TR}_i \left(1 - b^m_{t,s,se}\right), \quad \forall i \in \Omega_{PCC}, \quad \forall t \in \Omega_T, \quad \forall s \in \Omega'_s \cup \Omega''_s, \quad \forall se \in \Omega_{se} \tag{57}$$

$$L^{PCC}_{i,t,s,se} = \begin{cases} \alpha^{1st}_n P^{PCC}_{i,t,s,se} + \beta^{1st}_n Q^{PCC}_{i,t,s,se} - \gamma^{1st}\overline{S}^{TR}_i \le 0 \\ -\alpha^{1st}_n P^{PCC}_{i,t,s,se} + \beta^{1st}_n Q^{PCC}_{i,t,s,se} - \gamma^{1st}\overline{S}^{TR}_i \le 0 \\ -\alpha^{4th}_n P^{PCC}_{i,t,s,se} - \beta^{4th}_n Q^{PCC}_{i,t,s,se} - \gamma^{4th}\overline{S}^{TR}_i \le 0 \\ \alpha^{4th}_n P^{PCC}_{i,t,s,se} - \beta^{4th}_n Q^{PCC}_{i,t,s,se} - \gamma^{4th}\overline{S}^{TR}_i \le 0, \end{cases}$$
$$n = 1, 2, \ldots, n_{pw}, \quad \forall t \in \Omega_T,\ \forall i \in \Omega_{PCC}, \quad \forall s \in \Omega'_s \cup \Omega''_s, \quad \forall se \in \Omega_{se} \tag{58}$$

$$-P^{PCC}_{i,t,s,se} tg\left(\cos^{-1} PF^{TR,4th}_i\right) \le Q^{PCC}_{i,t,s,se} \le P^{PCC}_{i,t,s,se} tg\left(\cos^{-1} PF^{TR,1st}_i\right), \quad \forall i \in \Omega_{PCC}, \quad \forall t \in \Omega_T, \quad \forall s \in \Omega'_s \cup \Omega''_s, \quad \forall se \in \Omega_{se} \tag{59}$$

$$V_{i,t,s,se}\left(1 - b^m_{t,s,se}\right) = V^{GC}_{spec}\left(1 - b^m_{t,s,se}\right), \quad \forall i \in \Omega_{PCC}, \quad \forall t \in \Omega_T, \quad \forall s \in \Omega'_s \cup \Omega''_s, \quad \forall se \in \Omega_{se} \tag{60}$$

$$\delta_{i,t,s,se}\left(1 - b^m_{t,s,se}\right) = 0, \quad \forall i \in \Omega_{PCC},\ \forall t \in \Omega_T, \quad \forall s \in \Omega'_s \cup \Omega''_s, \quad \forall se \in \Omega_{se} \tag{61}$$

where, for the objective function $P^{PCC}_{i,t,s,se}$ denotes an active power imported/exported from/to the main grid across the i^{th} PCC of the MG at time t for s^{th} scenario of season se. $\sigma^{PCC}_{t,s,se}$ is the market energy price in \$/kWh corresponding to time t for s^{th} scenario of season se. While σ^{curt} is cost of load curtailment in \$/kWh. $b^{curt}_{i,t,s,se}$ denote a binary variable for load curtailment (1: load shaded and 0: load fed) for bus i at time t for s^{th} scenario of season se. w^{load}_i is the weighing coefficient of load at bus i. V_{base} is a setting voltage magnitude base value. PC^{VI} denotes a penalty coefficient of voltage violation in \$/kV. V^{spec}_{GC} is a nominal specified voltage during GC mode. V^{**}_i denote a voltage reference for secondary control of the DDG at candidate bus i operated with droop/2$^{\text{nd}}$. $V_{i,t,s,se}$ denotes a voltage magnitude of the bus i at time t for s^{th} scenario of season se.

In term it constraints, first for (29)-(35) $\underline{V}$ and $\overline{V}$ are maximum/Minimum voltage violation of the bus. $P_{i,t,s,se}$ and $Q_{i,t,s,se}$ denotes the active and reactive power injected to bus i at time t for s^{th} scenario of season se. G_{ij} and B_{ij} are the element of the conductance and susceptance matrix denotes the connection of bus i to bus j, respectively. $P^{WT,use}_{i,t,s,se}$ and $P^{PV,use}_{i,t,s,se}$ are respectively the PV and WT's adjusting power output and used at time t for s^{th} scenario of season se. $P^{dch}_{i,t,s,se}$ and $P^{ch}_{i,t,s,se}$ denotes the active power charge and discharge by i^{th} ES unit at time t for s^{th} scenario of season se, respectively. η^{ES}_i is a efficiency of the energy storage. $\delta_{j,t,s,se}$ is the voltage magnitude angle of bus i at time t for s^{th} scenario of season se., $Q^{PCC}_{i,t,s,se}$ denotes a reactive power exchange with the main grid across the i^{th} PCC of the MG at time t for s^{th} scenario of season se. $Q^{DDG}_{i,t,s,se}$ is a reactive power generated by the i^{th} DDG unit at time t for s^{th} scenario of season se. $Q^{ES}_{i,t,s,se}$ is a reactive power generate/receive of the i^{th} ES unit, at time t for s^{th} scenario

of season se. $P^{br}_{k,t,s,se}$ and $Q^{br}_{k,t,s,se}$ are the active and reactive power flowing across the transmission branch k at time t for s^{th} scenario of season se. $g_{i(k)j(k)}$ and $b_{i(k)j(k)}$ denotes the conductance and susceptance between bus i to j of branch k. $L^{br}_{k,t,s,se}$ is a set of piecewise linearization for line ampacity quadratic constraint. $\overline{I}^{br}_{k}$ denotes a maximum ampacity of the branch k. For the DDG's constraints (36)-(45), $k^{i\omega}$ denotes an integral gain for frequency restoration for DDG with droop/2nd. $\delta^{MG}_{t,s,se}$ denotes a phase angle of the bus where the frequency control act at time t for s^{th} scenario of season se. m^{p}_{i} and n^{q}_{i} are the active and reactive droop gain of the i^{th} DDG unit with primary droop/2nd. V^{*}_{i} is a voltage reference for primary control of the DDG at candidate bus i operated with droop/2nd. $u^{v}_{i,t,s,se}$ is an integrator output of secondary voltage restoration of i^{th} DDG unit operating with droop/2nd at time t for s^{th} scenario of season se. $\overline{S}^{DDG}_{i}$ is a capacity rating of the DDG unit i.$\Delta\omega$ and ΔV are respectively a maximum angular frequency and voltage magnitude deviation. $\underline{\chi}^{DDG}$and $\overline{\chi}^{DDG}$ are the minimum/maximum ratio for determining lower/upper bound of DDG's reactive power. $PF^{DDG,1th}_{i}$ and $PF^{DDG,4st}_{i}$ denotes minimum operating power factor allowable of the 1st/4th quadrant of the DDG unit i. $L^{DDG}_{i,t,s,se}$ is a set of piecewise linearization for DDG quadratic constraint. For the ES's constrains (48)-(55), $\overline{S}^{ES}_{i}$ is maximum rating power of the ES unit i. $b^{ES}_{i,t,s,se}$ denotes a binary variable indicates the status of ES (i.e. 1: discharge and 0: charge). $\underline{\chi}^{ES}$ and $\overline{\chi}^{ES}$ are the minimum/maximum ratio for determining lower/upper bound of ES's reactive power. $L^{ES}_{i,t,s,se}$ is a set of piecewise linearization for ES quadratic constraint. $E^{ES}_{i,t,s,se}$ denotes an energy SOC of the ES unit i at time t for s^{th} scenario of season se. SOC^{0}_{i} is an initial state of charge of the ES unit. $DoD^{max}$is a maximum Depth of Discharge allowable for ES. Finally, for (56)-(59) $\overline{S}^{TR}_{i}$ is a capacity rate of the transformer. $\underline{\chi}^{TR}$ and $\overline{\chi}^{TR}$ are the minimum/maximum ratio for determining lower/upper bound of reactive power flowing across TR. $L^{PCC}_{i,t,s,se}$ is a set of piecewise linearization for PCC quadratic constraint., $PF^{TR,1st}_{i}$ and $PF^{TR,4th}_{i}$ are the minimum operating power factor allowable of the 1st/4th quadrant of the transformer i.

For these constaints, the inequality (29) represents the general constrain that guarantees the voltage magnitude for different individual buses within magnitude limits. Eq. (30) guarantees load curtailment during IS mode. The microgrid model is obtained using the power flow model given by (31)-(35). Constraints (31) and (32) are the linear version of the node-based power flow equation that refers to the power injected to thei^{th} bus of the microgrid [19]. It is worth noting here that, (31) and (32) have been generally formulated for all buses. Thus, the variables representing the power exchange and generation (i.e., by DDG, WT, PV, ES) that are not relevant to the power flow equations written for bus i can be disregarded by setting the upper bound for these variables to zeros. Next, eqs. (33) and (34) are the linear version defining the active and reactive power flowing along a branch k in the microgrid. Where, $i(k)$ and $j(k)$ denote buses i and j located at the upstream and downstream of branch k, respectively. Finally, (35) is the piecewise linearization of the quadratic constraint limiting the line ampacity.

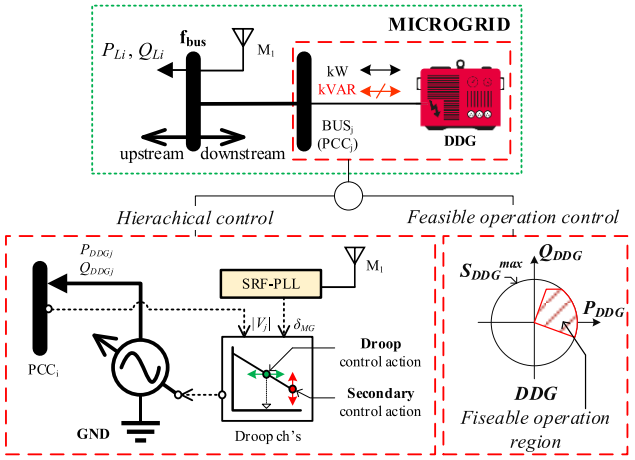

FIGURE 5. Steady state model for DDG unit operate with droop/2nd in IS mode and their feasible operation region for both GC and IS mode.

The DDG units are modeled using the steady state model (36)-(45). Fig. 5 shows the steady state model employed for representing operation constraints for the DDG units with droop/2nd. Details of the derivation of the DDG unit operation constraints can be found in [19]. Constraints (36) and (37) define the active and reactive power generated by the DDG units during IS or GC mode. These constraints are composed of two terms associated with the binary input $b^{m}_{t,s,se}$. The first term of these constraints refers to the operation of the DDG unit under droop/2nd control during IS mode. The second terms represent the operation of the DDG unit in PQ mode during GC mode. As one may observe, the activation of the terms in (36) and (37) are conditioned to the binary input $b^{m}_{t,s,se}$ status. Eq. (38) guarantees the voltage of the DDG bus restoration to the nominal secondary setting voltage in IS mode. Eq. (39) defines the apparent power equal to the DDG allocated unit rated size. In this work, loads are considering to be shared proportionally to the capacity of the DDG units [37], [39]. Thus, the active and reactive droop gain can be calculated via the capacity-based model as expressed in (40) and (41). Eqs. (42) and (43) establish minimum and maximum boundary limits to the active and reactive power.

Constraint (44) guarantees that the relationship between the active and reactive power of a DDG unit is greater than the minimum set power factor. Finally (45) represents the set of piecewise linearization that ensures the operation of the DDG unit respecting its rated capacity $\overline{S}^{DDG}_{i}$. Constraints (46) and (47) represent the power outputs of the WTs and PVs considering their actual MPPT power $P^{WT}_{i,t,s,se}$ and $P^{PV}_{i,t,s,se}$. ES constraints are depicted in (48)-(55). For this, in this work, ES units are operated in PQ mode via its power electronic inverter interfaced (48). Nevertheless, with the power electronic interface, the ES can be operated with droop/2nd

control similar to the work in [19]. Constraints (49)-(50) guarantee that the ES units' operations are restricted within the feasible operation region. In these constraints, the binary variable $b^{ES}_{i,t,s,se}$ is introduced in (49) and (50) to avoid simultaneous charging and discharging states. Eq. (51) ensures that the reactive power delivered by the ES units respect their maximum and minimum reactive power allowable setting. As the ES unit is connected through an inverter, (52) defines the piecewise linearization representing the quadratic constrain for limiting the output to the maximum rated power denote by $\overline{S}^{ES}_i$. In (53) update SOC for the ES are obtained for each time segment based on the charging/discharging energy flows, as well as considering the round-trip efficiency η^{ES}_i [32], [40]. Constraint (54) guarantees that the energy stored in the ES is restricted by its rated capacity and minimum energy storage setting. Finally (55) ensures that the energy stored in the ES is available at the end of the planning horizons and ready for the next days.

Constraints for the power exchange between the microgrid and the main grid at the substation are given by (56)-(61). The constraints (56)-(59) guarantee the power exchange is restricted by transformers' feasible operation. First, (56) and (57) limit the active and reactive power exchange respecting to the transformer rated power. As well, the introduction of $b^{m}_{t,s,se}$ in (56) and (57) allows for deactivating these constraints during IS mode. Then, (58) is the piecewise linearization representing the quadratic constrain for limiting the active and reactive power exchange under the transformer rated capacity. The operation for transformer limits above the minimum power factor setting is given by (59). Finally (60) and (61) refer to the grid connected power flow conditions for voltage magnitude and phase angle at the PCC^{MG} imposed by the main grid during GC mode.

The piecewise constraint coefficients for (35), (45), (52) and (58) can be calculated using (62a)-(62d). Details on the derivation of piecewise constrains coefficients for the quadratic constraints can be found in [19].

$$\alpha_n^{1^{st},4^{th}} = \cos\left(\varphi_n^{1^{st},4^{th}} + \left(n^{1^{st},4^{th}} - 1\right)\varphi_{sel}^{1^{st},4^{th}} \Big/ n_{pw}^{1^{st},4^{th}}\right), \quad n = 1, 2, \ldots, n_{pw} \tag{62a}$$

$$\beta_n^{1^{st},4^{th}} = \sin\left(\varphi_n^{1^{st},4^{th}} + \left(n^{1^{st},4^{th}} - 1\right)\varphi_{sel}^{1^{st},4^{th}} \Big/ n_{pw}^{1^{st},4^{th}}\right), \quad n = 1, 2, \ldots, n_{pw} \tag{62b}$$

$$\gamma^{1^{st},4^{th}} = \cos(\varphi_{sel}^{1^{st},4^{th}} \Big/ 2n_{pw}^{1^{st},4^{th}}), \quad n = 1, 2, \ldots, n_{pw} \tag{62c}$$

$$\varphi_0^{1^{st},4^{th}} = \varphi_{sel}^{1^{st},4^{th}} \Big/ 2n_{pw}^{1^{st},4^{th}}, \quad n = 1, 2, \ldots, n_{pw} \tag{62d}$$

2) DECISION VARIABLES - INNER LEVEL

The decision variables for the MILP model seeking to optimize microgrids' operation are summarized in Table 2.

TABLE 2. Decision variables for MILP model for microgrid optimal operation.

Variables		Set			
X^{MILP}	Type	$\forall t \in$	$,\forall s \in$	$\forall se \in$	$\forall i,k \in$
$V_{i,t,s,se}$	$\mathbb{R}$	Ω_T	$\Omega'_s \cup \Omega''_s$	Ω_{se}	Ω_{BUS}
$\delta_{i,t,s,se}$	$\mathbb{R}$	Ω_T	$\Omega'_s \cup \Omega''_s$	Ω_{se}	Ω_{BUS}
$b^{curt}_{i,t,s,se}$	$\mathbb{Z}$	Ω_T	$\Omega'_s \cup \Omega''_s$	Ω_{se}	Ω_{BUS}
$P^{DDG}_{i,t,s,se}$	$\mathbb{R}$	Ω_T	$\Omega'_s \cup \Omega''_s$	Ω_{se}	Ω_{DDG}
$Q^{DDG}_{i,t,s,se}$	$\mathbb{R}$	Ω_T	$\Omega'_s \cup \Omega''_s$	Ω_{se}	Ω_{DDG}
$u^{v}_{i,t,s,se}$	$\mathbb{R}$	Ω_T	$\Omega'_s \cup \Omega''_s$	Ω_{se}	Ω_{DDG}
$P^{WT,use}_{i,t,s,se}$	$\mathbb{R}$	Ω_T	$\Omega'_s \cup \Omega''_s$	Ω_{se}	Ω_{WT}
$P^{PV,use}_{i,t,s,se}$	$\mathbb{R}$	Ω_T	$\Omega'_s \cup \Omega''_s$	Ω_{se}	Ω_{PV}
$P^{dch}_{i,t,s,se}$	$\mathbb{R}$	Ω_T	$\Omega'_s \cup \Omega''_s$	Ω_{se}	Ω_{ES}
$P^{ch}_{i,t,s,se}$	$\mathbb{R}$	Ω_T	$\Omega'_s \cup \Omega''_s$	Ω_{se}	Ω_{ES}
$Q^{ES}_{i,t,s,se}$	$\mathbb{R}$	Ω_T	$\Omega'_s \cup \Omega''_s$	Ω_{se}	Ω_{ES}
$E^{ES}_{i,t,s,se}$	$\mathbb{R}$	Ω_T	$\Omega'_s \cup \Omega''_s$	Ω_{se}	Ω_{ES}
$b^{ES}_{i,t,s,se}$	$\mathbb{Z}$	Ω_T	$\Omega'_s \cup \Omega''_s$	Ω_{se}	Ω_{ES}
$P^{PCC}_{i,t,s,se}$	$\mathbb{R}$	Ω_T	$\Omega'_s \cup \Omega''_s$	Ω_{se}	Ω_{PCC}
$Q^{PCC}_{i,t,s,se}$	$\mathbb{R}$	Ω_T	$\Omega'_s \cup \Omega''_s$	Ω_{se}	Ω_{PCC}
$P^{br}_{k,t,s,se}$	$\mathbb{R}$	Ω_T	$\Omega'_s \cup \Omega''_s$	Ω_{se}	Ω_{LIN}
$Q^{br}_{k,t,s,se}$	$\mathbb{R}$	Ω_T	$\Omega'_s \cup \Omega''_s$	Ω_{se}	Ω_{LIN}

V. STAGE III: OPTIMAL OPERATION BASED ON DEEP NEURAL NETWORK (DNN) LEARNING

The detailed modeling of the multiple components involved in microgrids for ensuring adequate operating conditions during GC and IS modes, makes it unfeasible to solve this problem using a MILP formulation due to the stochastic nature of the problem, and consequently, the implied high computational burden. In this sense, seeking to overcome these limitations while not reducing the modeling complexity in order to ensure feasible resilient solutions, a novel methodology using DNN technique is proposed. For this, effective training samples for the DNN models are necessary. These samples are composed of 1) the set of input samples for combinations of switch allocation and resources; and 2) the set of targets for the LOPF dependent indices used for determining the multi-objective functions of the outer level. To obtain this data, the LOPF model depicted in the Section III is used considering microgrid formation indicators-based N-K contingencies level. Here, given that the LOPF is simulated for set of sample inputs belonging to Ω_s, Ω''_s and Ω_{se}, which are independent to each other, parallel computing can be employed as shown in Fig. 6. For this, any third-party solution based on well-knows multi-CPU cores or multi-GPU cores can be applied.

A general outline of this process based on the stochastic deep learning AC linear optimum power flow ($\text{DL-LOPF}^{\text{AC}}$) approach considering microgrids operation and control is presented in Fig. 6. Details for obtaining the set of input samples, as well as the targets provided by the LOPF model are described in the following section.

A. SET OF SAMPLE INPUTS AND TARGETS

The set of input samples is a combination of possible allocations for the DDGs, WTs, PVs, ESs and ISWs, where $\mathbf{IN}^{\mathbf{dnn}}$ denotes the matrix including a set of sample *sp* which belonging to a set of DNN training samples Ω_{SAM}, that can be expressed by (63a)-(63b).

$$\mathbf{IN}^{\mathbf{dnn}} = \left[\boldsymbol{IN}_1^{\boldsymbol{dnn}}; \boldsymbol{IN}_2^{\boldsymbol{dnn}}; \ldots; \boldsymbol{IN}_{sp}^{\boldsymbol{dnn}}\right], \quad sp \in \Omega_{SAM} \tag{63a}$$

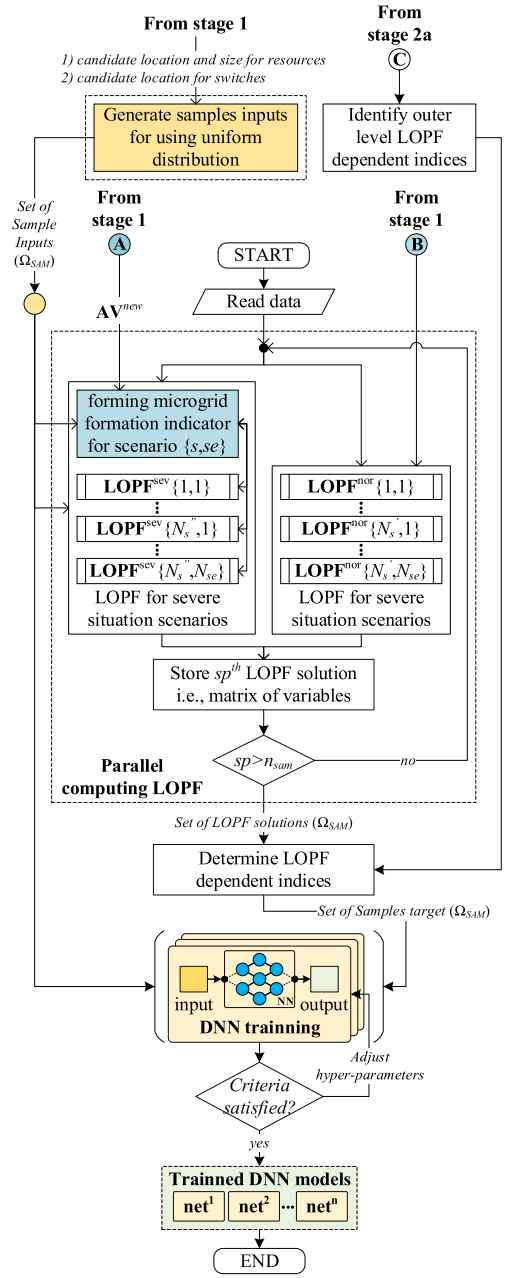

FIGURE 6. Proposed optimal operation for hierarchical microgrids based on deep-learning technique.

$$IN_{sp}^{dnn} = \begin{bmatrix} round\left(r_{a,sp}^{dnn}\right) \\ round\left(r_{b,sp}^{dnn}.\frac{\overline{P}^{DDG}}{P_{step}^{DDG}}\right)P_{step}^{DDG} \\ round\left(r_{c,sp}^{dnn}.\frac{\overline{P}^{WT}}{P_{step}^{WT}}\right)P_{step}^{WT} \\ round\left(r_{d,sp}^{dnn}.\frac{\overline{P}^{PV}}{P_{step}^{PV}}\right)P_{step}^{PV} \\ round\left(r_{e,sp}^{dnn}.\frac{\overline{P}^{ES}}{P_{step}^{ES}}\right)P_{step}^{ES} \end{bmatrix}, \quad \begin{matrix} sp \in \Omega_{SAM} \\ a \in \Omega_{ISW}^{can} \\ b \in \Omega_{DDG}^{can} \\ c \in \Omega_{WT}^{can} \\ d \in \Omega_{PV}^{can} \\ e \in \Omega_{ES}^{can} \end{matrix} \tag{63b}$$

The vector IN_{sp}^{dnn} is dependent on the candidate location of the ISW and resources, where n_{feat} denotes the number of features for a single DNN training sample input, in this case $n_{feat} = n_{ddg} + n_{wt} + n_{pv} + n_{es} + n_{isw}$, r_{sp}^{dnn} is a uniform random number between [0,1]. In this work, the uniform random is generated one time as a matrix with a size $n_{feat} \times n_{sam}$ representing a whole Ω_{SAM} training sample inputs before being classified into subset according to the candidate location of switch and resources as seen in (63b). In this way, it guarantees that the generated random numbers cover all possible configurations in the space $n_{feat} \times n_{sam}$.

The set of targets is identified by the outer level's indices dependent on the decision variables of the LOPF problem. In this case, from (14b)-(22) the identified indices are $RESI^{OLEV}$, $AOMC^{DDG}$, $AEMIS^{DDG}$ and $AEMIS^{GRID}$, where $TG_{sp,n}$ denotes the DNN targets n corresponding to LOPF solution sample sp, the identification targets for training the DNN model can be given by (64)-(66).

$$TG_{sp,1} = RESI^{OLEV}, \quad \forall sp \in \Omega_{SAM} \tag{64}$$

$$TG_{sp,2} = \begin{cases} AOMC^{DDG}/(\frac{365}{4}S_{base}\left(\sigma^{fuel}\Big/\eta^{DDG} + \sigma_{O\&M}^{DDG}\right)) \\ or \\ AEMIS^{DDG}/(\frac{365}{4}S_{base}K_{CO2}^{DDG}) \end{cases} = \sum_{\forall se \in \Omega_{se}}\sum_{\forall s \in \Omega_s}\left(\pi_{s,se}^{wiso}\sum_{\forall i \in \Omega_{DDG}}\sum_{\forall t \in \Omega_T}P_{i,t,s,se}^{DDG}\right), \quad \forall sp \in \Omega_{SAM} \tag{65}$$

$$TG_{sp,3} = AEMIS^{GRID}/(\frac{365}{4}S_{base}K_{CO2}^{GRID}) = \sum_{\forall se \in \Omega_{se}}\sum_{\forall s \in \Omega_s}\left(\pi_{s,se}^{wiso}\sum_{\forall i \in \Omega_{DDG}}\sum_{\forall t \in \Omega_T}P_{t,s,se}^{GRID+}\right), \quad \forall sp \in \Omega_{SAM} \tag{66}$$

The first target (64), $RESI^{OLEV}$, is dependent on LOPF's decision variable $b_{i,t,s,se}^{curt}$. It is responsible for the training of the DDN model for accounting $b_{i,t,s,se}^{curt}$ of the inner level. This allows the trained DNN model enables to predict the resilience index value which is corresponding to the first objective function as discussed in section IV. The second target (65) is related to $AOMC^{DDG}$ and $AEMIS^{DDG}$ indices dependent on the LOPF's decision variables $P_{i,t,s,se}^{DDG}$. It characterizes both indices shared by the same variable i.e., $P_{i,t,s,se}^{DDG}$ and leading to the possibility to predict only a single value for determining these two indices. As can see in (65), $TG_{sp,2}$ can be calculated via $AOMC^{DDG}$, or $AEMIS^{DDG}$, as those indices are dependent on the same $P_{i,t,s,se}^{DDG}$. In this case, the prediction results according to $TG_{sp,2}$ can be used for re-calculating $AOMC^{DDG}$ and $AEMIS^{DDG}$ respecting their corresponding multiplication constant requirement. These re-calculated provide the predicted results for $AOMC^{DDG}$ and $AEMIS^{DDG}$ which is necessary for determining the second/third objective function for the outer level (i.e., TC^{OLEV} and $AEMIS^{OLEV}$)

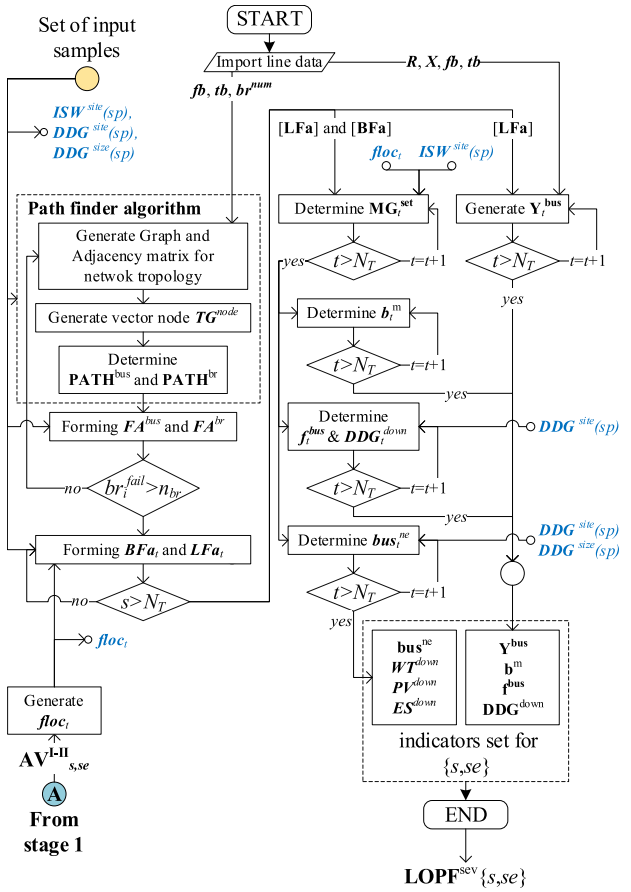

FIGURE 7. Flowchart for generating the microgrid indicator matrices and vectors for time $t \in \Omega_T$ for scenarios s of season se.

accordingly. Finally (66) corresponds to $AEMIS^{GRID}$ which is dependent to $P^{GRID+}_{i,t,s,se}$, leading to the representation of the predicted value of the trained DNN model for the annualized CO_2 emission by the power imported from the main grid during GC mode, similar to (21d) in section IV.

B. MICROGRID FORMATION

The microgrid formation is the intermediate step within the stochastic optimal operation level. This step delivers the necessary indicators for optimal operation level representing the microgrids formation due to N-K contingencies level. These indicators are the matrices and vectors that represent the time-coupling topologies of the test system during severe scenarios Ω''_s. The methodology for delivering the microgrid formation indicators respecting the LOPF problem is detailed illustrated in Fig. 7.

1) FAULT INFLUENCE PATH

First, the affected branch and bus pathfinder is proposed for searching the path(s) from the original fault location until the end branch (terminal edge) and end node (leaves node) respecting the graph representation of the network. This search algorithm is deployed in order to automatically search the path(s) whenever a single fault is located in the network. The respective step-by-step description of the algorithm solution is detailed in the following sections.

a: STEP 1: REPRESENTATION OF THE SYSTEM TOPOLOGY

Let the reference system topology be represented by the undirected graph $\mathbf{G^{bus}} = (\boldsymbol{ND^{bus}}, \boldsymbol{ED^{br}})$, where $\boldsymbol{ND^{bus}}$ are the set containing the vertices or nodes representing the buses in the reference system, while $\boldsymbol{ED^{br}}$ are the edge set representing the branch connected between two adjacent nodes in the test system. In this case, the adjacency matrix of $\mathbf{G^{bus}}$ is the $n_{bus} \times n_{bus}$ matrix denote by $\mathbf{M^{adj}} = [M^{adj}_{ij}]$ with M^{adj}_{ij} defined by (67) [41].

$$M^{adj}_{ij} = \begin{cases} 1, & \text{if } ND^{bus}_i ND^{bus}_j \in \boldsymbol{ED^{br}} \\ 0, & \text{otherwise} \end{cases} \tag{67}$$

As $\mathbf{G^{bus}}$ is an undirected graph, the adjacency matrix is the symmetrical square matrix with $M^{adj}_{ij} = M^{adj}_{ji}$. Here it is important to note that in case there is a reconfiguration in the reference system, $\mathbf{G^{bus}}$ and $\mathbf{M^{adj}}$ should be updated accordingly.

b: STEP 2: DETERMINATION OF THE TARGET NODES TG^{node}

Based on the graph $\mathbf{G^{bus}}$, the shortest path by Dijkstra's algorithm is adopted for determining the path(s), or road map(s), between the failed branch and the target node(s), where $fb\left(br^{fail}\right)$ denotes the start node for the shortest path, i.e. fault location, while the end of the shortest path is the target node including the root node and leave nodes. More detail about Dijkstra's algorithm can be found in [41], [42].

The target nodes can be identified using the adjacency matrix $\mathbf{M^{adj}}$, determining the row of $\mathbf{M^{adj}}$ with summation equal to one. In this sense, let i and j denote the row and column of $\mathbf{M^{adj}}$, $\sum_{j=1}^{n_{bus}} M^{adj}_{i,j} = 1$ indicates that node i is an end node with no connection elsewhere.

c: STEP 3: DETERMINATION OF THE PATH(S)

Once the target nodes are identified, Dijkstra's algorithm is employed for determining the shortest path between the start node $fb\left(br^{fail}\right)$ and the target nodes TG^{node}_i. For this, considering the system topology information available in the $\mathbf{G^{bus}}$ matrix, where the weight of all branches is set to one, given that any connection between two nodes is established by a unique path for a radial distribution system.

The Dijkstra's algorithm solution ($DIJK$) identifies the shortest path between two nodes, respectively $fb\left(br^{fail}\right)$ and TG^{node}_i, can be expressed by eq. (68).

$$\begin{aligned} \boldsymbol{path}^{\boldsymbol{bus}}_i &\left(fb\left(br^{fail}\right), TG^{node}_i\right) \\ &= DIJK\left(fb\left(br^{fail}\right), TG^{node}_i\right), \quad \forall i \in \Omega^{node}_{TG} \end{aligned} \tag{68}$$

Next, the branch path denoted by $path^{br}_i$ vector can be obtained by identifying the edges located within the solution path $fb\left(br^{fail}\right)$ to TG^{node}_i. Following, vectors $path^{bus}_i$ and $path^{br}_i$ belonging to a set of targets node(s) Ω^{node}_{TG} are

stored in matrices $\mathbf{PATH^{bus}}$ and $\mathbf{PATH^{br}}$, respectively. These matrices are responsible for determining the fault-influenced branch and bus matrices, being detailed elaborated on in the following section.

2) FAULT INFLUENCED BRANCH AND BUS MATRICES

Following, once affected paths are determined, clearing procedures must be established to successfully isolate the fault and ensure the system's resilience. In this sense, the representation of affected bus(es) and branch(es) by the respective fault(s) must be performed to enable planning algorithms solutions. These representations are respectively held by matrices **LFa** and **BFa**, describing affected bus(es) and branch(es). In addition, the establishment of rules to ensure the adequate allocation of candidate ISWs able to isolate the upstream and downstream of a branch fault is fundamental [43], [44]. For this, the following rules are established:

1) If the fault is found on the branch equipped with ISW, the fault stays in the middle of the branch and has been cleared by this ISW.
2) If the fault is located on the branch without ISW, the fault, in this case, is cleared by the nearby ISWs located along the searching paths.

A detailed description of bus and branch affected matrices is presented in the following sections.

a: BRANCH AFFECTED MATRIX (LFA)

The branch, or line, affected matrix **LFa** is the binary matrix assembling all binary vectors $\boldsymbol{LFa}_t$ with t belong to Ω_T, where an online branch is represented by "1", i.e., non-affected branch, and affected branches by the fault(s) are represented by "0". For determining this matrix, first, the binary matrix denoted by $\mathbf{FA^{br}}$ is required. $\mathbf{FA^{br}}$ is the binary square matrix $n_{br} \times n_{br}$, in which its i^{th} single row describes the set of affected branches corresponding to the location of a single fault br_i^{fail} where $i \in \Omega_{LIN}$. Once matrix $\mathbf{FA^{br}}$ is obtained, a generic i^{th} fault located at a branch "a", i.e., $floc_{i,t} = a$, due to the severe event at a time "t", allows for the determination of $\boldsymbol{LFa}_t$ by the row "a" of $\mathbf{FA^{br}}$. Moreover, $\mathbf{FA^{br}}$ is useful for manipulating the elements of $\boldsymbol{LFa_t}$ in case multiple faults are featured in the test system (i.e., $floc_{i,t} \in \Omega_{floc}$). To this end. the location of the fault(s) can be identified by looking up on time segment t of $\mathbf{AV}_{s,se}^{\mathbf{I-II}}$.

If there is more than a single fault located in the system. Let, $\boldsymbol{floc}_t$be a vector containing the locations of the faults, where its elements can be identified using $\mathbf{AV}_{s,se}^{\mathrm{I-II}}$. $\boldsymbol{LFa_t}$ at time t can be determined by looking up the multiple rows of $\mathbf{FA^{br}}$ considering the correspondent element number of vectors $\boldsymbol{floc}_t$ as described in (69), where $\prod$ denotes the Hadamard multiplication.

$$\boldsymbol{LFa}_t = \prod_{i \in \Omega_{floc}} \left[\circ \mathbf{FA^{br}}\left(floc_i, :\right) \right] \tag{69}$$

Finally, **LFa** is obtained by repeating the same methodology for $\boldsymbol{LFa}_t$ for $t \in \Omega_T$. Here one must note that, if no fault(s) occurs at time t, especially in the normal scenarios, i.e., Ω_s, the elements of $\boldsymbol{LFa}_t$ can be simply set by the vector constrained element of '1'.

TABLE 3. Algorithm for determining $FA^{bus}\{br_i^{fail}\}$.

Algorithm A: formation of $\boldsymbol{FA^{bus}}$

Initialize $\boldsymbol{FA^{bus}}(1{:}n_{bus}) = 1$
Generate $\mathbf{PATH^{br}}$ and $\mathbf{PATH^{bus}}$ using path finder for br_i^{fail}
for $pth = 1{:}n_{path}$
  Set $\boldsymbol{FA^{bus}}(br_i^{fail}, [\boldsymbol{fb}(br_i^{fail}), \boldsymbol{tb}(br_i^{fail})] = 0$
  for $br = 1{:}n_{path}$
    if $\mathbf{PATH^{br}}(pth, br)$ corresponding to location of ISW
      Denote $pis = \mathbf{PATH^{br}}(pth, br)$
      Find a_{fb} is an element address of $\mathbf{PATH^{br}}(pth, br) = \boldsymbol{fb}(pis)$
      Find a_{tb} is an element address of $\mathbf{PATH^{br}}(pth, br) = \boldsymbol{fb}(pis)$
      $\mathbf{FA^{bus}}\left(br^{fail}, \mathbf{PATH^{bus}}(pth, 1{:}min(a_{fb}, a_{tb}))\right) = 0$
      Break ***for*** *loop and go to next pth*
    elseif there is no ISW along path pth by $br = n_{path}$
      Find index for the non-zero number $\boldsymbol{nz}$ from $\mathbf{PATH^{bus}}(pth, :)$
      $\mathbf{FA^{bus}}\left(br^{fail}, \mathbf{PATH^{bus}}(pth, \boldsymbol{nz})\right) = 0$
      Break ***for*** *loop and go to next pth*
    end if of elseif
  end for
end for

b: BUS AFFECTED MATRIX (BFA)

Similar to the branches analysis, buses located within the fault zone bounded by the ISWs must be deactivated. In this sense, to represent this information, the binary matrix denoted by **BFa** containing the bus(es) affected is required, where the **BFa** is an assembly of the binary vectors $\boldsymbol{BFa}_t$ where $t \in \Omega_T$, with term(s) equal to "1", corresponding to an online bus, and "0" for those affected by the fault(s) and deactivated.

Following the binary matrix denoted by $\mathbf{FA^{bus}}$ is required. $\mathbf{FA^{bus}}$ is a non-square matrix due to $n_{bus} = n_{br} + 1$, where the i^{th} single row of $\mathbf{FA^{bus}}$ describes the set of affected buses corresponding to the location of a single fault location br_i^{fail} given $i \in \Omega_{LIN}$. Once this matrix $\mathbf{FA^{bus}}$ obtained, the $\boldsymbol{BFa}_t$ can be determined by looking up to the row "a" of $\mathbf{FA^{bus}}$. Similar to $\mathbf{FA^{br}}$, $\mathbf{FA^{bus}}$ can be used for determining $\boldsymbol{BFa}_t$ in case the case there is a multi-fault in the network i.e., $floc_{i,t} \in \Omega_{floc}$.

For determining $\mathbf{FA^{bus}}$, first $\mathbf{PATH^{br}}$ and $\mathbf{PATH^{bus}}$ have been determined for $br_i^{fail} \in \Omega_{LIN}$. Then, $\boldsymbol{FA^{bus}} br_i^{fail}$ is obtained searching $\mathbf{PATH^{br}} br_i^{fail}$ and $\mathbf{PATH^{br}} br_i^{fail}$ using the proposed algorithm described in Table 3.

For the case with multiple faults, a Hadamard multiplication $\prod$ is used according to $\mathbf{FA^{bus}}\{\boldsymbol{floc}_t\}$. Eq. (70) shows the formulation for determining $\boldsymbol{BFa}_t$ based on $\boldsymbol{floc}_t$.

$$\boldsymbol{BFa}_t = \prod_{i \in \Omega_{floc}} \left[\circ \mathbf{FA^{bus}}\left(floc_i, :\right) \right] \tag{70}$$

Similarly, $\boldsymbol{BFa}_t$ is repeatedly determined for $t \in \Omega_T$ and then stored in **BFa**. For the case where there is no fault at time t, the methodology described above can be skipped and $\boldsymbol{BFa}_t$ can be simply a set vector containing the element '1'.

TABLE 4. Formation of matrix containing microgrid set.

Algorithm: formation of $\mathbf{MG}_t^{\mathbf{set}}$

Initialize the matrix $\mathbf{MG}_t^{\mathbf{set}}(1{:}n_{bus}, 1{:}n_{bus}) = 0$
Determine $\boldsymbol{floc}_t = find\left(\mathbf{AV}_{s,se}^{\mathbf{I-II}}(1{:}n_{bus}, t) = 0\right)$
if $\boldsymbol{floc}_t$ is empty
    Set the matrix $\mathbf{MG}_t^{\mathbf{set}}(1{:}n_{bus}, 1{:}n_{bus}) = 0$
else
    import $\boldsymbol{LFa}_t$ from **LFa**, then $\boldsymbol{BFa}_t$ from **BFa**
    Initialized the root of microgrid $root^{MG} = 0$
    Set and initialize $\mathbf{MG}^{\mathbf{set0}} = 0$
    Initialize the status of the n^{th} ISW by $st_n^{isw} = 0$
➔ Find st_n^{isw} of the set $\boldsymbol{ISW}^{site}$ for time t
    for $n = 1{:}n_{isw}$
        if $\boldsymbol{LFa}_t(\boldsymbol{ISW}_n^{site}) = 0$,
            The $\boldsymbol{ISW}_n^{site}$ is open and set $st_n^{isw} = 0$
        else
            The $\boldsymbol{ISW}_n^{site}$ is still close and set $st_n^{isw} = 1$
        end if
    end for
    Define $\boldsymbol{ISW}^{open} = \boldsymbol{ISW}^{site}\left(find(st_n^{isw} = 0)\right)$
➔ Determine the adjacent matrix for $\mathbf{MG}_t^{\mathbf{set}}$
    Generate adjacency matrix $\mathbf{A}^{\mathbf{MG}}$ for the initial test system using (67)
    for $n = 1{:}n_{isw}^{open}$
        Set $\mathbf{A}^{\mathbf{MG}}\left(\boldsymbol{fb}(ISW_n^{open}), \boldsymbol{tb}(ISW_n^{open})\right) = 0$
        Set $\mathbf{A}^{\mathbf{MG}}\left(\boldsymbol{tb}(ISW_n^{open}), \boldsymbol{fb}(ISW_n^{open})\right) = 0$
    end for
➔ Determine the root of the microgrid(s) set
    Determine $\boldsymbol{bus}^{\boldsymbol{on}}$, by $\boldsymbol{bus}^{\boldsymbol{on}} = find(\boldsymbol{BFa}_t = 1)$
    for $m = 1{:}n_{isw}^{open}$
        if ISW_m^{open} corresponding to the fault location
            Set 1st root by $root^{MG}(m, 1) = fb(ISW_m^{open})$
            Set 2nd root by $root^{MG}(m, 2) = tb(ISW_m^{open})$
        else
            Determine a single root node $root^{MG}(m, 1)$ equal to fb or tb of ISW_m^{open} corresponding to the online node
        end if
    end for
    Do the intersection between $\mathbf{root}^{\mathbf{MG}}$ and $\boldsymbol{bus}^{\boldsymbol{on}}$ for eliminating the overlap and selecting only the corresponding online node for forming vector $\boldsymbol{root}^{\boldsymbol{MG}}$
➔ Forming $\mathbf{MG}_t^{\mathbf{set}}$ based on DFS
    for $m = 1{:}n_{root}$
        Do DFS on $\boldsymbol{A}^{\mathbf{MG}}$ for $root_m^{MG}$ then store resulting vector in $\boldsymbol{MG}_m^{\boldsymbol{DFS}}$
        Sort $\boldsymbol{MG}_m^{\boldsymbol{DFS}}$
        Update $\mathbf{MG}^{\mathbf{set0}}(m, 1{:}\,length\ of\ MG_m^{DFS}) = \boldsymbol{MG}_m^{\boldsymbol{DFS}}$
    end for
    Check and eliminate the overlapping set of microgrid(s) in $\mathbf{MG}^{\mathbf{set0}}$
    Store $\mathbf{MG}^{\mathbf{set0}}$ in $\mathbf{MG}_t^{\mathbf{set}}$
end if

3) MICROGRID FORMATION SET

The matrix $\mathbf{MG}_t^{\mathbf{set}}$ is used for indicating the set of possible microgrid formations once the fault is eliminated. In this sense, taking advantage of the Depth First Search (DFS) technique the matrix $\mathbf{MG}_t^{\mathbf{set}}$ for a generic $\boldsymbol{floc}_t$ and $\boldsymbol{ISW}^{site}$ is obtained employing the proposed algorithm described in Table 4 for all $t \in \Omega_T$. This is possible as the DFS technique allows the proposed algorithm able to track a set of microgrid(s) according to their roots noted by $root^{MG}$ which is corresponding to the location of the switch(es). More details about the DFS can be found in [45], [46].

4) MICROGRID FORMATION INDICATORS

In this section, the time dependent microgrid formation indicators are determined. These indicators are the binary matrices and binary vectors representing the time-coupled microgrid tropology and operation, especially during the N-K contingencies scenarios. The methodology applied for determining these indicators is described in the following subsection.

TABLE 5. Algorithm for determining b_t^m.

Algorithm A: formation of $\boldsymbol{b}_t^{\boldsymbol{m}}$

Initialize $\boldsymbol{b}_t^{\boldsymbol{m}}(1{:}n_{bus}) = 1$
if there is no fault(s) happening at time t
    Set vector $\boldsymbol{b}_t^{\boldsymbol{m}}(1{:}n_{bus})$ to 0
else
    Find the set microgrid in $\mathbf{MG}_t^{\mathbf{set}}$ that is adjacent to the main grid through bus 1
    Set $\boldsymbol{b}_t^{\boldsymbol{m}}$ to 0 for all buses corresponding to the set of microgrid that is adjacent to bus 1
end if

a: SYSTEM BUSES OPERATION MODE

The system buses' operation modes are described by matrix $\mathbf{b}^{\mathbf{m}}$. Matrix $\mathbf{b}^{\mathbf{m}}$ assembles the binary vectors $\boldsymbol{b}_t^{\boldsymbol{m}}$ containing the binary elements responsible for indicating the operation mode, i.e., GC or IS, of each system bus; where, the element of $\boldsymbol{b}_t^{\boldsymbol{m}}$ is "1" if the corresponding bus is located in the microgrid area, otherwise "0" for those buses connected to the main grid. The formation of $\boldsymbol{b}_t^{\boldsymbol{m}}$ can be expressed by (71). For the determine $\boldsymbol{b}_t^{\boldsymbol{m}}$, the algorithm in Table 5 is adopted.

$$\boldsymbol{b}_t^{\boldsymbol{m}} = [b_{1,t}^m, b_{2,t}^m, \ldots, b_{n_{bus},t}^m] \tag{71}$$

b: NON-ENERGIZED SYSTEM BUSES

The microgrid can be operated in IS mode when there is at least a single DDG unit localized within the microgrid. In this sense, let a vector $\boldsymbol{MG}_{m,t}^{\boldsymbol{set}}$ define the set of m^{th} microgrid found at time t, if there is no DDG unit installed in $\boldsymbol{MG}_{m,t}^{\boldsymbol{set}}$, this $\boldsymbol{MG}_{m,t}^{\boldsymbol{set}}$ can not operate in IS mode. For this reason, a binary vector $\boldsymbol{bus}_t^{ne}$ is adopt for indicating that the buses within the microgrid cannot be energized due to the lack of local DDG(s); where, the element of $\boldsymbol{bus}_t^{ne}$ is "1" when the corresponding bus is located in a with DDG(s), otherwise "0" for those buses located in microgrids lacking local DDG(s). The general formation for $\boldsymbol{bus}_t^{ne}$ is shown in (72). Then, the general algorithm for determiner $\boldsymbol{bus}_t^{ne}$ for an instance time $t \in \Omega_T$ is shown in Table 6.

$$\boldsymbol{bus}_t^{ne} = [bus_{1,t}^{ne}, bus_{2,t}^{ne}, \ldots, bus_{n_{bus},t}^{ne}] \tag{72}$$

c: FREQUENCY-CONTROLLED BUSES AND DEACTIVATED DDGS

According to (36) there is a need to identify the location of buses with frequency control capability within the microgrid. Nonetheless, if more than a single microgrid is created, the frequency-controlled bus for each formed microgrid should be identified. For this, the vector $\boldsymbol{f}_t^{\boldsymbol{bus}}$ is employed. Its elements indicate the location of frequency-controlled buses for each DDG. Still, there might be cases where a DDG is located

TABLE 6. Algorithm for forming bus_t^{ne}.

Algorithm A: formation of $\boldsymbol{bus}_t^{ne}$
Initialize $\boldsymbol{bus}_t^{ne}(1{:}n_{bus}) = 1$
if there is no fault(s) happening at time t
All buses are energized by GC mode, set $\boldsymbol{bus}_t^{ne}(1{:}n_{bus}) = 1$
else
Define n_{MG} as the number of microgrid(s) from $\mathbf{MG}_t^{\mathbf{set}}$
for $m = 1{:}n_{MG}$
if $\boldsymbol{MG}_{m,t}^{set}$ adjacent to the main grid
do nothing and jump to the next microgrid m of the for **loop**
elseif $\boldsymbol{MG}_{m,t}^{set}$ have a DDG unit installed by checking the element of $\boldsymbol{MG}_{m,t}^{set}$ with $\boldsymbol{DDG}_{sp}^{site}$ as well as confirm that $\boldsymbol{DDG}_{sp}^{size} \neq 0$
do nothing and jump to the next m of for **loop**
else
Define vector index $\boldsymbol{i}^{ne}$ that is equal to the non-zero element of $\boldsymbol{MG}_{m,t}^{set}$
Set $\boldsymbol{bus}_t^{ne}(\boldsymbol{i}^{ne}) = 0$
end if
end for

TABLE 7. Algorithm for determining f_t^{bus} and DDG_t^{down}.

Algorithm A: formation of $\boldsymbol{f}_t^{bus}$ and $\boldsymbol{DDG}_t^{down}$
Initialize vector $\boldsymbol{f}_t^{bus}(1{:}n_{ddg}) = 1$ and vector $\boldsymbol{DDG}_t^{down}(1{:}n_{ddg}) = 1$
if there is no fault(s) happen at time t, it means MG operate in GC mode
Do nothing and let $\boldsymbol{f}_t^{bus}(1{:}n_{ddg})$ and $\boldsymbol{DDG}_t^{down}(1{:}n_{ddg})$ as initial value
else
for $n = 1{:}n_{ddg}$
Initialize $\boldsymbol{h}^{ddg}(1{:}n_{MG}) = 0$
for $m = 1{:}n_{MG}$
if there is an element of $\boldsymbol{MG}_{m,t}^{set}$ corresponding to $DDG_{n,sp}^{site}$
Set $h_m^{ddg} = 1$
else
Set $h_m^{ddg} = 0$
end if
end for
if $\sum \boldsymbol{h}^{ddg} = 0$ means $DDG_{n,sp}^{site}$ are not stay on any MG set in $\mathbf{MG}_t^{\mathbf{set}}$
Set $f_{n,t}^{bus} = DDG_{n,sp}^{site}$ and $DDG_{n,t}^{down} = 0$
else
Set $f_{n,t}^{bus} = \boldsymbol{MG}_{m,t}^{set}(h^{ddg} = 1{,}1)$ and $DDG_{n,t}^{down} = 1$
end if
end for
end if

within the fault area. In this case, the binary vector $\boldsymbol{DDG}_t^{down}$ is used, where elements corresponding to DDGs standing in fault areas are set to zero, otherwise set to "1". (73) and (74) show the formation for $\boldsymbol{f}_t^{bus}$ and $\boldsymbol{DDG}_t^{down}$, respectively.

$$\boldsymbol{f}_t^{bus} = [f_{1,t}^{bus}, f_{2,t}^{bus}, \ldots, f_{n_{ddg},t}^{bus}] \tag{73}$$

$$\boldsymbol{DDG}_t^{down} = [DDG_{1,t}^{down}, DDG_{2,t}^{down}, \ldots, DDG_{n_{ddg},t}^{down}] \tag{74}$$

Table 7 shows the algorithm adopted for determining $\boldsymbol{f}_t^{bus}$ and $\boldsymbol{DDG}_t^{down}$.

d: WT, PV AND ES OPERATION STATUS

WT, PV and ES can not maintain the microgrid operation in IS without DDG support. In this sense, WTs, PVs and ESs that are located inside a non-successful IS microgrid should be deactivated. For this, vectors indicating the WTs, PVs and ESs deactivation status can be determined by simply mapping their location with $\boldsymbol{bus}_t^{ne}$ and can be as expressed by (75a)-(75c).

$$\boldsymbol{WT}_t^{down} = \boldsymbol{bus}_t^{ne}(\boldsymbol{WT}_{sp}^{site}) \tag{75a}$$

$$\boldsymbol{PV}_t^{down} = \boldsymbol{bus}_t^{ne}(\boldsymbol{PV}_{sp}^{site}) \tag{75b}$$

$$\boldsymbol{ES}_t^{down} = \boldsymbol{bus}_t^{ne}(\boldsymbol{ES}_{sp}^{site}) \tag{75c}$$

where, $\boldsymbol{WT}_t^{down}$, $\boldsymbol{PV}_t^{down}$ and $\boldsymbol{ES}_t^{down}$ are the vector containing the status of the WTs (i.e., $WT_{i,t,s,se}^{down}$), PVs (i.e., $PV_{i,t,s,se}^{down}$) and ESs (i.e., $ES_{i,t,s,se}^{down}$) at time t, respectively. Then, $\boldsymbol{WT}_{sp}^{site}$, $\boldsymbol{PV}_{sp}^{site}$ and $\boldsymbol{ES}_{sp}^{site}$ are respectively the vector containing the location of the WTs, PVs and ESs for sample sp.

e: TIME-COUPLED Y^{bus}

The initial system impedance is determined via the original system topology, i.e., $Z_{i,t,s,se} = Z_i^0$. Still, during severe event analysis, the impedance of overhead line branches changes as the system topology adapts, i.e., opening the switch of an overhead line leads to an equivalent impedance $Z_{i,t,s,se} = \infty$. In this sense, the binary matrix **LFa** is used for updating $Z_{i,t,s,se}$ at an instance time t, where the element of **LFa** can be used as a multiplication for modifying the impedance $Z_{i,t,s,se}$ as expressed in (76).

$$Z_{i,t,s,se} = (1/LFa_{i,t,s,se})Z_i^0, \quad \forall i \in \Omega_{BUS},\ \forall t \in \Omega_T,\ \forall s \in \Omega_s' \cup \Omega_s'',\quad \forall se \in \Omega_{se} \tag{76}$$

The time-coupled $\mathbf{Y}_{s,se}^{\mathbf{bus}}$ can be expressed by (77a) using the methodology found in [47]. Conductance matrix **G** and susceptance matrix **B** along the planning horizon Ω_T can be obtained using (77b) and (77c).

$$\mathbf{Y}_{s,se}^{\mathbf{bus}} = \left[\mathbf{Y}_{1,s,se}^{\mathbf{bus}}, \mathbf{Y}_{2,s,se}^{\mathbf{bus}}, \ldots, \mathbf{Y}_{N_T,s,se}^{\mathbf{bus}}\right],\quad \forall s \in \Omega_s' \cup \Omega_s'',\quad \forall se \in \Omega_{se} \tag{77a}$$

$$\mathbf{G}_{s,se} = real\left(\mathbf{Y}_{s,se}^{\mathbf{bus}}\right) \tag{77b}$$

$$\mathbf{B}_{s,se} = imag\left(\mathbf{Y}_{s,se}^{\mathbf{bus}}\right) \tag{77c}$$

C. INTEGRATION OF MICROGRID FORMATION INDICATORS TO INNER LEVEL OPTIMIZATION

In this section, the microgrid formation indicators are integrated into the LOPF problem allowing the capture of multi-microgrid topology and the status of available resources over the planning horizon Ω_T. For this, the LOPF formulation updated according to the multi-microgrid formation indicators is listed as follows:

1) OBJECTIVE FUNCTION

With a new $\boldsymbol{b}_t^{\boldsymbol{m}}$, the formulation (28a) and (28e) were replaced by (78a) and (78b), as shown at the bottom of the next page, to introduce $b_{i,t,s,se}^m$.

2) CONSTRAINTS

The update constraints considering the microgrids formulation indicators can be listed as follows:

$$\left(1 - bus_{i,t,s,se}^{ne}\right) \leq b_{i,t,s,se}^{curt} \leq b_{i,t,s,se}^{m},\quad \forall i \in \Omega_{BUS},\ \forall t \in \Omega_T,\ \forall s \in \Omega_s' \cup \Omega_s'',\ \forall se \in \Omega_{se} \tag{79}$$

$$P_{i,t,s,se} = \begin{pmatrix} \sum_{j\in\Omega_{BUS}} G_{ij,t,s,se} V_{i,t,s,se} \\ -\sum_{j\in\Omega_{BUS}} B_{ij,t,s,se} \delta_{j,t,s,se} \end{pmatrix} = \begin{pmatrix} P^{PCC}_{i,t,s,se} + P^{DDG}_{i,t,s,se} \\ +P^{WT,use}_{i,t,s,se} + P^{PV,use}_{i,t,s,se} \\ +P^{dch}_{i,t,s,se} - \eta^{ES}_i P^{ch}_{i,t,s,se} \\ -P^{L}_{i,t,s,se}\left(1 - b^{curt}_{i,t,s,se}\right) \end{pmatrix}, \quad \forall i \in \Omega_{BUS},\ \forall t \in \Omega_T, \\ \forall s \in \Omega'_s \cup \Omega''_s, \quad \forall se \in \Omega_{se} \tag{80}$$

$$Q_{i,t,s,se} = \begin{pmatrix} -\sum_{j\in\Omega_{BUS}} B_{ij,t,s,se} V_{i,t,s,se} \\ -\sum_{j\in\Omega_{BUS}} G_{ij,t,s,se} \delta_{j,t,s,se} \end{pmatrix} = \begin{pmatrix} +Q^{PCC}_{i,t,s,se} + Q^{DDG}_{i,t,s,se} \\ +Q^{ES}_{i,t,s,se} \\ -Q^{L}_{i,t,s,se}\left(1 - b^{curt}_{i,t,s,se}\right) \end{pmatrix}, \\ \forall i \in \Omega_{BUS}, \quad \forall t \in \Omega_T,\ \forall s \in \Omega'_s \cup \Omega''_s,\ \forall se \in \Omega_{se} \tag{81}$$

$$P^{br}_{k,t,s,se} = \begin{pmatrix} g_{i(k)j(k),t,s,se}\left(V_{i,t,s,se} - V_{j,t,s,se}\right) \\ +b_{i(k)j(k),t,s,se}\left(\delta_{i,t,s,se} - \delta_{j,t,s,se}\right) \end{pmatrix}, \\ \forall k \in \Omega_{LIN}, \quad \forall t \in \Omega_T,\ \forall s \in \Omega'_s \cup \Omega''_s,\ \forall se \in \Omega_{se} \tag{82}$$

$$Q^{br}_{k,t,s,se} = \begin{pmatrix} b_{i(k)j(k),t,s,se}\left(V_{i,t,s,se} - V_{j,t,s,se}\right) \\ +g_{i(k)j(k),t,s,se}\left(\delta_{i,t,s,se} - \delta_{j,t,s,se}\right) \end{pmatrix}, \\ \forall k \in \Omega_{LIN},\ \forall t \in \Omega_T,\ \forall s \in \Omega'_s \cup \Omega''_s,\ \forall se \in \Omega_{se} \tag{83}$$

$$P^{DDG}_{i,t,s,se} = \begin{pmatrix} \left[-k^{i\omega}\left(\delta^{MG}_{f^{bus}_{i,t},t,s,se} - \pi/2\right)\Big/ m^{p}_{i}\right] b^{m}_{i,t,s,se} \\ +\left(1 - b^{m}_{i,t,s,se}\right) P^{DDG}_{i,t,s,se} \end{pmatrix}, \\ \forall i \in \Omega_{DDG}, \quad \forall t \in \Omega_T,\ \forall s \in \Omega'_s \cup \Omega''_s, \\ \forall se \in \Omega_{se} \tag{84}$$

$$Q^{DDG}_{i,t,s,se} = \begin{pmatrix} \left[\left(V^{*}_{i} - V_{i,t,s,se} + u^{v}_{i,t,s,se}\right)\Big/ n^{q}_{i}\right] b^{m}_{i,t,s,se} \\ +\left(1 - b^{m}_{i,t,s,se}\right) Q^{DDG}_{i,t,s,se} \end{pmatrix}, \\ \forall i \in \Omega_{DDG}, \quad \forall t \in \Omega_T,\ \forall s \in \Omega'_s \cup \Omega''_s,\ \forall se \in \Omega_{se} \tag{85}$$

$$V_{i,t,s,se} b^{m}_{i,t,s,se} = V^{**}_{i} b^{m}_{i,t,s,se}, \quad \forall i \in \Omega_{DDG}, \forall t \in \Omega_T,\ \forall s \in \Omega'_s \cup \Omega''_s, \\ \forall se \in \Omega_{se} \tag{86}$$

$$0 \le P^{DDG}_{i,t,s,se} \le \overline{S}^{DDG}_{i} DDG^{down}_{i,t,s,se}, \quad \forall i \in \Omega_{DDG},\ \forall t \in \Omega_T, \\ \forall s \in \Omega'_s \cup \Omega''_s, \quad \forall se \in \Omega_{se} \tag{87}$$

$$\underline{\chi}^{DDG}\overline{S}^{DDG}_{i} DDG^{down}_{i,t,s,se} \le Q^{DDG}_{i,t,s,se} \le \overline{\chi}^{DDG}\overline{S}^{DDG}_{i} DDG^{down}_{i,t,s,se}, \quad \forall i \in \Omega_{DDG}, \\ \forall t \in \Omega_T, \quad \forall s \in \Omega'_s \cup \Omega''_s,\ \forall se \in \Omega_{se} \tag{88}$$

$$0 \le P^{WT}_{i,t,s,se} \le P^{WT,0}_{i,t,s,se} WT^{down}_{i,t,s,se}, \quad \forall i \in \Omega_{WT},\ \forall t \in \Omega_T, \\ \forall s \in \Omega'_s \cup \Omega''_s, \quad \forall se \in \Omega_{se} \tag{89}$$

$$0 \ \text{ł} \ eP^{PV}_{i,t,s,se} \le P^{PV,0}_{i,t,s,se} PV^{down}_{i,t,se}, \quad \forall i \in \Omega_{PV},\ \forall t \in \Omega_T, \\ \forall s \in \Omega'_s \cup \Omega''_s, \quad \forall se \in \Omega_{se} \tag{90}$$

$$0 \le P^{dch}_{i,t,s,se} \le \overline{S}^{ES}_{i} b^{ES}_{i,t,s,se} ES^{down}_{i,t,s,se}, \quad \forall i \in \Omega_{ES},\ \forall t \in \Omega_T, \\ \forall s \in \Omega'_s \cup \Omega''_s, \quad \forall se \in \Omega_{se} \tag{91}$$

$$0 \le P^{ch}_{i,t,s,se} \le \overline{S}^{ES}_{i}\left(1 - b^{ES}_{i,t,s,se}\right) ES^{down}_{i,t,s,se}, \quad \forall i \in \Omega_{ES}, \\ \forall t \in \Omega_T, \quad \forall s \in \Omega'_s \cup \Omega''_s, \quad \forall se \in \Omega_{se} \tag{92}$$

$$\underline{\chi}^{ES}\overline{S}^{ES}_{i} ES^{down}_{i,t,s,se} \le Q^{ES}_{i,t,s,se} \le \overline{\chi}^{ES}\overline{S}^{ES}_{i} ES^{down}_{i,t,s,se}, \quad \forall i \in \Omega_{ES},\ \forall t \in \Omega_T, \\ \forall s \in \Omega'_s \cup \Omega''_s, \quad \forall se \in \Omega_{se} \tag{93}$$

$$-\overline{S}^{TR}_{i}\left(1 - b^{m}_{i,t,s,se}\right) \le P^{PCC}_{i,t,s,se} \le \overline{S}^{TR}_{i}\left(1 - b^{m}_{i,t,s,se}\right), \quad \forall i \in \Omega_{PCC},\ \forall t \in \Omega_T, \\ \forall s \in \Omega'_s \cup \Omega''_s, \quad \forall se \in \Omega_{se} \tag{94}$$

$$\underline{\chi}^{TR}\overline{S}^{TR}_{i}\left(1 - b^{m}_{i,t,s,se}\right) \le Q^{PCC}_{i,t,s,se} \le \overline{\chi}^{TR}\overline{S}^{TR}_{i}\left(1 - b^{m}_{i,t,s,se}\right), \quad \forall i \in \Omega_{PCC}, \\ \forall t \in \Omega_T, \quad \forall s \in \Omega'_s \cup \Omega''_s,\ \forall se \in \Omega_{se} \tag{95}$$

$$V_{i,t,s,se}\left(1 - b^{m}_{i,t,s,se}\right) = V^{GC}_{spec}\left(1 - b^{m}_{i,t,s,se}\right), \quad \forall i \in \Omega_{PCC},\ \forall t \in \Omega_T, \\ \forall s \in \Omega'_s \cup \Omega''_s, \quad \forall se \in \Omega_{se} \tag{96}$$

$$\delta^{PCC}_{i,t,s,se}\left(1 - b^{m}_{i,t,s,se}\right) = 0, \quad \forall i \in \Omega_{PCC},\ \forall t \in \Omega_T, \\ \forall s \in \Omega'_s \cup \Omega''_s, \quad \forall se \in \Omega_{se} \tag{97}$$

where, $G_{ij,t,s,se}$ and $B_{ij,t,s,se}$ are the element of the time-coupled conductance and susceptance matrix denotes the connection of bus i to bus j at time t for s^{th} scenario of season

$$OF^{MILP,MGs}_{s,se} = \sum\nolimits_{t\in\Omega_T} \begin{bmatrix} C^{PCC}_{t,s,se}\left(1 - b^{m}_{i=1,t,s,se}\right) \\ +C^{DDG}_{t,s,se}\left(1 - b^{m}_{\forall i\in\Omega_{DDG},t,s,se}\right) \\ +C^{CURT}_{t,s,se} b^{m}_{\forall i\in\Omega_{BUS},t,s,se} + C^{VI,MGs}_{t,s,se} \end{bmatrix}, \quad \forall s \in \Omega'_s \cup \Omega''_s,\ \forall se \in \Omega_{se} \tag{78a}$$

$$C^{VI,MGs}_{t,s,se} = V_{base}\left(PC^{VI}\left[\sum\nolimits_{i\in\Omega_{BUS}} bus^{ne}_{i,t,s,se}\begin{pmatrix}\left(1 - b^{m}_{i,t,s,se}\right) V^{spec}_{GC} \\ +b^{m}_{i,t,s,se} V^{**}_{i} - V_{i,t,s,se}\end{pmatrix}\right]\right)\Delta t, \quad \forall t \in \Omega_T,\ \forall s \in \Omega'_s \cup \Omega''_s, \\ \forall se \in \Omega_{se} \tag{78b}$$

se, respectively. $g_{i(k)j(k),t,s,se}$ and $b_{i(k)j(k),t,s,se}$ are the time-coupled conductance and susceptance between bus i to j of branch k, at time t for s^{th} scenario of season se. $\delta^{MG}_{f^{bus}_{i,t},t,s,se}$ denotes a phase angle of the frequency controllable bus $f^{bus}_{i,t}$ at time t for s^{th} scenario of season se.

First, (30) is replaced by (79) for allowing the load at the individual bus to curtail during IS mode while forcing $b^{curt}_{i,t} = 1$ for any bus i that corresponds to the bus non-energize $bus^{ne}_{i,t,s,se}$. Then, equations (80)-(84) are power flow constraints considering the microgrids topology using the time-coupled $\mathbf{Y}^{\mathbf{bus}}_{s,se}$. The updated constraints for the DDG units are expressed by (84)-(85). Compared to (36)-(38), $b^{m}_{i,t,s,se}$ is introduced in (84)-(86), allowing the problem consideration of an individual DDG unit's operation, i.e., GC or IS mode. Moreover, for (84), $\delta^{MG}_{f^{bus}_{i,t},t,s,se}$ is dependent on frequency-controlled buses. Eqs. (42) and (43) are replaced by (87) and (88) for accounting for the status of the DDG units i.e., online or failure. The inequalities (89)-(93) guarantee that WTs, PVs and ESs are deactivated in case they are located inside a non-successful IS microgrids. Finally, eqs. (94)-(97) defined the updated power exchange constraints by introducing $b^{m}_{i,t}$.

3) MILP MODEL FOR LOPF CONSIDERING MICROGRIDS FORMATION

According to the updated LOPF problem formulation, the MILP model used for the deep-learning approach can be summarized as follows:

$$\min_{\boldsymbol{X}_{MILP}} OF^{MILP,MGs}_{s,se} \tag{98}$$

Subject to:

- Voltage and load curtailment constraints: (29), (79)
- Power flow constraints: (80)-(83), (35)
- DDG operation constrains: (39)-(41), (44), (45), (84)-(88)
- WT and PV operation constrains: (89), (90)
- ESS operation constraints: (48), (52)-(55), (91)-(92)
- Power exchange constraints: (58), (59), (94)-(97)

D. DEEP NEURAL NETWORK (DNN) MODEL

At this stage, for each sample *sp*, the identified targets (64)-(66) can be calculated using the results obtained by the LOPF solution. Then, a set of sample inputs $\mathbf{IN^{dnn}}$ and the calculated targets (64)-(66) are used for training the DDN models, wherein 70% of the samples were arbitrarily selected for the training procedure and the remaining samples for the testing procedure. For simplicity, a single DNN model is trained for predicting the single identification target. In this work, each DDN model employed is formed as a multi-layer feedforward neural network with three levels, i.e., a single input layer, several hidden layers and a single output layer [48], [49]. Fig. 8 shows the basic scheme for a multi-layer feed-forward neural network architecture.

According $\mathbf{IN^{dnn}}$ and targets (64)-(66), a general DNN model architecture designed for a single sample can be

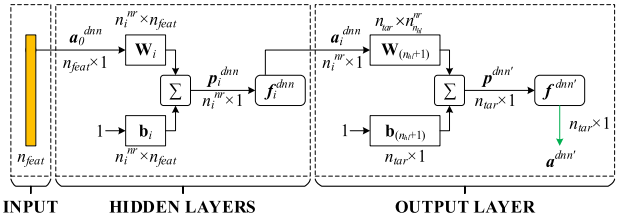

FIGURE 8. General scheme of multi-layer feed-forward neural network architecture for predicting a single identified target.

expressed by (99)-(101).

$$\boldsymbol{a}^{\boldsymbol{dnn}}_{0,sp} = \boldsymbol{IN}^{\boldsymbol{dnn}}_{sp}, \quad sp \in \Omega_{SAM} \tag{99}$$

$$\boldsymbol{a}^{\boldsymbol{dnn}}_{i,sp} = f^{dnn}_{i}\left(\mathbf{W}_i \boldsymbol{a}^{\boldsymbol{dnn}}_{i-1,sp} + \mathbf{b}_i\right), \quad i = 1, 2, .., n_{hl},\ sp \in \Omega_{SAM} \tag{100}$$

$$a^{dnn'}_{sp} = f^{dnn'}\left(\mathbf{W}_{n_{hl}+1} \boldsymbol{a}^{\boldsymbol{dnn}}_{n_{hl},sp} + \mathbf{b}_{n_{hl}+1}\right), \quad sp \in \Omega_{SAM} \tag{101}$$

The input layer of the hidden layer receives the vector of input $\boldsymbol{a}^{\boldsymbol{dnn}}_{0,sp}$ expressed by (99). Then, each layer in the hidden layer computes their neuron pre-activation $\boldsymbol{p}^{\boldsymbol{dnn}}_{i,sp}$ regarding the weight matrix (i.e., $\mathbf{W}_i$) and biases vector (i.e., $\mathbf{b}_i$), the activation function $f^{dnn}_{i}(.)$ employed to $\boldsymbol{p}^{\boldsymbol{dnn}}_{i,sp}$ for delivering the neuron activation for the next layer (100). In the end, the output layer computes a single prediction neuron activation, $n_{tar} = 1$, using the neuron activation $\boldsymbol{a}^{\boldsymbol{dnn}}_{n_{hl},sp}$ that is obtained by the last layer of the hidden layer (101). In this work, $f^{dnn}_{i}(.)$ is a sigmoid activation function for the hidden layer, while the output layer linear activation function is denoted by $f^{dnn'}(.)$ is used. Finally, the DNN model has been trained via the Bayesian Regularization Backpropagation (BRB) algorithm [48]. This algorithm is a backpropagation-based approach focused on minimizing the mean sum of squares of the network errors (MSE) during the DDN model training. Moreover, seeking to minimize and make the network response smoother, as well as likely to reduce overfitting impact [48], [50]. The proposed algorithm also includes the network regularization based on the network sum of mean square weights (MSW).

As can be seen in Fig. 6, the prediction obtained by the trained DDN model should satisfy the criteria. In this work, the errors indicated in (102) have been used as a criterion calculated for every round of DNN training completion. Then, (103) and (104) are calculated for illustrating the performance of the model for different types of errors.

$$e^{dnn}_{1} = 100\% \times \max\left(\frac{\left|TG_{sp} - net^{n}\left(\boldsymbol{IN}^{\boldsymbol{dnn}}_{sp}\right)\right|}{TG_{sp}}\right), \quad \forall sp \in \Omega^{test}_{SAM} \tag{102}$$

$$e^{dnn}_{2} = \text{mean}\left(\left|TG_{sp} - net^{n}(\boldsymbol{IN}^{\boldsymbol{dnn}}_{sp})\right|\right), \quad \forall sp \in \Omega^{test}_{SAM} \tag{103}$$

$$e_3^{dnn} = 100\% \times \frac{mean\left(\left|TG_{sp} - net^n(\boldsymbol{IN}_{sp}^{\boldsymbol{dnn}})\right|\right)}{mean\left(TG_{sp}\right)}, \quad \forall sp \in \Omega_{SAM}^{test} \tag{104}$$

where, $net^n\left(\boldsymbol{IN}_{sp}^{\boldsymbol{dnn}}\right)$ is the prediction results for the input sample $\boldsymbol{IN}_{sp}^{\boldsymbol{dnn}}$ using the DNN model corresponding to target n. First, e_1^{dnn} represents the relative error between the prediction and real value. In this case, we apply a maximum for delivering the worst error over the vector of relative error. Then, e_2^{dnn} and e_3^{dnn} represent the mean absolute and relative errors, presenting more generalized perspectives in comparison to e_1^{dnn}.

In this work, the hyper parameters are randomly selected for every round of DNN training, i.e., (a) activation function for hidden layers, (b) activation function for outer layer, (c) number of layers and corresponding neurons in the hidden layers. According to the BRB algorithm, the training round stops if the sum squared error and the sum squared weights are not improved over subsequent training iterations (epochs) [48], [50]. Then, trained DNN models are validated through the testing set until satisfying the criteria e_1^{dnn} threshold, guaranteeing that the worst relative error between the target and prediction is less than e_1^{dnn}. Finally, trained DNN models are used for predicting the targets and calculating the LOPF dependent indices $RESI^{OLEV}$, $AOMC^{DDG}$, $AEMIS^{DDG}$ and $AEMIS^{GRID}$ for the outer level. In this sense, let $net^n(\boldsymbol{X_{OLEV}})$ be a trained DDN network for target n depending on $\boldsymbol{X_{OLEV}}$, the LOPF dependent indices for the outer level calculated using the trained DNN model can be expressed by (105)-(109b).

$$RESI^{OLEV,dl} = net^1(\boldsymbol{X_{OLEV}}), \quad \forall sp \in \Omega_{SAM} \tag{105}$$

$$TC^{OLEV,dl} = \begin{pmatrix} C^{DDG,dl} + C^{WT} \\ +C^{PV} + C^{ES} + C^{ISW} \end{pmatrix} \tag{106}$$

$$C^{DDG,dl} = CPC^{DDG} + TL \times AOMC^{DDG,dl} \tag{107a}$$

$$AOMC^{DDG,dl} = net^2\left(\boldsymbol{X_{OLEV}}\right) \times \left(\frac{365}{4} S_{base}\left(\sigma^{fuel} \Big/ \eta^{DDG} + \sigma_{O\&M}^{DDG}\right)\right) \tag{107b}$$

$$AEMIS^{OLEV,dl} = AEMIS^{DDG,dl} + AEMIS^{GRID,dl} \tag{108}$$

$$AEMIS^{DDG,dl} = net^2(\boldsymbol{X_{OLEV}})(\frac{365}{4} S_{base} K_{CO2}^{DDG}), \quad \forall sp \in \Omega_{SAM} \tag{109a}$$

$$AEMIS^{GRID,dl} = net^3(\boldsymbol{X_{OLEV}})(\frac{365}{4} S_{base} K_{CO2}^{GRID}), \quad \forall sp \in \Omega_{SAM} \tag{109b}$$

VI. STAGE IV: SOLUTION FOR OPTIMUM PLANNING

The proposed multi-objective optimization problem incorporating the DNN models for the resilience-oriented planning of microgrids can be summarized as follows:

$$\min_{\boldsymbol{X_{OLEV}}} \left(RESI^{OLEV,dl}, TC^{OLEV,dl}, AEMIS^{OLEV,dl}\right) \tag{110}$$

s.t.:

- DERs size constraint: (23), (24)
- Maximum allowable bus power constraint: (25)
- ISWs and DERs installation constraints: (26), (27)

The proposed problem has been solved using the population-based multi-objective optimization approach NSGA-II [51]. Fig. 9 shows the general outline of the proposed optimum planning NSGA-II based on DNN models. The NSGA-II is widely used for multi-objective optimization problems due to its computational efficiency and faster convergence compared to the other techniques [51]. Moreover, the solution delivered by NSGA-II is closed to the true Pareto-optima frontier [51]. Additional details on NSGA-II and its implementation can be found in [51].

In the beginning, the first iteration at $gen = 0$ the NSGA-II starts generating an initial random parent population with n_{pop} individuals. In this work, a single individual includes the combination of the genes representing the allocation of the planning elements i.e., ISWs, DDGs, WTs, PVs and ESs. Fig. 10 shows the structure of an individual or a chromosome. Then, considering every single individual, the multi-objective function can be determined from two directions A and B. For the following iteration $gen > 0$ the NSGA-II starts forming an n_{pop} child offspring population using the genetic operators, i.e., selection, crossover, and mutation [51]. Similar to the parent population, the multi-objective functions are evaluated for n_{pop} child individuals, and a new parent population is determined.

First, the child population is combined with the parent population forming a mixed population with $2 \times n_{pop}$ individuals. Then, a new parent population is developed by selecting n_{pop} individuals from the mixed population using the fast non-dominated sorting technique [51]. According to this technique, individual(s) classified in the lowest rank of the frontier are selected and moved up to the highest frontier until the number of selected individuals reach n_{pop}. If the last ranked individuals cause the quantity to exceed n_{pop}, the crowding distance is applied for selecting the remainder individuals. This process is repeated until satisfy the NSGA-II criteria.

VII. NUMERICAL RESULTS

To validate the proposed method, the IEEE 33-bus test system is selected. This system is a typical distribution network with the ability to be disconnected from the main grid via the main isolated switch, i.e., ISW^{sub}, installed at the upstream interfacing substation. Distribution lines infrastructure is assumed as a typical overhead power line, with loads weighing coefficient proportional to the annual peak load, Fig. 11, similar to the work found in [19]. The wind speed and irradiance data sets are obtained via the scenario generation procedure described in Section III using fast forward reduction. For this,

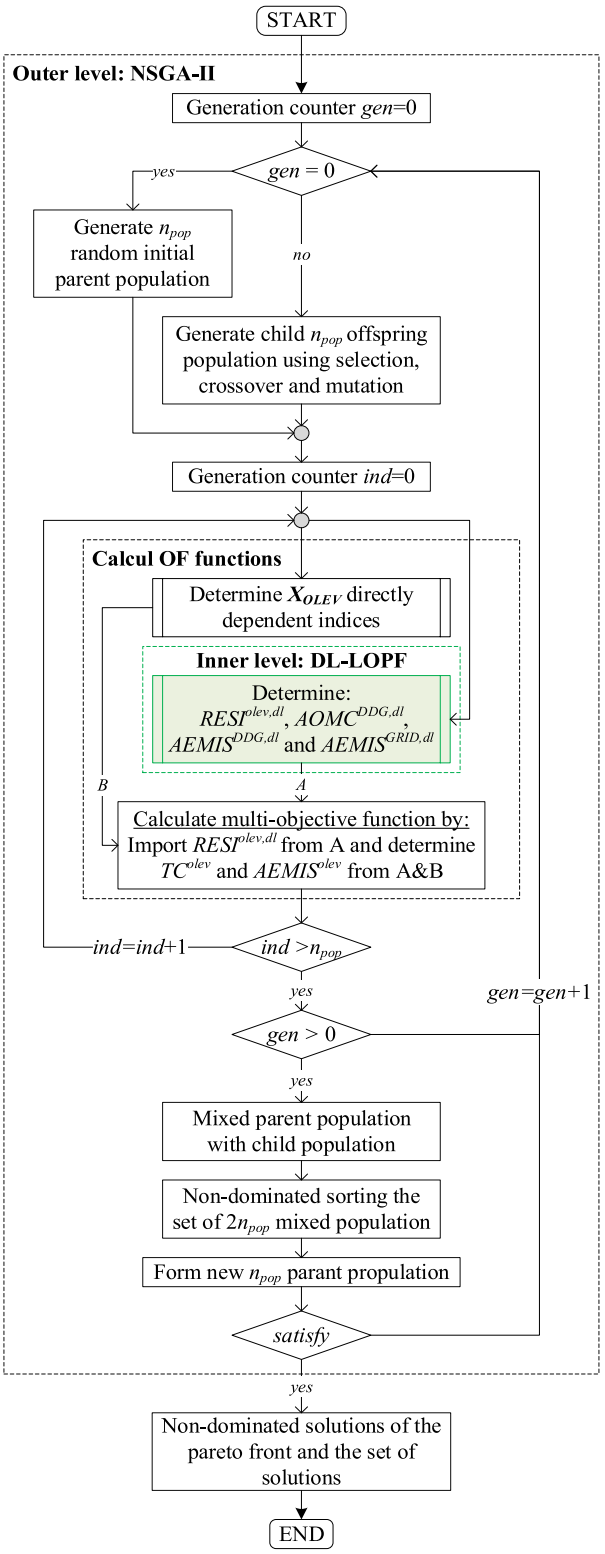

FIGURE 9. Optimum planning approach.

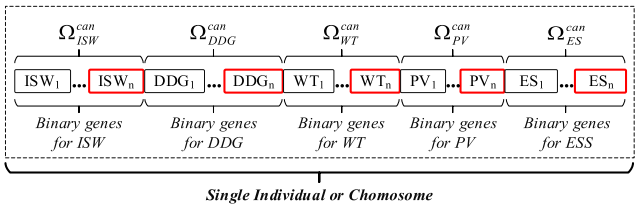

FIGURE 10. Structure of chromosome for NSGA-II.

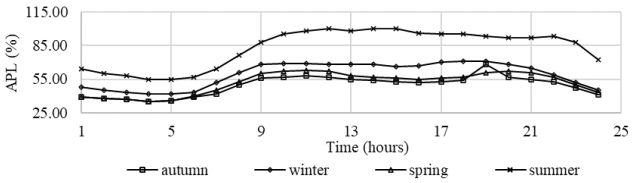

FIGURE 11. Seasonal annual load pattern.

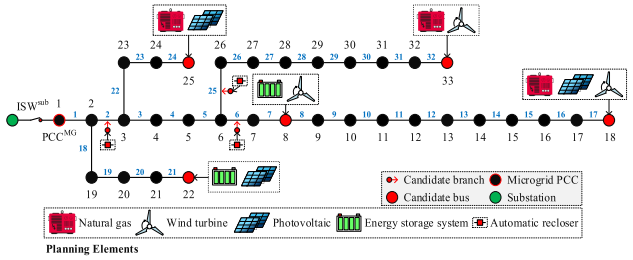

FIGURE 12. 33-bus test system with candidate buses and branches.

data series extracted from NREL [52] comprising the hourly profile for 10 years, respectively 2008-2017 for Victoria-BC, Canada, of wind speed in MPH (miles per hour) and for irradiance in w/m^2 are employed. Details pertaining to the obtained set of scenario reductions are shown in Table 8. Based on the obtained data sets, the most vulnerable wind scenarios summarized in Table 9 are used for generating severe operation scenarios. For accounting for the uncertainty of the N-K contingencies, N_s^{pre} is set sufficiently high, $N_s^{pre} = 10000$, allowing for the selection of 5 scenarios for each season se. This procedure steps are detailed depicted in Section III, and the parameters related to the scenario generation are summarized in Table 10. The daily market electricity price is extracted from NYISO [53], where corresponding days and years are shown in Table 8 and Table 9. The test system candidate buses and branches for the planning elements are shown in Fig. 12, with main characteristics summarized in Table 11 [54].

The proposed planning framework is developed in MATLAB environment, including the DNN models training procedure, the implementation of NSGA-II and the validation procedure. It is worth noting that the technology sodium sulfur (NaS) was selected for the ESs due to its high number of lifecycles. In this work, the ES capacity rating is proportional to their power rating, similarly to the work in [55]. In this case, the ratio between the rated capacity and rated power is set to 5 for all ESs. This number was extracted from the optimal solution found in [33]. Additionally, the maximum DoD is arbitrary set to 70% to provide a balance between the battery lifecycle and its generation capability. The DDGs

TABLE 8. Set of scenarios and their probability obtained by fast forward selection and their corresponding calendar day/year for WT and PV.

Season		Details
Fall	Scenario	{80, 352, 694, 717, 718}
	Day #	324, 322, 300, 323, 324
	Year	2008, 2011, 2015, 2015, 2015
	$\pi_{s,se}^{wiso}$	{0.385, 0.024, 0.519, 0.048, 0.024}
Winter	Scenario	{291, 554, 586, 669, 854}
	Day #	352, 342, 374, 366, 369
	Year	2011, 2014, 2014, 2015, 2017
	$\pi_{s,se}^{wiso}$	{0.042, 0.403, 0.120. 0.093. 0.341}
Spring	Scenario	{34, 103, 127, 563, 564}
	Day #	94, 71, 95, 76, 77
	Year	2008, 2009, 2009, 2014, 2014
	$\pi_{s,se}^{wiso}$	{0.111, 0.021, 0.447, 0.405, 0.016}
Summer	Scenario	{152, 341, 342, 525, 619}
	Day #	212, 219, 220, 221, 224
	Year	2009, 2011, 2011, 2013, 2014
	$\pi_{s,se}^{wiso}$	{0.523, 0.335, 0.014, 0.067, 0.061}

TABLE 9. The most vulnerable wind scenarios and their corresponding date.

Season	Corresponding date			$max\ (v_{se}^{worst})$	
	day	*month*	*year*	*m/s*	$(m/s)^{gust}$
Fall	19	November	2012	15.83	20.37
Winter	18	January	2011	16.11	20.74
Spring	12	Mars	2012	16.66	21.44
Summer	01	June	2010	15.55	20.01

TABLE 10. Parameter for generating scenario.

Parameters	Unit	Set belong	Values
N_s^{pre}	-	-	10000
N_s'/N_s''	-	-	5/5
v_i^{ci}	m/s	$\forall i \in \Omega_{WT}^{can}$	4
v_i^{co}	m/s	$\forall i \in \Omega_{WT}^{can}$	26
v_i^{ra}	m/s	$\forall i \in \Omega_{WT}^{can}$	16
R_i^C	kW/m^2	$\forall i \in \Omega_{PV}^{can}$	0.15
R_i^{STD}	kW/m^2	$\forall i \in \Omega_{PV}^{can}$	1
k^{gust}	-	-	1.287
$\mu_i^{pole}/\sigma_i^{pole}$	-	$\forall i \in \Omega_{LIN}$	65/15
$\mu_i^{cond}/\sigma_i^{cond}$	-	$\forall i \in \Omega_{LIN}$	47/9
$\pi^{br,nvul}$	-	-	0.05
$v_{cri}^{low}/v_{cri}^{high}$	m/s	-	20/40
$MTTR^{nw}$	h	-	2
h_1^{low}/h_2^{low}	h	-	2/3
h_1^{high}/h_2^{high}	h	-	3/4

is the natural gas type which can be operated in PQ mode, during GC mode, and droop/2nd, during IS mode. The general parameters used in this research are summarized in Table 12.

A. DEEP LEARNING SOLUTION VALIDATION

In this section, the performance of the trained DDN models is evaluated. As discussed in Section V, a single model is used for predicting the single target. The corresponding hyper-parameters for each DNN model architecture are summarized in Table 13. The number of samples is 40000 including 70% for the training set and 30% for the testing set. Taking advantage of the BRB algorithm, training is terminated if the sum squared error and the sum squared weights are not relatively improved over successive training iterations (epochs) [48], [50]. Additionally, an e_1^{dnn} threshold of 10% is considered

TABLE 11. Characteristic of the 33-bus test system.

Line No.	*fb* #	*tb* #	*R* (ohm)	*X* (ohm)	L^{br} (m)	N_i^{pole}	P_{tb}^{Lpeak} (kW)	Q_{tb}^{Lpeak} (kVar)	w^{load}
1	1	2	0.092	0.047	100	4	100	60	0.027
2	2	3	0.492	0.251	500	14	90	40	0.024
3	3	4	0.365	0.186	350	10	120	80	0.032
4	4	5	0.380	0.194	350	10	60	30	0.016
5	5	6	0.817	0.706	800	21	60	20	0.016
6	6	7	0.187	0.618	200	6	200	100	0.054
7	7	8	0.710	0.235	700	19	200	100	0.054
8	8	9	1.028	0.739	1000	26	60	20	0.016
9	9	10	1.042	0.739	1000	26	60	20	0.016
10	10	11	0.196	0.065	200	6	45	30	0.012
11	11	12	0.374	0.124	350	10	60	35	0.016
12	12	13	1.465	1.153	1500	39	60	35	0.016
13	13	14	0.540	0.711	550	15	120	80	0.032
14	14	15	0.590	0.525	600	16	60	10	0.016
15	15	16	0.745	0.544	750	20	60	20	0.016
16	16	17	1.286	1.718	1300	34	60	20	0.016
17	17	18	0.731	0.573	700	19	90	40	0.024
18	2	19	0.164	0.156	150	5	90	40	0.024
19	19	20	1.501	1.353	1500	39	90	40	0.024
20	20	21	0.409	0.477	400	11	90	40	0.024
21	21	22	0.707	0.935	700	19	90	40	0.024
22	3	23	0.450	0.308	450	12	90	50	0.024
23	23	24	0.896	0.708	900	24	420	200	0.113
24	24	25	0.894	0.700	900	24	420	200	0.113
25	6	26	0.203	0.103	200	6	60	25	0.016
26	26	27	0.284	0.144	300	9	60	25	0.016
27	27	28	1.057	0.932	1000	26	60	20	0.016
28	28	29	0.802	0.699	800	21	120	70	0.032
29	29	30	0.506	0.258	500	14	200	600	0.054
30	30	31	0.972	0.961	950	25	150	70	0.040
31	31	32	0.310	0.361	300	9	210	100	0.057
32	32	33	0.340	0.529	350	10	60	40	0.016
						Total	**3715**	**2300**	

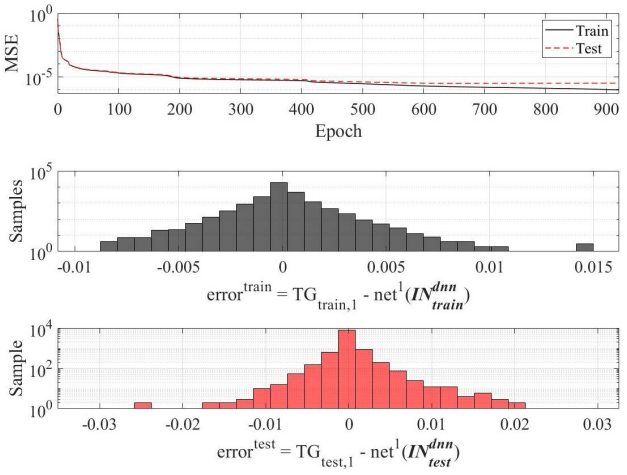

FIGURE 13. MSE over epoch, distributed error of training set and test set of the first DNN model for predicting TG_1.

for guaranteeing the accuracy of the DNN models. In this case, the Fig. 13, 14 and 15 illustrate the training/testing MSE and distributed error of the DNN model for predicting $TG_{sp,1}$, $TG_{sp,1}$ and $TG_{sp,1}$, respectively. To this end, the performance of the trained DNN models are summarized in Table 14.

Analyzing Table 14, one can draw conclusions regarding the DDN models errors for the three targets of interest. First, the MSE, RMSE, and max $|y|$ for the training and

TABLE 12. General parameters.

Elements	Parameters	Unit/detail	Values	Level problem	
				outer	inner
DDG	σ^{fuel}	\$/kWh	0.0205	✓	✓
	η_i^{DDG}	per unit	0.370	✓	✓
	σ_{INV}^{DDG}	\$/kW	1300	✓	✓
	$\sigma_{O\&M}^{DDG}$	\$/kWh	0.003	✓	✓
	K_{CO2}^{DDG}	kg/kWh	201.6	✓	-
	Mode	for GC/IS	PQ/2[nd]	-	✓
	$\overline{P}_i^{DDG}$	MW	4.0	✓	-
	P_{step}^{DDG}	kW	100	✓	-
	V^*/V^{**}	p.u.	1.01/1.05	-	✓
	ki^{ω}	-	4	-	✓
	$PF_i^{DDG,1st}$	-	0.4	-	✓
	$PF_i^{DDG,4th}$	-	0.4	-	✓
	$\underline{\chi}^{DDG}/\overline{\chi}^{DDG}$	-	-0.2/0.6	-	✓
WT	σ_{INV}^{WT}	\$/kW	1686	✓	-
	$\sigma_{O\&M}^{WT}$	\$/kW/year	46	✓	-
	Mode	for GC/IS	PQ[unity]	-	✓
	$\overline{P}_i^{WT}$	MW	0.6	✓	-
	P_{step}^{WT}	kW	100	✓	-
PV	σ_{INV}^{PV}	\$/kW	2277	✓	-
	$\sigma_{O\&M}^{PV}$	\$/kW/year	21	✓	-
	Mode	for GC/IS	PQ[unity]	-	✓
	$\overline{P}_i^{PV}$	MW	0.3	✓	-
	P_{step}^{PV}	kW	100	✓	-
ES	$\sigma_{INV}^{ES,P}$	\$/kW	300	✓	-
	$\sigma_{O\&M}^{ES}$	\$/kW/year	80	✓	-
	$\sigma_{INV}^{ES,E}$	\$/kWh	350	✓	-
	σ_{INS}^{ES}	\$/kWh	8	✓	-
	Mode	for GC/IS	PQ	-	✓
	$\overline{P}_i^{ES}$	MW	0.3	✓	-
	P_{step}^{ES}	kW	100	✓	-
	r^{ES}	-	5	✓	✓
	DoD^{max}	%	70	-	✓
	η_i^{ES}	%	95	-	✓
	SoC^0	%	50	-	✓
	$\underline{\chi}^{ES}/\overline{\chi}^{ES}$	-	-0.6/0.6	-	✓
TR	$\overline{S}^{TR}$	kVA	5300	-	✓
	$\underline{\chi}^{TR}/\overline{\chi}^{TR}$	-	-0.6/0.6	-	✓
	$PF_i^{TR\_1st}$	-	0.75	-	✓
	$PF_i^{TR\_4th}$	-	0.75	-	✓
	V_{pcc}	p.u.	1.05	-	✓
Network	$\overline{P}_i^{bus}$	kVA/ph	6.00[a],4.00[b]	✓	-
	$\overline{I}_{k=1\to8}^{br}$	A/Ψ	500	-	✓
	$\overline{I}_{k=9\to32}^{br}$	A/Ψ	350	-	✓
SSW	σ_{INV}^{SSW}	\$/SSW	64.3	✓	-
	$\sigma_{O\&M}^{SSW}$	\$/h	1.15	✓	-
General	N_T	h	24	-	✓
	TL	year	10	✓	-
	K_{CO2}^{GRID}	kg/kWh	143	✓	-
	σ^{curt}	\$/kWh	3.4	-	✓
	PC^{VI}	\$/kV	1.1	-	✓
	S_{base}	kVA	1000	✓	✓
	V_{base}	kV	12.66	-	✓
	$\varphi_{sel}^{1st,4th}$	deg.	90	-	✓
	$n_{pw}^{1st,4th}$	-	15	-	✓

testing procedures are found around 10^{-4} to 10^{-7}, 10^{-2} to 10^{-4}, and 10^{-1} to 10^{-2} ranges, for all targets. These results indicate the developed method significant ability to infer adequate optimal solutions, presenting errors significantly smaller than accepted deviations. Where respective

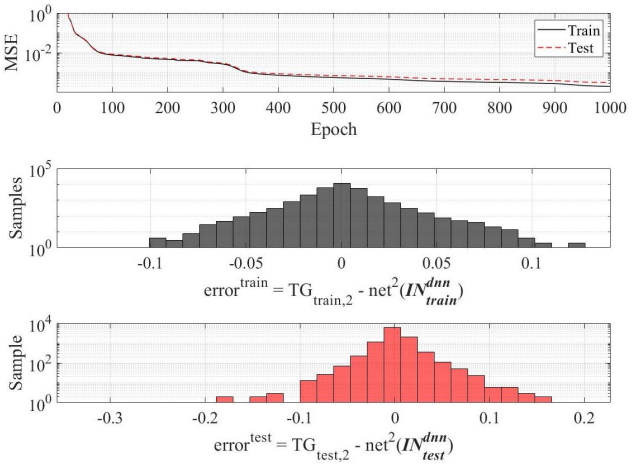

FIGURE 14. MSE over epoch, distributed error of training set and test set of the first DNN model for predicting TG_2.

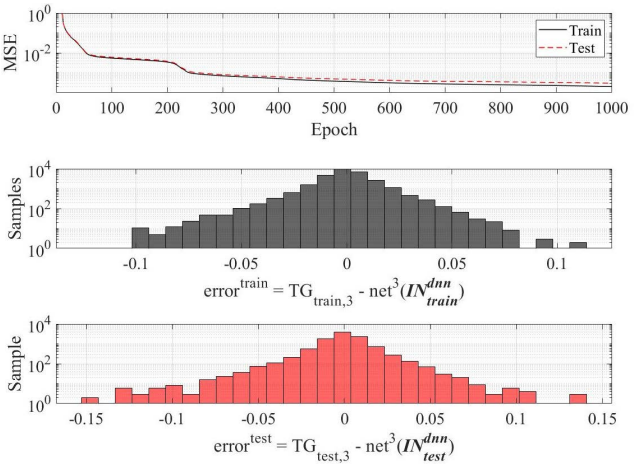

FIGURE 15. MSE over epoch, distributed error of training set and test set of the first DNN model for predicting TG_3.

TABLE 13. Hyper-parameters setting for DNN models' architectures.

Hyper-parameters	DNN Tanning Targets		
	$TG_{sp,1}$	$TG_{sp,2}$	$TG_{sp,3}$
No. of hidden layer	3	3	3
No. of neurons for hidden layer	25-130-25	25-80-25	25-60-25
Activation fcn. for hidden layer	log-sigmoid	log-sigmoid	log-sigmoid
Activation fcn. for output layer	linear	linear	linear
log-sigmoid: Logistic sigmoid activation function			

variations in the errors range are due to the different units under consideration. In terms of the criteria, the e_1^{dnn} obtained for $TG_{sp,2}$, $TG_{sp,2}$ and $TG_{sp,3}$ are found less than the 10% threshold. The e_2^{dnn} is found at 7.75×10^{-4}, 1.06×10^{-2} kWh and 1.09×10^{-2} kWh for $TG_{sp,2}$, $TG_{sp,2}$ and $TG_{sp,3}$, respectively. Finally, e_3^{dnn} shows the ratio in percentage for e_2^{dnn} over the mean target, leading to an error of less than 1%.

TABLE 14. Performance of trained DNN models.

Indicators	Set	Training targets		
		$TG_{sp,1}$ -	$TG_{sp,2}$ (kWh)	$TG_{sp,3}$ (kWh)
MSE	Train	9.29×10^{-7}	2.03×10^{-4}	2.04×10^{-4}
	Test	3.13×10^{-6}	3.14×10^{-4}	3.00×10^{-4}
RMSE	Train	9.64×10^{-4}	1.43×10^{-2}	1.43×10^{-2}
	Test	1.77×10^{-3}	1.77×10^{-2}	1.73×10^{-2}
$max\|y\|$	Train	1.50×10^{-2}	1.36×10^{-1}	1.23×10^{-1}
	Test	3.15×10^{-2}	3.29×10^{-1}	1.52×10^{-1}
e_1^{dnn} (%)	-	7.96	1.97	0.09
e_2^{dnn} (kWh)	-	7.75×10^{-4}	1.06×10^{-2}	1.09×10^{-2}
e_3^{dnn} (%)	-	1.44×10^{-1}	2.80×10^{-2}	0.63×10^{-2}

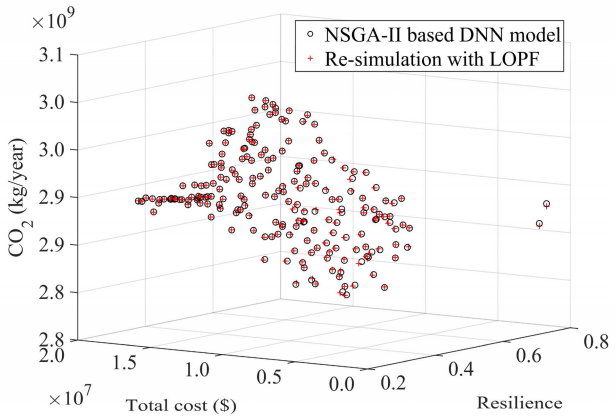

FIGURE 16. Comparison multi-objective solutions obtained by proposed NSGA-II based DNN model and their corresponding real values.

B. NSGA-II PERFORMANCE BASED DNN MODEL

In this section, the performance of the proposed NSGA-II based DNN model is evaluated. The NSGA-II is responsible for generating the multi-objective problem solution according to the Pareto frontier. In this work, the maximum number of iterations and the population are set to 1000. The crossover and mutation probability is set to 0.8 and 0.01, respectively. These parameters were selected based on the guidelines available in [51], [56].

The solutions obtained include the $\mathbf{X_{OLEV}}$ and the values of the multi-objective function are based on DNN models' prediction. To validate these solutions, first, the LOPF problem (98) is re-simulated for the obtained solution $\mathbf{X_{OLEV}}$. Then, the solution obtained by re-simulating the LOPF is used for calculating the real values of multi-objective functions. Then, R-square (R^2) and error indices (102)-(104) are calculated for evaluating the error between real objective functions and those obtained by (98).

Fig. 16 shows the comparison between the real multi-objective functions results and those obtained by (98).

Then, Fig. 17, 18 and 19 illustrate the probability density as a histogram and the cumulative density of the set of errors $\boldsymbol{e_1^{OLEV*}}$ for $\boldsymbol{RESI^{OLEV}}$, $\boldsymbol{TC^{OLEV}}$ and $\boldsymbol{AEMIS^{OLEV}}$, respectively. Where, $\boldsymbol{e_1^{OLEV*}}$ denotes the set of relative errors,

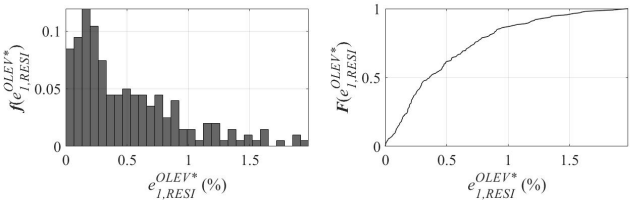

FIGURE 17. Probability density as histogram and cumulative density curve of relative error $e_{1,RESI}^{OLEV*}$ for $RESI^{OLEV}$.

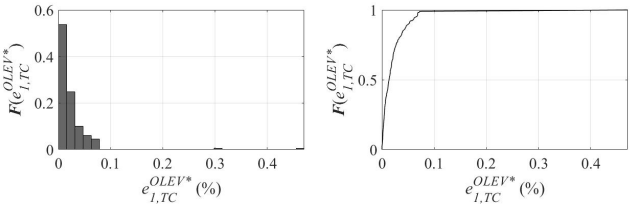

FIGURE 18. Probability density as histogram and cumulative density curve of relative error $e_{1,TC}^{OLEV*}$ for TC^{OLEV}.

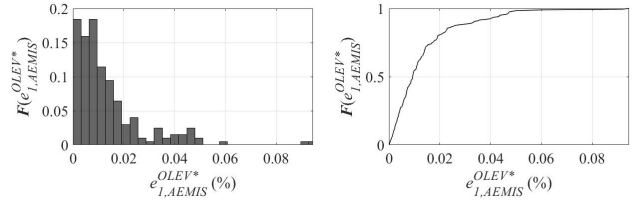

FIGURE 19. Probability density as histogram and cumulative density curve of relative error $e_{1,AEMIS}^{OLEV*}$ for $AEMIS^{OLEV}$.

TABLE 15. Performance of NSGA-II.

Indicators	NSGA-II objective functions		
	$RESI^{OLEV}$	TC^{OLEV}	$AEMIS^{OLEV}$
R^2	0.9993	1.000	0.9999
e_1^{OLEV}	1.98 (%)	4.71×10^{-1} (%)	9.45×10^{-2} (%)
e_2^{OLEV}	1.84×10^{-3}	1.57×10^{3} ($/year)	3.94×10^{5} (kg/year)
e_3^{OLEV}	5.27×10^{-1} (%)	1.69×10^{-2} (%)	1.36×10^{-2} (%)

compared to the max/worst relative error with $e_1^{OLEV} = \max\left(\boldsymbol{e_1^{OLEV*}}\right)$.

Finally, Table 15 summarizes the R^2 and errors indices between both sets of solutions. The R^2 obtained for the three objective functions are close to 1.00, e_1^{OLEV} for all objective functions are less than 2%, whereas e_2^{OLEV} and e_3^{OLEV} indicate absolute and relative errors of less than 1%.

C. OPTIMAL PLANNING SOLUTION

This section presents the optimal planning solution wherein the solution is positioned in the Pareto frontier respecting the NSGA-II behavior. In this case, the solution can be classified into two groups according to the 3D plan for multi-objective function solutions shown in Fig. 20.

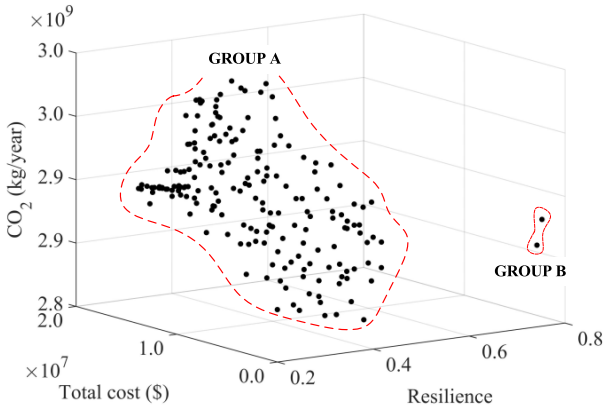

FIGURE 20. Classification in Group A and Group B for the multi-objective function's solution obtained by NSGA-II based DNN model.

TABLE 16. Planning solution corresponding the max/min in each objective function for group A and the planning solution for group B.

Group	No.	Binary allocation size of DDGs, WTs, PVs and ESs		$RESI^{OLEV}$	TC^{OLEV} ($/year)	$AEMIS^{OLEV}$ (kg/year)
A	1	*1-4-1*	*/1-2-1/2-1-2/1-1*	**0.512**	4.53×10^{6}	2.85×10^{9}
	2	*10-16-14*	*/5-5-4/4-4-4/3-3*	**0.275**	1.53×10^{7}	2.90×10^{9}
	3	*3-30-30*	*/4-4-4/4-4-4/3-3*	0.284	$\mathbf{1.78\times10^{7}}$	2.89×10^{9}
	4	*1-4-1*	*/1-2-2/1-1-1/1-1*	0.506	$\mathbf{4.24\times10^{6}}$	2.87×10^{9}
	5	*8-16-15*	*/1-2-1/1-1-1/1-1*	0.276	9.76×10^{6}	$\mathbf{3.02\times10^{9}}$
	6	*1-4-2*	*/3-3-3/4-3-4/2-2*	0.478	7.93×10^{6}	$\mathbf{2.79\times10^{9}}$
B	1	*0-2-2*	*/0-0-0/0-1-1/0-0*	0.773	1.53×10^{6}	2.86×10^{9}
	2	*0-2-2*	*/0-0-0/0-0-0/0-0*	0.774	1.03×10^{6}	2.88×10^{9}

Group A corresponds to the solution of $\mathbf{X_{OLEV}}$ where all three ISWs are installed on candidate branches of the test system. These solutions present variations due to the allocation of different DDGs sizes in the candidate buses and their deployment for maintaining the microgrid operation in IS mode. Thus, affecting the evolution of the resilience index in the Pareto frontier between ∼0.2 and ∼0.5. In contrast, Group B corresponds to the solution $\mathbf{X_{OLEV}}$ where none of ISWs are allocated in the test system. Here, it is worth reminding that a resilience index close to zero represents a high performing network against severe events or any interruption requirement, i.e., load shedding. In this perspective, as expected the resilience indices value in Group B are significantly higher in comparison to Group A. Detailed results are presented in Table 16 showcasing the planning solution $\mathbf{X_{OLEV}}$ and multi-objective functions corresponding to: 1) the max/min value for each objective function for Group A, and 2) the two solutions for Group B.

First analyzing Group A, one can observe that cases A2, A3 and A5 show greater resilience in comparison to A1, A4 and A6. These results are due to the higher size of DDGs allocated, providing the microgrid with better management capacity for generation/load balancing and, consequently, avoiding additional curtailment. Nonetheless, increasing the size of DDGs consequently increases the TC^{OLEV} and $AEMIS^{OLEV}$ due to the additional cost associated. As can see in Table 16, TC^{OLEV} and $AEMIS^{OLEV}$ for cases A2, A3 and A4 are greater than those in cases A1, A4 and A6. In this sense, the consideration of renewable resources as the main sources leading to a cleaner energy system can significantly reduce $AEMIS^{OLEV}$. This perspective is clearly observed comparing cases A2 to A5, where $AEMIS^{OLEV}$ is significantly reduced for A2 in comparison to A1 due to its higher capacity for renewable resources. Still, $RESI^{OLEV}$ presents very similar values for both cases with TC^{OLEV} for A2 higher in comparison to A5 due to installation cost. From another perspective, Group B solutions feature significantly reduced resilience capacity, i.e., significantly higher $RESI^{OLEV}$ in comparison to Group A. However, given their trade-off between the three multi-objective functions, they are still placed on the Pareto frontier, e.g., TC^{OLEV} for the cases in Group B are significantly lower in comparison to A1-A6.

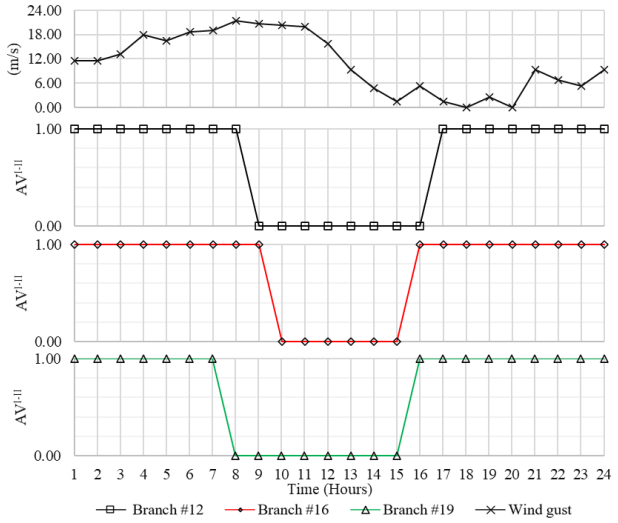

FIGURE 21. Wind gust profile and the timeline of branch #12/#16/#19 availability corresponding to a selected scenario in spring.

D. RESILIENCE IMPROVEMENT

Next, in this section, the obtained optimal planning solutions are stressed for an N-3 contingency scenario to illustrate the system performance in face of severe operating conditions. The N-3 contingency was selected corresponding to the spring season in which multiple faults are localized in the network, respectively on branches #12, #16 and #19. Following, the network performance represented by the energy supply level during the N-3 contingency is determined for the base case, case A1, case A2 and case B2. The corresponding wind gust profile and the binary state representing the availability of branches #12, #16 and #19, according to the selected $\mathbf{AV^{I-II}}$,are presented in Fig. 21.

Whereas Table 17 depicts the availability timeline for branches #12, #16 and #19 along the planning horizon. Based on this scenario, energy supply results are illustrated in Fig. 22 for the base case and optimal planning solutions identified in case A1, case A2 and case B2. Analyzing Fig. 22, one can observe that the base case and case B2 are not able to

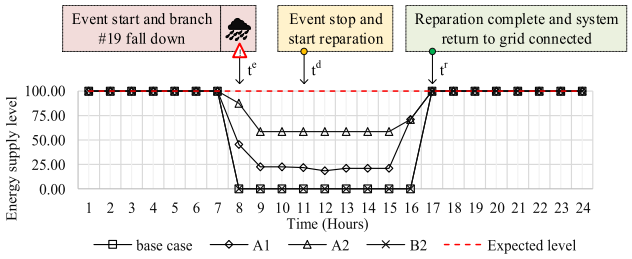

FIGURE 22. Energy supply level and timeline event for representing system performance for base case, case A1, case A2 and case B2.

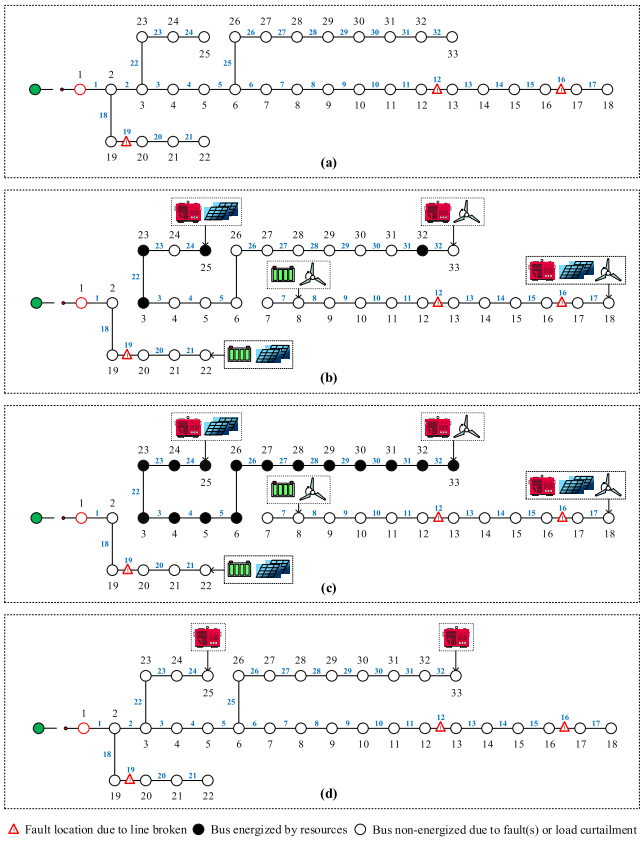

FIGURE 23. Microgrid formations and bus's supply state at t^d for (a) Base case (b) Case A1 (c) Case A2 (d) Case B2.

resist this severe event, leading to a direct drop-in supply from 100% to 0% at t^e. As there are no ISWs placed in the network, the microgrids could not be formed, while only ISW^{sub} found in the substation is open and takes down a whole test system for clearing the faults in this N-3 contingencies. On the other hand, cases A1 and A2 allow for the formation of microgrids, maintaining the energy supply level according to the size of DDGs allocated. In this sense, due to the limited size of DDGs allocated in case A1, the energy supply level drops down to ∼20% at t^d. In contrast, case A2 shows the best performance where the energy supply level drops down from 100% to 59% at t^d, where 41% of non-supplied loads correspond to buses located inside locations isolated by ISWs.

TABLE 17. Timeline of overhead line (branch) #12, #16 and #19 break down over the planning horizon of a selected scenario in spring.

line no.	t^e	$t^{br,fail0}$	t^d	$TTR^{br,fail}$	$t^{br,rep}$	$t^{r'}$	t^r
	8:00	-	11:00	-	-	16:00	17:00
#12		9:00		6h	17:00		
#16	-	10:00	-	5h	16:00	-	-
#19		8:00		5h	16:00		

VIII. CONCLUSION

In this work, a novel resilience-oriented microgrid planning framework is proposed. The proposed framework develops a multi-objective optimization problem formulation incorporating stochastic DL-LOPF^{AC} models solved by NSGA-II based on DNN. The proposed DL-LOPF^{AC} framework provides planning solutions considering stochastic scenarios featuring renewable energy and load uncertainties, HILP events due to N-K contingencies caused by failures in overhead lines, while simultaneously solving for both GC and IS operation modes, including detailed modeling of control and operational requirements, such as droop/2nd during islanded. Next, in order to enable this comprehensive planning framework, NSGA-II based on DNN models is employed to overcome the computation burden and time execution limitations imposed by the stochastic nature of the resilience-oriented planning problem and consideration of the detailed systems' model. In this sense, by taking advantage of the proposed framework predicted solutions obtained by DL-LOPF^{AC} for the inner level present a computation efficient solutions that do not require numerous iterations as found in existing traditional analytical solution methodologies. Following, to verify the effectiveness of the proposed framework multiple numerical analyses are performed. First, the performance for the DL-LOPF^{AC} is evaluated by obtaining significantly reduced MSE/RMSE in relation to the expected error threshold. Moreover, the maximum relative error e_1^{dnn} is found significantly smaller than the threshold for the trained DNN models, demonstrating high accuracy for the DNN models' predicted results. Next, the proposed optimization level NSGA-II based DNN model is validated, demonstrating accuracy levels within accepted deviations, specifically the worst relative error e_1^{OLEV} found is less than 2% for all fitness functions. Finally, the overall planning solution is discussed, indicating the proposed approach ability to deliver optimal planning solutions capable of significantly improving the system resilience even when subjected to HILP events such as N-3 contingencies. Future directions of this work include the integration of electric vehicles into the optimization problems, as these new system elements can significantly impact the system operation, while introducing opportunities in the area of resilience-oriented planning.

ACKNOWLEDGMENT

The author Youthanalack Vilaisarn especially thanks the PCBF for their support of his Doctoral Program studies.

REFERENCES

[1] A. Hirsch, Y. Parag, and J. Guerrero, "Microgrids: A review of technologies, key drivers, and outstanding issues," *Renew. Sustain. Energy Rev.*, vol. 90, pp. 402–411, Jul. 2018, doi: 10.1016/j.rser.2018.03.040.

[2] F. H. Jufri, V. Widiputra, and J. Jung, "State-of-the-art review on power grid resilience to extreme weather events: Definitions, frameworks, quantitative assessment methodologies, and enhancement strategies," *Appl. Energy*, vol. 239, pp. 1049–1065, Apr. 2019, doi: 10.1016/j.apenergy.2019.02.017.

[3] Z. Li, M. Shahidehpour, F. Aminifar, A. Alabdulwahab, and Y. Al-Turki, "Networked microgrids for enhancing the power system resilience," *Proc. IEEE*, vol. 105, no. 7, pp. 1289–1310, Jul. 2017, doi: 10.1109/JPROC.2017.2685558.

[4] Y. Wang, A. O. Rousis, and G. Strbac, "On microgrids and resilience: A comprehensive review on modeling and operational strategies," *Renew. Sustain. Energy Rev.*, vol. 134, Dec. 2020, Art. no. 110313, doi: 10.1016/j.rser.2020.110313.

[5] J. Kim and Y. Dvorkin, "Enhancing distribution system resilience with mobile energy storage and microgrids," *IEEE Trans. Smart Grid*, vol. 10, no. 5, pp. 4996–5006, Sep. 2019, doi: 10.1109/TSG.2018.2872521.

[6] Y. Wang, A. O. Rousis, and G. Strbac, "A three-level planning model for optimal sizing of networked microgrids considering a trade-off between resilience and cost," *IEEE Trans. Power Syst.*, vol. 36, no. 6, pp. 5657–5669, Nov. 2021, doi: 10.1109/TPWRS.2021.3076128.

[7] J. Najafi, A. Peiravi, A. Anvari-Moghaddam, and J. M. Guerrero, "Resilience improvement planning of power-water distribution systems with multiple microgrids against hurricanes using clean strategies," *J. Clean. Prod.*, vol. 223, pp. 109–126, Jun. 2019, doi: 10.1016/j.jclepro.2019.03.141.

[8] M. H. Amirioun, F. Aminifar, and H. Lesani, "Towards proactive scheduling of microgrids against extreme floods," *IEEE Trans. Smart Grid*, vol. 9, no. 4, pp. 3900–3902, Jul. 2018, doi: 10.1109/TSG.2017.2762906.

[9] Q. Shi, F. Li, M. Olama, J. Dong, Y. Xue, M. Starke, C. Winstead, and T. Kuruganti, "Network reconfiguration and distributed energy resource scheduling for improved distribution system resilience," *Int. J. Electr. Power Energy Syst.*, vol. 124, Jan. 2021, Art. no. 106355, doi: 10.1016/j.ijepes.2020.106355.

[10] J. Zhu, Y. Yuan, and W. Wang, "An exact microgrid formation model for load restoration in resilient distribution system," *Int. J. Electr. Power Energy Syst.*, vol. 116, Mar. 2020, Art. no. 105568, doi: 10.1016/j.ijepes.2019.105568.

[11] X. Wu, Z. Wang, T. Ding, X. Wang, Z. Li, and F. Li, "Microgrid planning considering the resilience against contingencies," *IET Gener., Transmiss. Distrib.*, vol. 13, no. 16, pp. 3534–3548, Aug. 2019, doi: 10.1049/iet-gtd.2018.6816.

[12] M. Ghasemi, A. Kazemi, A. Mazza, and E. Bompard, "A three-stage stochastic planning model for enhancing the resilience of distribution systems with microgrid formation strategy," *IET Gener., Transmiss. Distrib.*, vol. 15, no. 13, pp. 1908–1921, Feb. 2021, doi: 10.1049/gtd2.12144.

[13] Y. Wang, A. O. Rousis, and G. Strbac, "Resilience-driven optimal sizing and pre-positioning of mobile energy storage systems in decentralized networked microgrids," *Appl. Energy*, vol. 305, Jan. 2022, Art. no. 117921, doi: 10.1016/j.apenergy.2021.117921.

[14] X. Hu, H. Hu, S. Verma, and Z.-L. Zhang, "Physics-guided deep neural networks for power flow analysis," *IEEE Trans. Power Syst.*, vol. 36, no. 3, pp. 2082–2092, May 2021, doi: 10.1109/TPWRS.2020.3029557.

[15] X. Pan, T. Zhao, M. Chen, and S. Zhang, "DeepOPF: A deep neural network approach for security-constrained DC optimal power flow," *IEEE Trans. Power Syst.*, vol. 36, no. 3, pp. 1725–1735, May 2021, doi: 10.1109/TPWRS.2020.3026379.

[16] J. C. Bedoya, Y. Wang, and C.-C. Liu, "Distribution system resilience under asynchronous information using deep reinforcement learning," *IEEE Trans. Power Syst.*, vol. 36, no. 5, pp. 4235–4245, Sep. 2021.

[17] M. Moradi-Sepahvand, T. Amraee, and S. Sadeghi Gougheri, "Deep learning based hurricane resilient coplanning of transmission lines, battery energy storages, and wind farms," *IEEE Trans. Ind. Informat.*, vol. 18, no. 3, pp. 2120–2131, Mar. 2022, doi: 10.1109/TII.2021.3074397.

[18] M. Dabbaghjamanesh, A. Kavousi-Fard, and J. Zhang, "Stochastic modeling and integration of plug-in hybrid electric vehicles in reconfigurable microgrids with deep learning-based forecasting," *IEEE Trans. Intell. Transp. Syst.*, vol. 22, no. 7, pp. 4394–4403, Jul. 2021, doi: 10.1109/TITS.2020.2973532.

[19] Y. Vilaisarn, M. Moradzadeh, M. Abdelaziz, and J. Cros, "An MILP formulation for the optimum operation of AC microgrids with hierarchical control," *Int. J. Electr. Power Energy Syst.*, vol. 137, May 2022, Art. no. 107674, doi: 10.1016/j.ijepes.2021.107674.

[20] M. Abdelaziz and M. Moradzadeh, "Monte–Carlo simulation based multiobjective optimum allocation of renewable distributed generation using OpenCL," *Electr. Power Syst. Res.*, vol. 170, pp. 81–91, May 2019, doi: 10.1016/j.epsr.2019.01.012.

[21] M. Barani, J. Aghaei, M. A. Akbari, T. Niknam, H. Farahmand, and M. Korpas, "Optimal partitioning of smart distribution systems into supply-sufficient microgrids," *IEEE Trans. Smart Grid*, vol. 10, no. 3, pp. 2523–2533, May 2019, doi: 10.1109/TSG.2018.2803215.

[22] A. J. Conejo, M. Carrion, and J. M. Morales, *Decision Making Under Uncertainty in Electricity Markets*. Piscataway, NJ, USA: IEEE, 2010.

[23] M. Bao, Y. Ding, M. Sang, D. Li, C. Shao, and J. Yan, "Modeling and evaluating nodal resilience of multi-energy systems under windstorms," *Appl. Energy*, vol. 270, Jul. 2020, Art. no. 115136, doi: 10.1016/j.apenergy.2020.115136.

[24] M. H. Amirioun, F. Aminifar, and H. Lesani, "Resilience-oriented proactive management of microgrids against windstorms," *IEEE Trans. Power Syst.*, vol. 33, no. 4, pp. 4275–4284, Jul. 2018, doi: 10.1109/TPWRS.2017.2765600.

[25] M. H. Amirioun, F. Aminifar, H. Lesani, and M. Shahidehpour, "Metrics and quantitative framework for assessing microgrid resilience against windstorms," *Int. J. Electr. Power Energy Syst.*, vol. 104, pp. 716–723, Jan. 2019, doi: 10.1016/j.ijepes.2018.07.025.

[26] J. W. Muhs and M. Parvania, "Stochastic spatio-temporal hurricane impact analysis for power grid resilience studies," in *Proc. IEEE Power Energy Soc. Innov. Smart Grid Technol. Conf. (ISGT)*, Feb. 2019, pp. 1–5, doi: 10.1109/ISGT.2019.8791647.

[27] *Cost-Benefit Analysis of the Deployment of Utility Infrastructure Upgrades and Storm Hardening Programs*, Satell. Commun., Quanta Technol., Raleigh, NC, USA, 2009, pp. 1–108, vol. 3021.

[28] Y. M. Darestani and A. Shafieezadeh, "Multi-dimensional wind fragility functions for wood utility poles," *Eng. Struct.*, vol. 183, pp. 937–948, Mar. 2019, doi: 10.1016/j.engstruct.2019.01.048.

[29] T. A. Short, *Electric Power Distribution Equipment and Systems*. New York, NY, USA: CRC Press, 2006.

[30] S. Poudel, A. Dubey, and A. Bose, "Risk-based probabilistic quantification of power distribution system operational resilience," *IEEE Syst. J.*, vol. 14, no. 3, pp. 3506–3517, Sep. 2020.

[31] F. S. Gazijahani and J. Salehi, "Robust design of microgrids with reconfigurable topology under severe uncertainty," *IEEE Trans. Sustain. Energy*, vol. 9, no. 2, pp. 559–569, Apr. 2018, doi: 10.1109/TSTE.2017.2748882.

[32] M. Moradzadeh and M. M. A. Abdelaziz, "A stochastic optimal planning model for fully green stand-alone PEV charging stations," *IEEE Trans. Transport. Electrific.*, vol. 7, no. 4, pp. 2356–2375, Dec. 2021, doi: 10.1109/TTE.2021.3069438.

[33] M. Moradzadeh and M. M. A. Abdelaziz, "A new MILP formulation for renewables and energy storage integration in fast charging stations," *IEEE Trans. Transport. Electrific.*, vol. 6, no. 1, pp. 181–198, Mar. 2020, doi: 10.1109/TTE.2020.2974179.

[34] B. Mukhopadhyay and D. Das, "Optimal multi-objective expansion planning of a droop-regulated islanded microgrid," *Energy*, vol. 218, Mar. 2021, Art. no. 119415, doi: 10.1016/j.energy.2020.119415.

[35] M. F. Shaaban and E. F. El-Saadany, "Accommodating high penetrations of PEVs and renewable DG considering uncertainties in distribution systems," *IEEE Trans. Power Syst.*, vol. 29, no. 1, pp. 259–270, Jan. 2014, doi: 10.1109/TPWRS.2013.2278847.

[36] A. Maulik and D. Das, "Optimal operation of droop-controlled islanded microgrids," *IEEE Trans. Sustain. Energy*, vol. 9, no. 3, pp. 1337–1348, Jul. 2018, doi: 10.1109/TSTE.2017.2783356.

[37] P. P. Vergara, J. C. Lopez, M. J. Rider, and L. C. P. da Silva, "Optimal operation of unbalanced three-phase islanded droop-based microgrids," *IEEE Trans. Smart Grid*, vol. 10, no. 1, pp. 928–940, Jan. 2019, doi: 10.1109/TSG.2017.2756021.

[38] P. P. Vergara, J. C. López, L. C. P. da Silva, and M. J. Rider, "Security-constrained optimal energy management system for three-phase residential microgrids," *Electr. Power Syst. Res.*, vol. 146, pp. 371–382, May 2017, doi: 10.1016/j.epsr.2017.02.012.

[39] P. P. Vergara, J. M. Rey, J. C. López, M. J. Rider, L. C. P. D. Silva, H. R. Shaker, and B. N. Jørgensen, "A generalized model for the optimal operation of microgrids in grid-connected and islanded droop-based mode," *IEEE Trans. Smart Grid*, vol. 10, no. 5, pp. 5032–5045, Sep. 2019, doi: 10.1109/TSG.2018.2873411.

[40] I. Alsaidan, A. Khodaei, and W. Gao, "A comprehensive battery energy storage optimal sizing model for microgrid applications," *IEEE Trans. Power Syst.*, vol. 33, no. 4, pp. 3968–3980, Jul. 2018, doi: 10.1109/TPWRS.2017.2769639.
[41] J. David, M. Van Nguyen, and N. Cohen, *Algorithmic Graph Theory*. Free Software Foundation, 2012. [Online]. Available: http://code.google.com/p/graphbook/
[42] R. Balakrishnan and K. Ranganathan, *A Textbook of Graph Theory*. New York, NY, USA: Springer, 2012.
[43] H. E. Farag, M. M. A. Abdelaziz, and E. F. El-Saadany, "Voltage and reactive power impacts on successful operation of islanded microgrids," *IEEE Trans. Power Syst.*, vol. 28, no. 2, pp. 1716–1727, May 2013, doi: 10.1109/TPWRS.2012.2223491.
[44] M. M. A. Abdelaziz, H. E. Farag, and E. F. El-Saadany, "Optimum droop parameter settings of islanded microgrids with renewable energy resources," *IEEE Trans. Sustain. Energy*, vol. 5, no. 2, pp. 434–445, Apr. 2014, doi: 10.1109/TSTE.2013.2293201.
[45] R. Tarjan, "Depth-first search and linear graph algorithms," *SIAM J. Comput.*, vol. 1, no. 2, pp. 146–160, Jun. 1972, doi: 10.1137/0201010.
[46] T. H. Cormen, C. E. Leiserson, R. L. Rivest, and C. Stein, *Introduction to Algorithms*, 3rd ed. Cambridge, MA, USA: MIT Press, 2009.
[47] J. D. Glover, M. S. Sarma, and T. J. Overbye, *Power System Analysis and Design*. Stamford, CT, USA: Cengage Learning, 2012.
[48] H. B. Demuth and M. T. Hagan, *Neural Network Design*, 2nd ed. Boston, MA, USA: Martin Hagan, 2014.
[49] S. Haykin, *Neural Networks and Learning*, vols. 1–3. Amsterdam, The Netherlands: Elsevier, 2008.
[50] M. H. Beale, M. T. Hagan, and H. B. Demuth, *Deep Learning Toolbox™ User's Guide*. Natick, MA, USA: MathWorks, 2021.
[51] K. Deb, A. Pratap, S. Agarwal, and T. Meyarivan, "A fast and elitist multiobjective genetic algorithm: NSGA-II," *IEEE Trans. Evol. Comput.*, vol. 6, no. 2, pp. 182–197, Aug. 2002, doi: 10.1109/4235.996017.
[52] *The National Renewable Energy Laboratory (NREL)*. Accessed: Jan. 5, 2021. [Online]. Available: https://maps.nrel.gov/nsrdb-viewer
[53] *New York Independent System Operator*. Accessed: Jan. 5, 2021. [Online]. Available: http://www.nyiso.com
[54] Y. Vilaisarn and M. Abdelaziz, "An inversion-free sparse Z power flow algorithm for large-scale droop controlled islanded microgrids," *Int. J. Electr. Power Energy Syst.*, vol. 121, Oct. 2020, Art. no. 106048, doi: 10.1016/j.ijepes.2020.106048.
[55] H. Haddadian and R. Noroozian, "Multi-microgrids approach for design and operation of future distribution networks based on novel technical indices," *Appl. Energy*, vol. 185, pp. 650–663, Jan. 2017, doi: 10.1016/j.apenergy.2016.10.120.
[56] L. Wang, A. H. C. Ng, and K. Deb, *Multi-objective Evolutionary Optimisation for Product Design and Manufacturing*. London, U.K.: Springer, 2011.

YOUTHANALACK VILAISARN received the B.S. degree in electrical engineering from the National University of Laos, Vientiane, Laos, in 2013, and the M.S. degree in electrical engineering from Paul Sabatier University (TOULOUSE III), Toulouse, France, in 2015. He is currently pursuing the Ph.D. degree with Laval University, Quebec, QC, Canada. His research interests include microgrid operation and control, power flow analysis for microgrids, microgrid optimal operation, and planning of microgrids.

YURI R. RODRIGUES received the B.Sc. and M.Sc. degrees in electrical engineering from the Federal University of Itajuba, Brazil, in 2015 and 2017, respectively, and the Ph.D. degree in electrical engineering from the University of British Columbia, Canada, in 2021. He is currently an Assistant Professor with Seattle Pacific University, USA. His research interests include dynamics, controls and analysis of microgrids and active distribution networks, advanced monitoring provided by phasor measurement units, integration of distributed and renewable generation, power system short- and long-term stability, and engineering education.

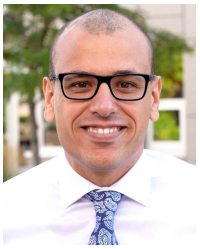

MORAD MOHAMED ABDELMAGEED ABDELAZIZ (Senior Member, IEEE) was born in Cairo, Egypt, in September, 1984. He received the B.Sc. (Hons.) and M.Sc. degrees in electrical engineering from Ain Shams University, Cairo, Egypt, in 2006 and 2009, respectively, and the Ph.D. degree in electrical and computer engineering from the University of Waterloo, ON, Canada, in 2014.

He is currently an Assistant Professor with the School of Engineering, University of British Columbia, Kelowna, Canada. He is a Registered Professional Engineer in the province of British Columbia. His research interests include the applications of machine learning (ML), optimization and high-performance computation (HPC) in smart grids, electric vehicles charging infrastructure, integration of distributed and renewable generation, electrification of the transportation systems, power systems operation and decarbonization and dynamics, controls and analysis of microgrids, and active distribution networks.

Dr. Abdelaziz is an Associate Editor for *IET Generation, Transmission & Distribution* and the *Canadian Journal of Electrical and Computer Engineering* (CJECE). He has been recognized as one of the best reviewers for the IEEE TRANSACTIONS ON SMART GRID.

JÉRÔME CROS received the Doctoral degree from the Institut National Polytechnique of Toulouse, France, in 1992, where he worked on design of brushless dc motors for automotive applications. Since 1995, he has been a Professor with the Electrical Engineering Department, Laval University, Québec, QC, Canada. His research interests include electrical machine design, modeling methods, magnetic field calculation, drives, condition monitoring, and fault diagnosis.